Ferromagnetically Contacted Carbon Nanotube Quantum Dots

Mark Dennis Elkin

Department of Physics and Astronomy

University of Leeds

Submitted in accordance with the requirements for the degree of

Doctor of Philosophy

March 2012

The candidate confirms that the work submitted is his own and that appropriate credit has been given within the thesis where reference has been made to the work of others.

Acknowledgements

I would like to thank my supervisor Prof. B. J. Hickey whose support, endless enthusiasm and knowledge has been a source of enlightenment during my time in the group. I would also like to thank Dr Oscar Cespedes for the helpful discussions on the path of my research and Dr Gavin Burnell for his contributions to my understanding of the intricacies of measurement systems and without whom my work would have been far more manual in nature. I also am greatly indebted to all the people in leeds who have trained me. To Dr Mannan Ali, Dr Aidan Hindmarch and Dr Chris Allen who contributed their time and skills to my cause.

I would also like to thank Mr John Turton and Mr Phil Cale who managed to keep my experiments running sweet and cold, despite my monopoly of a piece of equipment that caused me to be awarded the condensed matter prize for the group member with the most cryogens consumed year on year.

My great thanks also go to my collaborators at Basel University. Prof. Schönenburger and Dr Andreas Baumgartner who kindly supplied Carbon nanotubes to cary out my work with and discussions on my results.

To Jason Morgan has been an excellent housemate and friend and all the members of the condensed matter group who have made my PhD enjoyable, whether climbing, playing basketball or drinking tea.

For Dina, without whose support I may have become lost.

Abstract

This thesis presents research into spin-transport in Carbon nanotube quantum dots. Sputtered Permalloy electrodes designed with shape anisotropy were used to contact Carbon nanotubes grown by chemical-vapour deposition in lateral spin-valve structures. The magnetoresistance of these spin-valves were measured at low-temperatures and as a function of the charge state of the quantum dots.

Two conductance regimes were measured in a Carbon nanotube spin-valve with Permalloy nucleation pads. At high bias outside of the coulomb blockade regime a $\sim 10\%$ magnetoresistance was measured that is analogous to giant-magnetoresistance, in that it is due to spin-dependent scattering at the ferromagnet-Carbon nanotube interfaces. At lower bias the device enters the coulomb blockade regime and the magnetoresistance observed develops a different structure, over a larger field range, together with the development of an offset in conductance between saturations. The maximum value of this MR was $MR \sim 245\%$ and it was attributed to changes in the induced charge on the quantum dot.

By modifying the design of the Permalloy electrodes, a single domain state at the point of contact of the Carbon nanotube was achieved. A well defined anti-parallel state of the Permalloy electrodes, with associated changes in the conduction of the devices was observed, yet the conductance offset remained, with a maximum MR of $\sim 60\%$.

The positions of the coulomb peaks were measured during magnetic reversal of the electrodes, showing the change in induced charge on the quantum dot, with a maximum $MR \sim 350\%$. Predictions of device transport based on the magneto-coulomb effect and spin-dependent

interfacial phase shifts were compared to experimental results and found to not fit the observed behaviour. This led to the conclusion that changes in the charge state of the quantum dots must be due to a fixed spin-quantisation axis intrinsic to the Carbon nanotube.

Abbreviations

AC	Alternating Current
AMR	Anisotropic Magnetoresistance
CNT	Carbon Nanotube
CVD	Chemical Vapour Deposition
DC	Direct Current
DOS	Density Of States
EBL	Electron Beam Lithography
FM	Ferromagnet
FWHM	Full-Width Half-Maximum
GMR	Giant Magnetoresistance
MC	Magneto-Coulomb
MOKE	Magneto-Optical Kerr Effect
MR	Magnetoresistance
MWCNT	Multi-Walled Carbon Nanotube
NM	Normal Metal
OOMMF	Object Orientated MicroMagnetic Framework
QD	Quantum Dot
QW	Quantum Wire
SDIPS	Spin-Dependent Interfacial Phase Shifts
SEM	Scanning Electron Microscope
SWCNT	Single-Walled Carbon Nanotube
TB	Tunnel Barrier
TMR	Tunnel Magnetoresistance

Publications

C. S. Allen, **M. D. Elkin,** G. Burnell, B. J. Hickey, C. Zhang, S. Hofmann and J. Robertson, "Transport measurements on carbon nanotubes structurally characterized by electron diffraction," *Physical Review B,* vol. 84, no. 11, 115444, 2011

Priyanka A. Pandey, Gavin R. Bell, Jonathan P. Rourke, Ana M. Sanchez, **Mark D. Elkin,** Bryan J. Hickey, and Neil R. Wilson, "Physical Vapor Deposition of Metal Nanoparticles on Chemically Modified Graphene: Observations on MetalGraphene Interactions," *Small,* vol. 7, no. 22, 3202-3210, 2011

Contents

Chapter 1

Introduction

Since their discovery in 1991 by Iijima[1] carbon nanotubes (CNTs) have been an area of intense research interest, both experimental and theoretical, over a broad range of disciplines due to their novel properties. For example, much work has been carried out on incorporating them into composites[2, 3] and using them to spin fibres[4, 5] as they have the largest tensile strength and Young's modulus of any material discovered[6, 7]. Their high thermal conductivity has also been of interest with multi-walled carbon nanotubes (MWCNTs) showing thermal conductivities of over 3000 $\mathrm{WK^{-1}m^{-1}}$[8], many times that of copper, at $\sim$400 $\mathrm{WK^{-1}m^{-1}}$. Good room temperature conductivity and a strong sensitivity to electric field of semiconducting CNTs has seen them investigated as field-effect transistors[9, 10, 11, 12] (FETs) for use in logic systems[13], however some of the most interesting physics in CNTs is found in the low-temperature transport regime in which they act as one-dimensional quantum wires, with ballistic conductance[14, 15]. Depending on the contact properties to the CNTs at low-temperature they may exhibit Fabrey-Perot resonances with transparent contacts (Transmission probability $T \sim 1$),[16, 17, 18] where the conductance through the tube has been shown to be close to the maximum for two-channel spin-degenerate quantum wire. While with low transmission contacts ($T \ll 1$) CNTs may form quantum dots (QDs)[19, 20, 21], where transport is only allowed through tunnelling via the discrete energy levels available in the CNT, with Kondo resonances having been observed in the intermediate contact regime ($T \sim 0.6$)[22, 23, 24], in which electron spins in the nanotube QD couple to spins in the metallic electrodes, forming a correlated many-electron state, allowing current to flow at zero bias even when an energy level of the QD is not available for transport.

The quality of contact between CNTs and metals is dependent of the properties of the metal used. With early experiments showing the formation of Schottky barriers at the CNT-metal contact[11, 25]. When using palladium, a metal with a high work-function and good wetting interaction with CNTs[26, 27] as a contact material these barriers are greatly reduced or eliminated[28, 29] and good transport through the valence band of the CNTs is achieved, with conductance values close to the theoretical maximum of $4e^2/h$ for CNTs.

Due to the lack of nuclear spin of the main carbon isotope C^{12} and the predicted long coherence lengths in CNTs make them ideal for use in spintronic devices, in which the spin degree of freedom of electrons is used to control transport. The classic example of which is a spin-valve where the transport between two ferromagnetic (FM) layers via an intermediary material is dependent on the relative magnetisation and hence the spin polarisations of the FM layers. Experiments using CNTs as the intermediary material in spin valve structures have shown evidence of spin transport in CNTs[30] and experiments on FM contacted CNT QDs have shown that the spin transport through CNTs is dependent on the quantised energy levels within the QDs[31]. All current work on FM contacted CNTs has been carried out using evaporated electrodes, however the preferred method of deposition for metal spintronic devices is sputtering. Also the materials chosen for contacting CNTs have generally been selected by considering the quality of contact between CNT and FM, meaning the magnetic properties of the FMs have not been ideal. For example, the nickel-palladium contacts used to demonstrate gate-voltage control of spin-transport show anti-ferromagnetic ordering of their domain structures when patterned into nanostructures[32], meaning their magnetisation is not well defined.

The aim of this work is to study spin-transport in CNTs. The band structure of CNTs means that ballistic, spin-coherent transport should be possible. The low spin-orbit interaction in carbon suggests that the spin diffusion length should be long and electron-electron interactions in low-dimensional systems such as QDs means that the spin-transport could be dependent on the energy quantisation.

Contact was made to CNTs using sputtered permalloy (Py) an 80% nickel 20% iron alloy, currently used extensively in spintronic research due to its advantageous properties[33, 34], which include a high spin-polarisation[35], a low coercivity, almost zero magnetostriction[36], a strong shape anisotropy and a large domain size[37]. This was done by investigating the dependence of the magnetoresistance (MR) of sputtered Py contacted CNT QDs at low temperature to the discrete energy level spectra of the QD.

In Chapter 2 an overview of theory relevant to the transport through FM contacted CNT QDs will be presented. Beginning with the structure and electronic properties of graphene and how they relate to those of CNTs of differing sizes and structural characteristics. The basic principles of electron transport through quantum dots and how they can be realised experimentally, including the transport of CNT QDs and estimates of their energy scales. Then the origin of ferromagnetism will be introduced, together with spin-dependent transport originating with the two-band model and explaining magnetoresistance. Followed by the interaction between CNT QDs and both applied magnetic fields and electrode magnetisation, considering movement of energy levels within a QD due to magnetic fields parallel and perpendicular to the CNT axis and energy and field effects caused by the introduction of ferromagnetic electrodes, including the magneto-coulomb (MC) effect and spin-dependent interfacial phase-shifts (SDIPS). This is followed by a review of pertinent experimental results.

Chapter 3 will describe the experimental techniques used to make CNT devices, together with methods used to acquire results presented in this work.

Chapter 4 will present results obtained from a Py contacted CNT QD that incorporates shape anisotropy in the Py pads to perform spin-valve measurements. The source-drain bias dependence of the observed MR will be presented, together with interpretations of the dependence based on the high bias resistive transport regime and the low bias coulomb blockade regime. In the low bias regime large changes in conductance are attributed to shifts in the charge state of the QD, with the magnitude of these shifts being greater than that predicted by the MC effect.

Chapter 5 will show results obtained from Py contacted CNT QDs that use electrodes with better defined magnetic behaviour than the designs used previously.

Observed changes in device conductance as attributed previously to changes in the energy level spectra of the QD are now directly observed and compared to theoretical predictions for ferromagnetically contacted CNTs.
Finally conclusions that can be drawn from this work and plans for future investigations are given in Chapter 6.

Chapter 2

Theory

2.1 Carbon Nanotubes

Carbon nanotubes (CNTs) are large molecules made up of carbon atoms bonded in a hexagonal honeycomb structure like that of graphene, which itself is a single atomic layer of Graphite[38], shown in Figure 2.1.

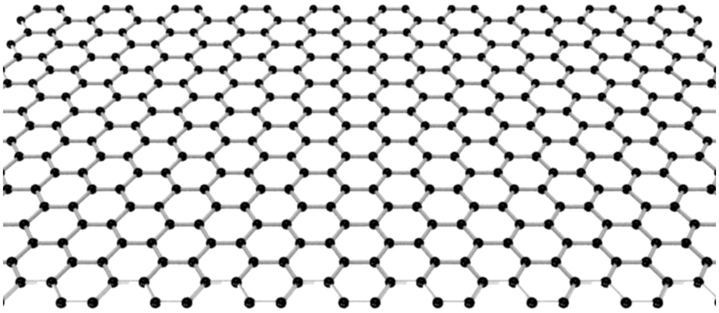

Figure 2.1: Atomic structure of a sheet of graphene.

A particular single-walled nanotube can be thought of as a sheet of graphene that has been rolled up along a particular chiral vector $\mathbf{C}$, where $\mathbf{C}$ is made up of the graphene lattice vectors $\boldsymbol{a}_1$ and $\boldsymbol{a}_2$ and becomes the circumference of the tube[39, 40]. Normally a chiral vector is quoted by its chiral indices in the form (n_1, n_2) where[41]:

$$\mathbf{C} = n_1\boldsymbol{a}_1 + n_2\boldsymbol{a}_2$$

These chiral indices correspond to a chiral angle θ and diameter d:

$$\theta = \cos^{-1}\left(\frac{n_1 + n_2/2}{\sqrt{n_1^2 + n_1 n_2 + n_2^2}}\right)$$

$$d = \frac{a_0}{\pi}\sqrt{n_1^2 + n_1 n_2 + n_2^2}$$

where $a_0 = 2.461$ Å is the lattice constant of graphene. The smallest graphene lattice vector perpendicular to **C** is known as the translational vector (**T**) and together with the chiral vector defines the unit cell of a carbon nanotube. Figure 2.2 illustrates this and shows the chiral and translational vectors for a (4,2) carbon nanotube.

Due to the similarities between the structure of carbon nanotubes and graphene the electronic properties of tubes can be obtained from the properties of graphene, which will now be discussed. A carbon atom has 6 electrons, 4 of which are in its valence shell in $2s^2$ and $2p^2$ orbitals. In graphene and other carbon allotropes with

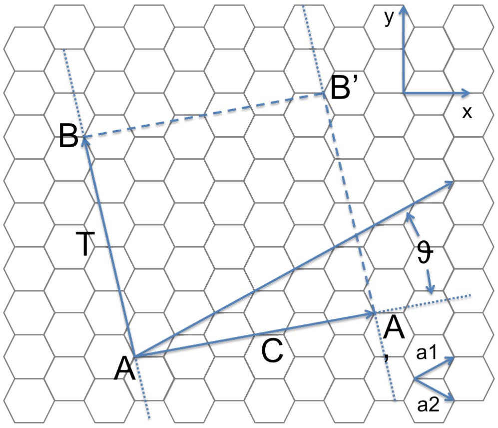

Figure 2.2: The hexagonal atomic structure of graphene with basis vectors $\boldsymbol{a}_1$ and $\boldsymbol{a}_2$, showing the construction of a carbon nanotube with chiral vector **C**. The nanotube is constructed by the rolling up of the graphene sheet along the chiral vector until the point A meets the point A' and the point B meets the point B'. The translational vector **T** points along the tube axis and the angle θ is the chiral angle between **C** and $\boldsymbol{a}_1$. Adapted from Saito et al.[42]

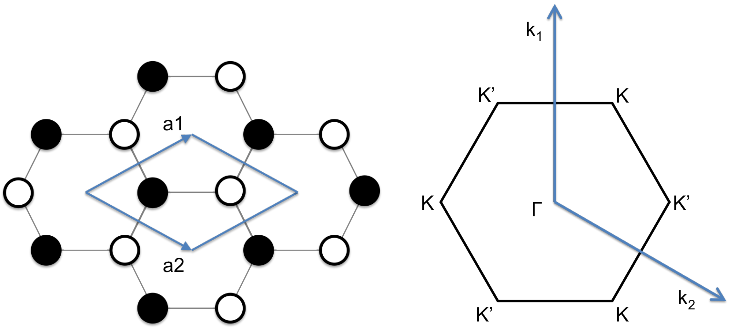

(a) (b)

Figure 2.3: (a) The unit cell of graphene containing two carbon atoms with basis vectors $\boldsymbol{a}_1$ and $\boldsymbol{a}_2$ with corresponding reciprocal lattice (b) showing the first Brillouin zone and high symmetry points Γ and K. The reciprocal lattice vectors $\boldsymbol{k}_1$ and $\boldsymbol{k}_2$ in Cartesian coordinates are $\boldsymbol{k}_1 = (0, 1)4\pi/\sqrt{3}a_0$ and $\boldsymbol{k}_2 = (0.5\sqrt{3}, -0.5)4\pi/\sqrt{3}a_0$.[39]

honeycomb lattices two p-orbital electrons and one s-orbital electron combine to produce three sp^2 hybrid orbitals, which lie in-plane at 120° to one another, forming σ bonds. The final valence electron is then in a $\mathrm{p_Z}$ orbital perpendicular to the plane of the σ bonds and forms bonding and anti-bonding π and π^* bonds.

The Brillouin zone of graphene in Figure 2.3(b) has two non-equivalent points K and K' corresponding to the two atoms in the graphene unit cell shown in Figure 2.3(a), the rest of the six points can be obtained from transformations along the reciprocal lattice vectors $\boldsymbol{k}_1$ and $\boldsymbol{k}_2$. As the σ bonds in graphene are far from the Fermi level with a band gap of $\sim$ 11 eV the electronic properties of graphene are well described by taking into account the energy dispersion of only the π bonding electrons. The dispersion relation of the π orbitals can be approximated with a first or third nearest neighbour tight binding calculation. The nearest neighbour approach provides a reasonable approximation of the energy dispersion at or near the Fermi level, but does not accurately reproduce the π bands over a large range of the Brillouin zone, whereas the third nearest neighbour approximation can quite accurately reproduce energy dispersions from ab-initio calculations.[43]. The dispersion relation for a nearest neighbour tight-binding calculation is shown in Figure 2.4, where the energy of the dispersion was calculated from:

$$E^{\pm}(\boldsymbol{k}_x, \boldsymbol{k}_y) = \frac{\epsilon_{2p} \pm \gamma_0 \sqrt{f_{xy}(\boldsymbol{k}_x, \boldsymbol{k}_y)}}{1 \pm s_0 \sqrt{f_{xy}(\boldsymbol{k}_x, \boldsymbol{k}_y)}}$$

where ϵ_{2p} is the energy of the $2p_z$ orbital, s_0 the overlap integral between the two nearest neighbours and γ_0 the carbon-Carbon interaction energy or tight binding integral. The function $f(\boldsymbol{k}_x, \boldsymbol{k}_y)$ is derived from the energies of the $2p_z$ electrons and their overlap elements in reciprocal space is:

$$f_{\boldsymbol{xy}} = 3 + 2\cos a_0 \boldsymbol{y} + 4\cos \frac{\sqrt{3}a_0}{2}\boldsymbol{x} \cos \frac{a_0}{2}\boldsymbol{y}$$

The graphene π bands are seen to meet at the Fermi level at six points corresponding to the K points of the Brillouin zone, with a linear relationship between E and $\boldsymbol{k}$. This linear relationship $E^{\pm}(\boldsymbol{k}) = \pm v_F \hbar \mid \boldsymbol{k} \mid$ means that the electrons and holes have zero effective mass around the Fermi energy and so behave like

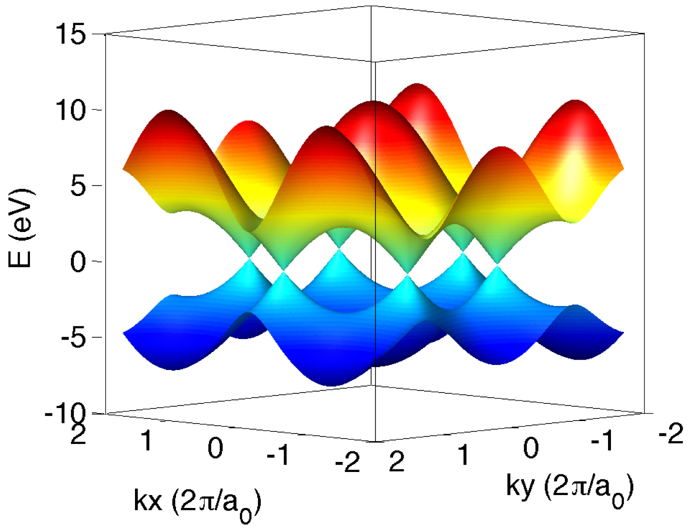

Figure 2.4: The electronic band structure of a graphene sheet obtained from a nearest-neighbour tight-binding calculation. The valence and conduction band are seen to meet at the K points of the reciprocal lattice at which $E^{\pm}(\boldsymbol{k})$ is approximately linear.

relativistic particles with a speed equal to the Fermi velocity, $v_F \sim 10^6$ ms^{-1}[44]. As the two atoms in the graphene unit cell each donate one electron to the bonding and anti-bonding pairs of the valence and conduction band, examining the energy dispersion about a K point as shown in Figure 2.5 we see the electrons and holes at a displacement of $\pm\boldsymbol{k}$ from the K point have opposite molecular orbital states, these two states are often described as a pseudospin as they behave in an analogous way to an electron spin. Due to this pseudospin, backscattering is not allowed between $\boldsymbol{k}$ and -$\boldsymbol{k}$ directions because of their orthogonal molecular orbitals and although inter-band scattering is still allowed, this preserves the direction of motion and does not introduce electrical resistance[45]. Due to this effect the electrons have long mean free paths, meaning graphene and graphene-like materials have potential for spintronic applications[46] due to long spin coherence lengths[47].

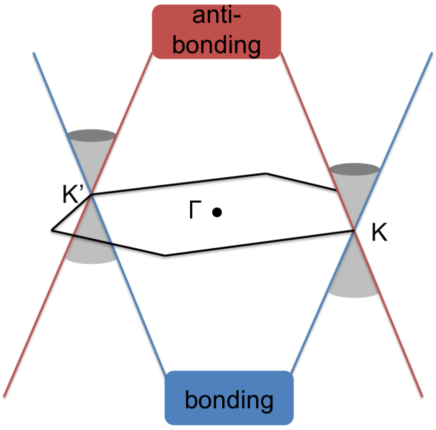

Figure 2.5: Energy dispersion of a graphene sheet around the Fermi energy showing the contribution of the two orbital states at either side of a K point. Adapted from Ensslin[48]

The electronic properties of a carbon nanotube with particular chiral indices can be found by first finding the unit cell of the carbon nanotube in question. The unit cell of the carbon nanotube is formed by a cylindrical surface with diameter d and a height equal to the translational unit vector $\boldsymbol{a}$, where the tubes diameter is given by:

$$d = \frac{|c|}{\pi}$$

where $\boldsymbol{a}$ is defined as the smallest graphene lattice vector perpendicular to c, along the translational vector $\mathbf{T}$. The reciprocal lattice vector $\boldsymbol{k}_z$ is then defined as:

$$\boldsymbol{k}_z = \frac{2\pi}{\boldsymbol{a}}$$

If it is assumed the tube is infinitely long in relation to its diameter this wave vector is continuous. The second reciprocal lattice vector $\boldsymbol{k}_\perp$, which points along the circumference of the tube must be quantised due to the continuous nature of the circumference according to the boundary conditions:

$$m \cdot \lambda = |c| = \pi \cdot \mathrm{d}$$

$$\boldsymbol{k}_{\perp,m} = \frac{2\pi}{\lambda} = \frac{2\pi}{|c|} \cdot m = \frac{2}{\mathrm{d}} \cdot m$$

where m is an integer with values that span between $-q/2 + 1$ and $q/2$ where q is the number of graphene hexagons in the carbon nanotube unit cell. This quantisation is very important to physical and transport properties of carbon nanotubes as it limits the modes of electrons and phonons travelling circumferentially around the tube to those that have a phase shift of an integer multiple of 2π as all other modes will vanish due to interference, making the carbon nanotube a quasi-one-dimensional system. The Brillouin zone of a (10,10) nanotube is shown as a series of red lines on top of the reciprocal lattice of graphene in Figure 2.6 with its periodic conditions in the $\boldsymbol{k}_\perp$ axis showing the quantisation of states.

The electronic structure of a carbon nanotube can then be found by mapping the energy dispersion of a graphene sheet onto the Brillouin zone of that particular tube. As the conduction and valence bands of graphene meet at the K points of its Brillouin zone, carbon nanotubes with Brillouin zones that cross a K point of the graphene Brillouin zone are metallic, whereas tubes that have a Brillouin

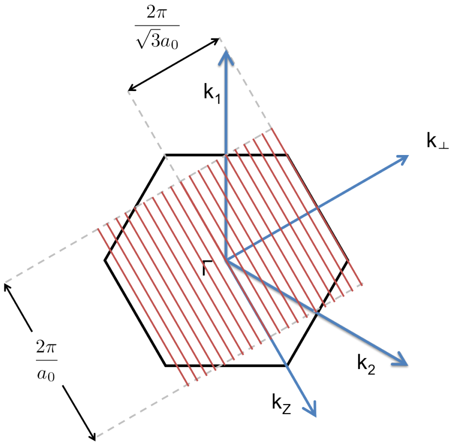

Figure 2.6: Brillouin zone of a (10,10) carbon nanotube shown in red overlaying that of a graphene sheet, showing quantisation in the $\boldsymbol{k}_\perp$ axis. Adapted from Reich et al. [41]

zone that does not cross a K point are semiconducting, with varying band gaps depending on their chiral vector. Using this approach it is expected that roughly 1/3 of carbon nanotubes are metallic or quasi-metallic.

The electronic structure of a (10,10) carbon nanotube for $\Gamma \leq \boldsymbol{k}_z \leq \pi/a_0$ derived from the dispersion relation of graphene is shown in Figure 2.7, showing the linear energy dispersion around a K point, while the electronic structure of a (19,0) semiconducting tube are shown in Figure 2.8, showing a gap between valence and conduction bands and a non-linear dispersion of the energy levels closest to zero energy.

The electronic states either side of a K point in metallic carbon nanotubes, like those of graphene, correspond to the two molecular orbital states. Backscattering occurs between these two states displaced from the K point by $\boldsymbol{k}$ and $\boldsymbol{k}$', as shown in Figure 2.9. The overlap of the two states depends on the angle between them as $\cos^2(\theta/2)$ where θ is the angle between the two states, making this scattering process forbidden. However for semiconducting tubes the Brillouin zone is offset from a K point, making the angle between $\boldsymbol{k}$ and $\boldsymbol{k}$' less than π and allowing backscattering to occur. This makes the mean free path for semiconducting tubes orders of magnitude smaller than that of metallic ones and makes them sensitive to long range disorder[49].

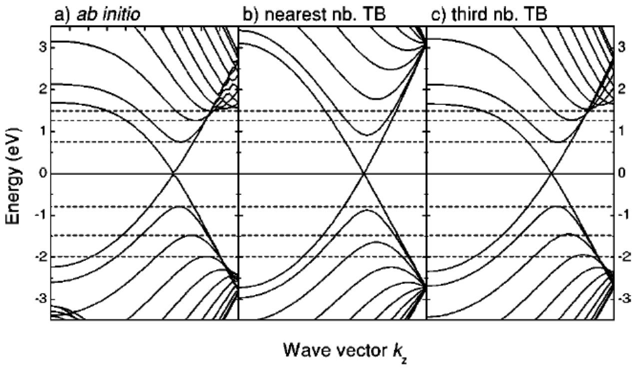

Figure 2.7: Band Structure of a (10,10) nanotube obtained from the electronic structure of graphene obtained by: (a) Ab-initio calculation (b) Nearest-neighber tight-binding and (c) Third-nearest-neighbour tight-binding. Taken from Reich et al.[43]

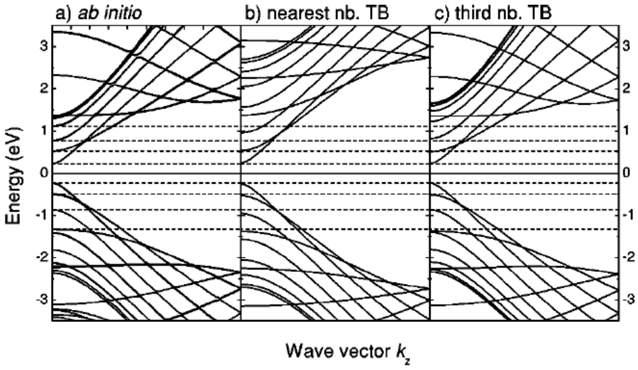

Figure 2.8: Band Structure of a (19,0) nanotube obtained from the electronic structure of graphene obtained by: (a) Ab-initio calculation (b) Nearest-neighber tight-binding and (c) Third-nearest-neighbour tight-binding. Taken from Reich et al.[43]

The mean free paths in metallic carbon nanotubes can be of the order of 1 μm[19, 50, 51, 52] and as devices often have channel lengths of less than this, their transport may be described as ballistic. In the ballistic regime there is no resistance associated with conduction through the tube due to the lack of scattering but the conductance remains finite as the maximum conductance is given

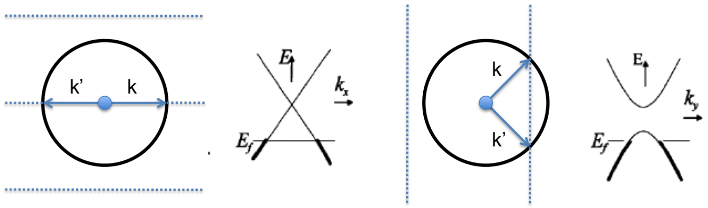

Figure 2.9: Allowed k values for a metallic and semiconducting nanotube relative to the Fermi circle of graphene about a K point at an energy E_F. Adapted from McEuen et al.[49]

by $n\frac{e^2}{h}$, where n is the number of one-dimensional (1D) channels available for transport through the device and $\frac{e^2}{h}$ is the quantum of conductance. Near the Fermi energy carbon nanotubes have 2 spin-degenerate 1D channels so we expect a maximum conductance of $\frac{4e^2}{h}$ or 2 G_0, where G_0 is defined as the conduction through one spin degenerate 1D channel. This maximum conductance is only achieved when the tube is perfectly contacted i.e. there is 100% transmission and no reflection at the tube boundaries. For non-perfect contacts this is reduced and the conduction through each channel is dependent on the transmission into and out of the tube T_i giving $G = \frac{2e^2}{h}\Sigma_i T_i$, where the summation is over all the available channels.

2.2 Quantum Dots

Quantum dots (QDs) are zero dimensional objects in that their physical size is less than their Fermi wavelength giving them a discrete energy spectrum of electron states analogous to that of an atom[53, 54]. Electron transport through a dot may be performed by contacting the quantum dot with a source (S) and drain (D) electrode which couple to the dot by tunnelling into the discrete states, with the coupling characterised by the capacitance of the contact $C_{\mathrm{S(D)}}$ and the coupling strength $\Gamma_{\mathrm{S(D)}}$. A third electrode that is only capacitively coupled to the dot via C_{g} may also be used to tune the energy of the states of the dot as shown in Figure 2.10. Carbon nanotubes may form QDs in this way when the tunnel barriers form between themselves and metal electrodes deposited on them. In this case the transmission probability between metal and tube is < 1 and the conductance through the tube is less than the theoretical maximum of 2 G_0.

The weak coupling between the QD and the electrodes means the number of electrons on the QD is an integer N. For transport to occur through a QD an electron must tunnel from the source electrode into the dot raising the number of electrons on the dot by one, then tunnel from the dot to the drain electrode, however to add an additional electron to the island the coulomb repulsion between the added electron and the charge on the island must be overcome. This is known as the charging energy of the QD, $U_\mathrm{C} = e^2/C_\Sigma$, where C_Σ=C_S+C_D+C_g[55]. The gate electrode may tune the electrostatic energy of the QD by inducing an effective charge q=$C_\mathrm{g}V_\mathrm{g}$ on the dot. When sweeping V_g the build up of induced charge will be compensated for by tunnelling of discrete charges onto the dot. The period of oscillation of the discrete charge addition to the dot leads to Coulomb oscillations in the conductance of the device, as when a gate voltage value is reached that corresponds to an electron being added to the dot, the number of electrons is allowed to alternate between N and N+1 and current is able to flow through the dot, whereas the conduction through the dot is blocked for all other values, as

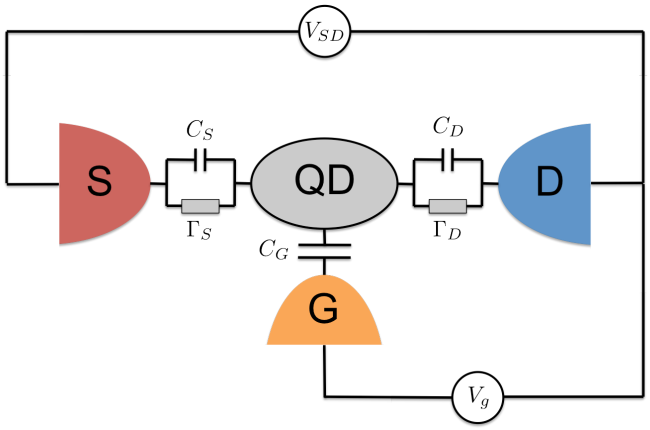

Figure 2.10: Coupling of a Quantum dot (QD) to macroscopic measurement apparatus. Source and Drain lines are characterised by a capacitance ($C_{\mathrm{S(D)}}$) and coupling strength ($\Gamma_{\mathrm{S(D)}}$) allowing tunnelling onto and off from the QD. A third Gate contact is only capacitively coupled to the dot and can be used to induce a charge on the dot.

shown in Figures 2.13(b):2.13(c). As a defect free carbon nanotube has a four-fold degeneracy of its energy levels due to the two-fold spin degeneracy of the two orbital states, we expect a four-fold degeneracy of the oscillation of conductance with gate voltage, as the addition of an electron into an energy level with an available state is equal to U_{C}, while the addition of an electron to the next energy level of the QD will be $U_{\mathrm{C}} + \Delta E$ where ΔE is the energy spacing of the QD. An example of this four-fold symmetry of coulomb blockade oscillation is shown in Figure 2.11. Although often in devices the orbital degeneracy is lifted due to mixing of the K states of the tube, either by defects in the tube or interaction with the contacts leaving a spin degenerate 2 fold state[56].

The line shape of the coulomb resonances is broadened by applied source-drain bias due to the offset between the chemical potential of the electrodes. We assume the electronic occupation of the electrodes is described by a Fermi function, which becomes a step function at low temperatures where the electronic states are filled up to a chemical potential $\mu_{\mathrm{S(D)}}$. A bias applied to source and drain offsets the chemical potentials allowing a larger range of gate voltage over which the QD energy level is between the levels of the electrodes. However we also see coulomb blockade resonance of finite width at zero bias. In the case $\hbar\Gamma \ll k_B T \ll \Delta E$ the peak broadening is dependent on temperature and the line shape is given by[57]:

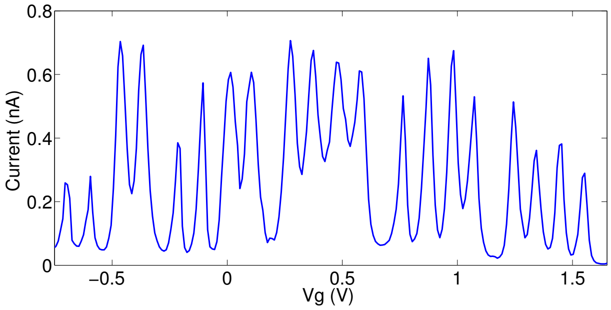

Figure 2.11: Current flow through a device at V_{SD}=15 mV taken at 1.4 K showing four-fold symmetry of coulomb blockade resonances.

$$G = \frac{e^2}{4k_B T}\frac{\Gamma_{\mathrm{S}}\Gamma_{\mathrm{D}}}{\Gamma_{\mathrm{S}}+\Gamma_{\mathrm{D}}}\cosh^{-2}\left(\frac{\Delta_{\mathrm{min}}}{2k_B T}\right)$$

where Δ_{min} is proportional to the Fermi energy of the electrodes and zero at a coulomb blockade resonance and the full-width half-maximum (FWHM) of the coulomb resonance is $\sim 3.5\ k_B T$. In the case $k_B T \ll \hbar\Gamma \ll \Delta E$ the line shape of the coulomb resonances is broadened by the coupling to the electrodes, known as life time broadening. This is due to the energy-time uncertainty $\Delta E \cdot \Delta t \geq \hbar/2$ and the line shape of the resonance has the Breit-Wigner form[57]:

$$G = \frac{4e^2}{\hbar} \frac{\Gamma_{\text{S}}\Gamma_{\text{D}}}{\Gamma_{\text{S}} + \Gamma_{\text{D}}} \cdot \frac{\Gamma_{\text{S}} + \Gamma_{\text{D}}}{(\epsilon/\hbar)^2 + ((\Gamma_{\text{S}} + \Gamma_{\text{D}})/2)^2}$$

where ϵ is the difference in energy of the energy level in the QD and the electrodes. From this dependence we can extract the FWHM of the coulomb resonance to be $\Gamma_{\text{S}} + \Gamma_{\text{D}}$.

As can be seen from Figure 2.13 conduction through a carbon nanotube QD is dependent on an energy level of the quantum dot being between the chemical potentials of source and drain electrodes and we have considered the conduction of the QD as a function of gate voltage as the induced charge on the dot moves the energy levels through the bias window of source and drain. In addition to this the charging energy of the dot can also be overcome using applied source drain bias (V_{SD}) as the offset in chemical potential between the electrodes is $\mu_{\text{S}} - \mu_{\text{D}} = -e \cdot V_{\text{SD}}$. Steps in the current-voltage characteristics of the device are referred to as the coulomb staircase and correspond to states becoming available for transport in the V_{SD} bias window. The applied bias needed to overcome the coulomb blockade is obviously dependent on the position of the energy levels of the quantum dot and the steps of the coulomb blockade staircase correspond to areas of high differential conductance. To extract parameters from the QD differential conductance, it is often plotted as a function of V_{SD} and V_{g}, often referred to as the QDs stability diagram. A schematic representation of this is shown in Figure 2.12, where the light grey shaded diamonds are areas where coulomb blockade is stopping current flow in the device and the red lines represent areas of large differential conductance corresponding to a energy level of the dot moving into the V_{SD} bias window. The four fold symmetry of the device can be seen in the increased size of every fourth diamond because of the increased level spacing of the QD.

As V_{SD} is applied directly to the QD, the charging energy can be extracted directly as the height of the coulomb diamond multiplied by the electron charge, whereas to equate the gate voltage to an energy we must find the gate coupling α, where $\alpha = \frac{U_{\mathrm{C}}}{E_{\mathrm{add}}} = \frac{C_{\mathrm{G}}}{C_{\Sigma}}$. Alternatively α can be found from the gradients of the high differential conductance lines $\alpha = \frac{\beta_+ |\beta_-|}{\beta_+ + |\beta_-|}$, where the β values can also be used to be the capacitative coupling of the source and drain electrodes to the QD.

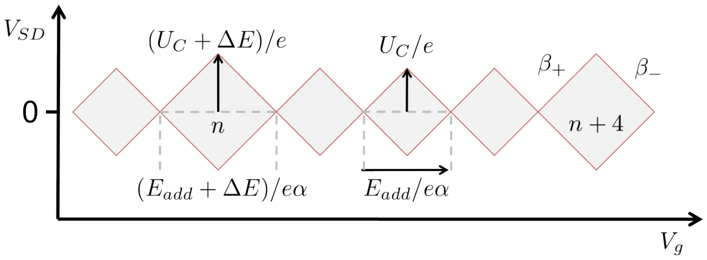

Figure 2.12: Coulomb blockade stability diagram for a carbon nanotube QD with four-fold symmetry. Grey diamonds are blocked regions where the charge on the dot is fixed and no current can flow and red lines represent regions of high differential conductance ($\mathrm{d}G/\mathrm{d}V_{\mathrm{g}}$) beyond which current flows. Some intrinsic parameters of the QD can be extracted from the measurements shown.

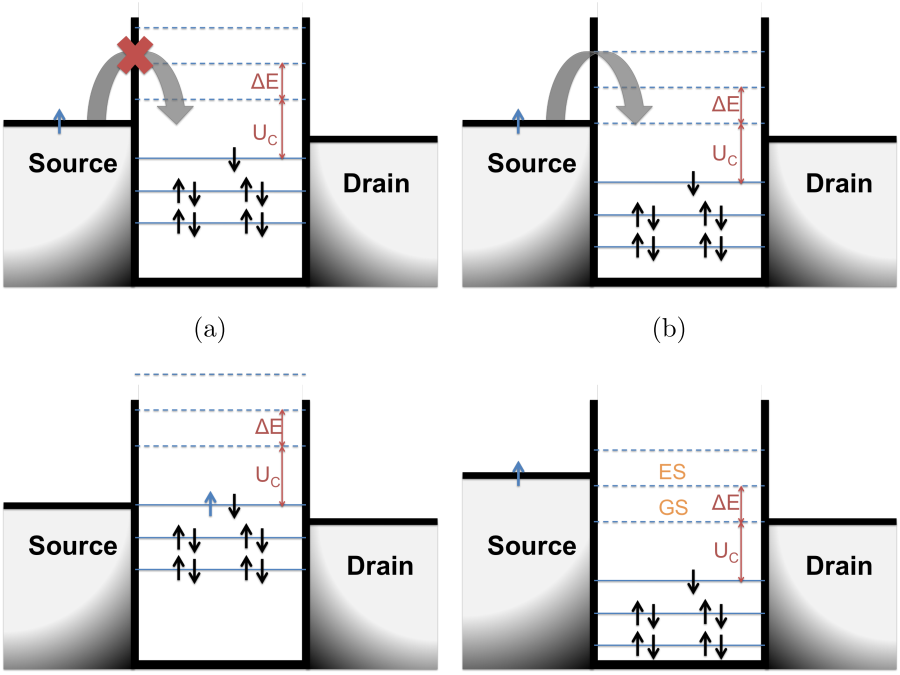

(a) (b)

(c) (d)

Figure 2.13: Energy diagrams representing a carbon nanotube between two metal electrodes. In (a) transport is blocked through the tube as there is no available energy level between the source and drain potentials of the electrodes. The states below the source-drain levels are filled apart from the top level which has a single electron in it, the energy levels are separated by a spacing ΔE with a larger gap U_C being the charging energy taken to put an extra electron onto the quantum dot. In (b-c) a gate voltage tunes the energy levels in the nanotube so an available level is between the source-drain energy levels, allowing transport through the tube. If the voltage applied to the source-drain electrodes is increased further as in (d) excited states of the nanotube can be probed[19].

As shown in Figure 2.13(d) for large V_{SD} excited states are available for transport through the QD, in this case as $V_{\mathrm{SD}} < 2U_{\mathrm{C}}/e$ only single electron tunnelling is allowed though the dot as the addition of one electron to the dot would move the excited states out of the source-drain bias window, but the increased number of states available means the conductance through the device is higher. This can be seen in the differential conductance of the device as shown in Figure 2.14, where excited states are offset from the ground state by ΔE.

SWCNTs and MWCNTs may be differentiated using transport measurements by the ratio $\Delta E/U_{\mathrm{C}}$ as the intrinsic level spacing of un-doped CNTs is independent of diameter and varies with L the length of the CNT QD. While the charging energy is dependent on the capacitance between the CNT and the electrodes, meaning MWCNTs which have larger diameters and electron overlaps than SWCNTs tend to have a lower U_{C} and higher $\Delta E/U_{\mathrm{C}}$ ratio[58].

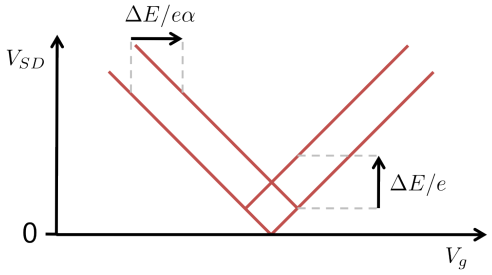

Figure 2.14: Excited states of a QD shown as red lines of high differential conductance beyond the edges of the coulomb blockade diamonds[55].

The charging energy of a SWCNT QD can be estimated from the capacitive coupling, which is dependent on the length of the CNT that forms the QD. For couplings of 50 af/L →100 af/L calculated for SWCNTs of differing diameters[19, 59] the charging energy lies in the range 3-7 meV/L where L is the length of the tube in μm. The intrinsic energy level spacing of an un-doped, metallic CNT is given by[50, 58]:

$$\begin{aligned} \Delta E &= hv_F/2L \\ &\approx 1.8 \text{ meV}/L. \end{aligned}$$

2.3 Spintronics

Spintronic devices are such that the electron transport through them is dependent on the spin polarisation of the current, where spin is an intrinsic property of an electron analogous to an angular momentum. As such spintronic devices must include a method of generating a spin-polarised current, where the simplest way of doing this is passing the current through a ferromagnetic material as they have a spin-split density of states (DOS) at the Fermi level, giving them a majority and minority carrier[60].

The origin of the ferromagnetism of transition metals is described by the Stoner model in which we consider the band structure of the metal to be separated into a spin up and spin down band. In molecular field theory electron spins are influenced by an average exchange field λM, which is produced by the electron spins. The interaction responsible is exchange and Stoner expressed this as an enhancement of the Pauli paramagnetism χ_P and this magnetisation of the electron gas produces the exchange field. This is a cyclic argument, so to resolve whether ferromagnetism occurs we will consider the change in energy of the system between no spin splitting of the spin sub-bands and a small spin-splitting caused by a movement of electrons from the down spin band to the up spin band. A system will always tend to minimise its energy so we will expect spontaneous ferromagnetism if this movement of electrons causes an overall reduction in energy of the system. The change in kinetic energy associated with a movement of electrons from $E_F - \delta E$ in the spin down band to $E_F + \delta E$ in the spin up band is given by[61]:

$$\Delta E_{KE} = \frac{1}{2} g(E_F)(\delta E)^2$$

This movement changes the number density of up and down spins to:

$$n_\uparrow = \frac{1}{2}n + \frac{1}{2}g(E_F)\delta E$$

$$n_\downarrow = \frac{1}{2}n - \frac{1}{2}g(E_F)\delta E$$

where n is the number density of electrons in the paramagnetic case. As each electron has a magnetic moment equal to the Bohr magneton μ_B, the magnetisation is given by:

$$M = \mu_B(n_\uparrow - n_\downarrow)$$

The potential or molecular field energy is then:

$$\begin{aligned}\Delta E_{PE} &= -\int_0^M \mu_0(\lambda M')dM' \\ &= -\frac{1}{2}\mu_0 M \cdot \lambda M \\ &= -\frac{1}{2}\mu_0 \lambda M^2 \\ &= -\frac{1}{2}\mu_0 \mu_B^2 \lambda (n_\uparrow - n_\downarrow)^2\end{aligned}$$

Substituting $U = \mu_0 \mu_B^2 \lambda$, where U is a measure of the exchange we obtain:

$$\Delta E_{PE} = -\frac{1}{2}U \cdot (g(E_F)\delta E)^2$$

So the total change in energy of the system due to the spin-flipped electrons is:

$$\begin{aligned}\Delta E &= \Delta E_{KE} + \Delta E_{PE} \\ &= \frac{1}{2}g(E_F)(\delta E)^2 - \frac{1}{2}U \cdot (g(E_F)\delta E)^2 \\ &= \frac{1}{2}g(E_F)(\delta E)^2(1 - Ug(E_F))\end{aligned}$$

A spontaneous spin splitting is expected for $\Delta E < 0$ in which case:

$$Ug(E_F) \geq 1$$

This is known as the Stoner criterion for ferromagnetism and tells us that for spontaneous ferromagnetism to occur exchange must be strong and the density of states must be large at the Fermi energy. This condition is fulfilled for the three transition metals cobalt, iron and nickel, mainly due to their large density of states at the Fermi energy. The three elements exhibit a spin splitting of Δ, equal to the exchange splitting in the absence of a magnetic field.

The spin splitting in ferromagnets leads to separate electron transport behaviour for the two spin sub-bands as first proposed by Mott[62]. This leads to the formation of two independent current channels in parallel, the resistivity of which

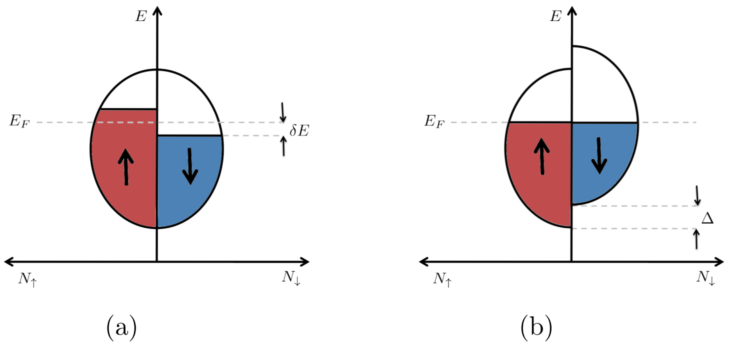

(a) (b)

Figure 2.15: Schematic representation of spontaneous ferromagnetism. (a) Down spin electrons between E_F and $E_F - \delta E$ move into the up spin sub-band (b) Assuming the total energy of the system is lowered by the movement of electrons the two spin sub-bands are offset by the exchange splitting Δ and have differing densities of states at the Fermi level.

are:

$$\rho_{\uparrow(\downarrow)} = \frac{m_{\uparrow(\downarrow)}}{n_{\uparrow(\downarrow)} e^2 \tau_{\uparrow(\downarrow)}}$$

The total resistivity of the two channels in the absence of spin mixing[63] is:

$$\rho_{total} = \frac{\rho_\uparrow \cdot \rho_\downarrow}{\rho_\uparrow + \rho_\downarrow}$$

The spin asymmetry of the resistivity of the two conduction channels is characterised by the coefficient $\alpha = \rho_\downarrow / \rho_\uparrow$.

The change in resistance of a ferromagnetic material with field (magnetoresistance) is dependent on the angle between the magnetisation and the current direction θ_{IM} and is known as the anisotropic magnetoresistance[64] (AMR) for this reason. The origin of the AMR lies in the s-d scattering of electrons due to spin-orbit coupling in the material due to the applied field, without this spin-orbit interaction scattering of the majority s electrons into d states cannot occur as there is no mixing of s and d states. Due to conservation of momentum of the scattered electrons, the scattering cross section is different for a current parallel to the ferromagnetic magnetisation than for a current perpendicular to the magnetisation due to the orbital anisotropy of the d states. The resistance of the ferromagnet is at a maximum when the current is parallel to the magnetisation direction and at a minimum when the current is perpendicular to the magnetisation with an angular dependence of:

$$R(\theta_{IM}) = R_{\min} + \Delta R_{AMR} \cdot \cos^2(\theta_{IM})$$

We have identified ferromagnets as a source of spin-polarised currents, but to be useful these currents must be transported between ferromagnets via other materials. When a current of density j flows between a ferromagnet (F) and a normal metal (NM) its distribution of spin up and spin down electrons must change as the bulk spin polarisations for the two materials differs, this leads to a discontinuity in the spin-dependent chemical potential ($\Delta\mu_{\uparrow(\downarrow)}$) at the interface of the materials as shown in Figure 2.17(b). The chemical potential discontinuity leads to a spin accumulation when a spin polarised current flows and is defined as[65]:

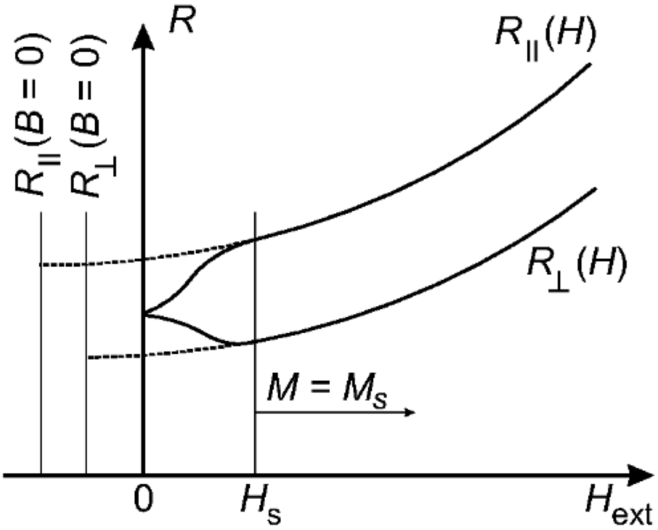

Figure 2.16: Resistance as a function of applied field for current parallel to the field ($R_{||}$) and current perpendicular to the field ($R_{\perp}$). Taken from Getzlaff[64].

$$j\uparrow(\downarrow) = -\frac{\sigma_{\uparrow(\downarrow)}}{e} \bigtriangledown \mu_{\uparrow(\downarrow)}$$

where current polarisation is given by:

$$P_j = \frac{j_\uparrow - j_\downarrow}{j_\uparrow + j_\downarrow}$$

With the spin asymmetry of the conduction characterised by $j_\uparrow = \beta j$ and $j_\downarrow = (1-\beta)j$. Assuming that the rate of scattering events of the two channels is far larger than the spin-flip scattering rate (τ_{sf}^{-1}) allows the chemical potentials of the conduction channels ($\mu_{\uparrow(\downarrow)}$) to differ, with a gradient determined by the current of the channel:

$$\frac{\delta\mu_{\uparrow(\downarrow)}}{\delta x} = -(e/\sigma_{\uparrow(\downarrow)})j_{\uparrow(\downarrow)}$$

where x is the distance from the barrier. Recalling α, the spin asymmetry of the conductance defined previously, we see this as an intrinsic property of the material, which changes abruptly at the FM/NM interface, whereas β is continuous. Far from the interface in the two materials the 2 spin bands are in equilibrium and $\beta = \alpha$, while at the boundary $\delta\beta/\delta x \neq 0$ and the spin bands are at separate chemical potentials. This potential difference between the bands is the motive force of the current conversion and obeys the diffusion equation in the steady state:

$$(\mu_\uparrow - \mu_\downarrow)/\tau_{sf} = D\frac{\delta^2(\mu_\uparrow - \mu_\downarrow)}{\delta x^2}$$

where $D = \frac{1}{3}v_F l$ is the diffusion constant and l the mean-free path. The potential difference $(\mu_\uparrow - \mu_\downarrow)$ can then be seen to decay exponentially from the interface on the scale of the spin diffusion length $\Lambda = (D\tau_{sf})^{\frac{1}{2}}$. Defining the average chemical potential of the two bands in each material as $\mu_0 = \alpha\mu_\uparrow + (1-\alpha)\mu_\downarrow$, the resistance of the interface can be simply found from the difference in μ_0 at the interface and the current[65]:

$$\begin{aligned} R_I &= \frac{\mu_\uparrow - \mu_\downarrow}{ej} \\ R_I &= \frac{(2\alpha_F - 1)^2(\sigma_N^{-1}\Lambda_N)(\sigma_F^{-1}\Lambda_F)}{(\sigma_F^{-1}\Lambda_F) + 4\alpha_F(1-\alpha_F)(\sigma_N^{-1}\Lambda_N)} \end{aligned}$$

So we see that spin accumulation can cause spin-split states in a NM at distances from the interface with a FM far larger than the mean-free path and that an interface resistance is caused by the chemical potential drop across the interface

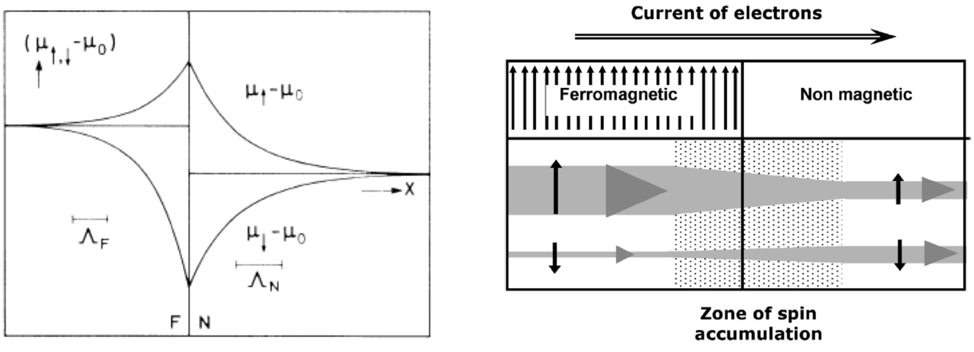

(a) (b)

Figure 2.17: (a) Change in spin dependent chemical potentials for a ferromagnet-normal metal interface due to current flow between the materials. Taken from van Son et al. 1987 (b) Spin polarisation of electrons across a ferromagnet-normal metal interface driven by current flow. (a) Taken from van Son et al.[65]. (b) Taken from Schuhl et al.[66]

even when good Ohmic contact is made between the materials.

Introducing a finite contact resistance into the interface modifies the spin-transport and the current polarisation can be written as[67]:

$$P = \frac{r_C P_C + r_F P_F}{r_F + r_C + r_N}$$

where:

$$r_F = \frac{L_{SF}\sigma_F}{4\sigma_\uparrow\sigma_\downarrow} \quad \text{and} \quad r_N = \frac{L_{SN}}{\sigma_N}$$

With r_C the contact resistance of the interface and P_C the associated polarisation. This is not the same as the interface resistance that occurs in a transparent Ohmic contact where $r_C = 0$ and for an Ohmic contact reduces to the interface resistance as defined previously. This relationship between polarisation and contact resistance illustrates the conductivity mismatch problem, as if $r_F \ll r_N$ then $P \sim r_F/r_N \ll 1$. This equation also shows how the introduction of a tunnel barrier between the ferromagnet and normal metal can overcome this spin injection problem.

Giant magnetoresistance (GMR) was discovered by Baibich et al.[68] and simultaneously by Binash et al.[69] in iron-chromium multilayers. The results from

Baibich et al. are shown in Figure 2.18 where a large change in resistance is observed between the zero field case and the saturated state H_{S}, as the Fe layers that are anti-parallel (AP) at $H = 0$ due to the anti-ferromagnetic ordering induced by the Cr are pulled into a parallel (P) state. This large change in resistance between P and AP states can be explained by Mott's two band conduction model if we consider the scattering and hence resistance of the two channels in the two configurations. Simplifying the multilayers to a 3 layer ferromagnet/normal metal/ferromagnet (FM/NM/FM) system as shown in Figure 2.19 with an electron mean free path for each spin channel which is greater than the layer thickness so the scattering is averaged over the structure. It is assumed that the scattering caused by interface potentials and other sources is spin-dependent and weighted by the density of available states. In the P case, the majority spin electrons are weakly scattered when passing through each layer, making the channel resistance 2r much smaller than for the minority carrier which is scattered at each interface and in the bulk of each magnetic layer and has a channel resistance of $2R$, making the resistance of the parallel state $R_{\mathrm{P}} = 2rR/(r + R) \sim 2r$. In the AP state each of the spin channels alternates, being minority and majority through the stack, making the averaged resistance through the stack $R_{\mathrm{AP}} = (R + r)/2$. The GMR is defined as:

$$GMR = (R_{\mathrm{AP}} - R_{\mathrm{P}})/R_{\mathrm{P}}$$

Large GMR values are associated with combinations such as Fe/Cr and Co/Cu, where the band matching of the materials is important and the majority spin-bands are nearly full.

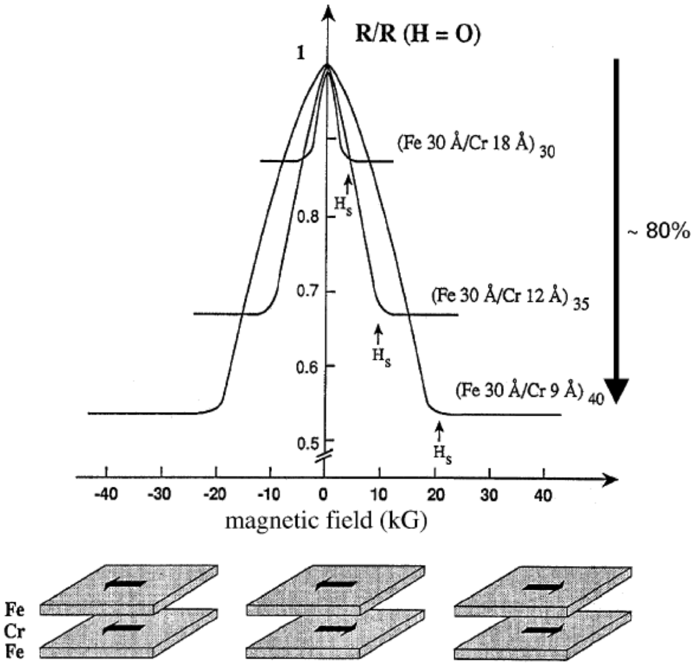

Figure 2.18: GMR in Fe/Cr superlatices at 4.2 K, resistance is normalised to $R(H = 0)$ and shows the antiparallel alignment of layers at zero field, which then rotate to parallel at H_{S}, the saturation magnetisation of the stack. Taken from Baibich et al.[68]

GMR spin valves employ normal metal layers between the ferromagnetic layers. When replacing this normal layer with a tunnel barrier a similar spin valve effect is observed, with high conductance when the magnetic layers are parallel and low conductance when they are anti-parallel. Tunnelling was first observed by Giaver [70] when measuring the BCS gap in superconductors and later by Julliere[71] in ferromagnets. In this case the origin of the magnetoresistance is not scattering as in GMR but is dependent on the density of states (DOS) of the spin sub-bands of the ferromagnets. As shown in Figure 2.20 assuming the tunnelling between the two ferromagnetic layers preserves the spin of the electrons, in a parallel configuration the majority spin have a large number of available states to tunnel into and the minority carriers have a small number of available states. In the AP configuration the majority carriers have a small number of available

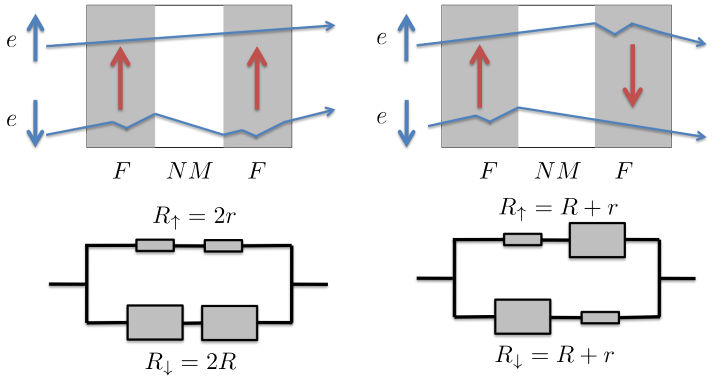

Figure 2.19: Scattering description of GMR in spin valves. Straight electron paths through the stack shown in blue represent low scattering, whereas deviations in the electron path represent increased scattering in the bulk or at interfaces. The two parallel spin channels and their interface resistance are shown below, with large resistors representing increased scattering.

states to tunnel into and the minority carriers have a large number. Defining $a_{M(m)} = g(E_F)_{M(m)}/g(E_F)_{total}$ as the proportion of majority (M) and minority (m) states at the Fermi energy we obtain[72]:

$$\begin{aligned} G_{\text{P}} &\propto a_{MS}a_{MD} + a_{mS}a_{mD} \\ G_{\text{AP}} &\propto a_{MS}a_{mD} + a_{mS}a_{MD} \end{aligned}$$

This leads us to Julliere's formula:

$$MR = \frac{G_{\text{P}} - G_{\text{AP}}}{G_{\text{AP}}} = \frac{2P_1P_2}{1 + P_1P_2}$$

where P_1 and P_2 are the respective spin polarisations of the two magnetic layers. Figure 2.21 shows an example of the TMR between two magnetic layers of CoFe and Co through an Alumina tunnel barrier[73]. The hysteretic magnetoresistance seen is due to the differing coercive fields of the magnetic layers, H_{S1} and H_{S2} between which an anti-parallel alignment of the magnetisations is obtained, as shown by the arrows on the Figure.

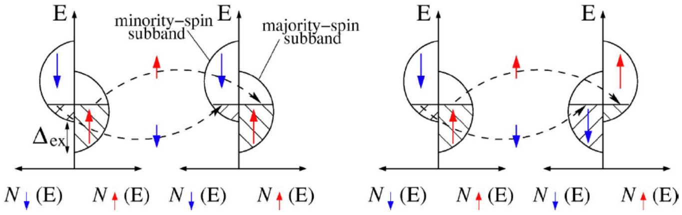

Figure 2.20: Spin dependent tunnelling between two ferromagnetic layers aligned parallel and anti-parallel (alignment indicated by the spin of the majority subband). Taken from Zutic et al.[67]

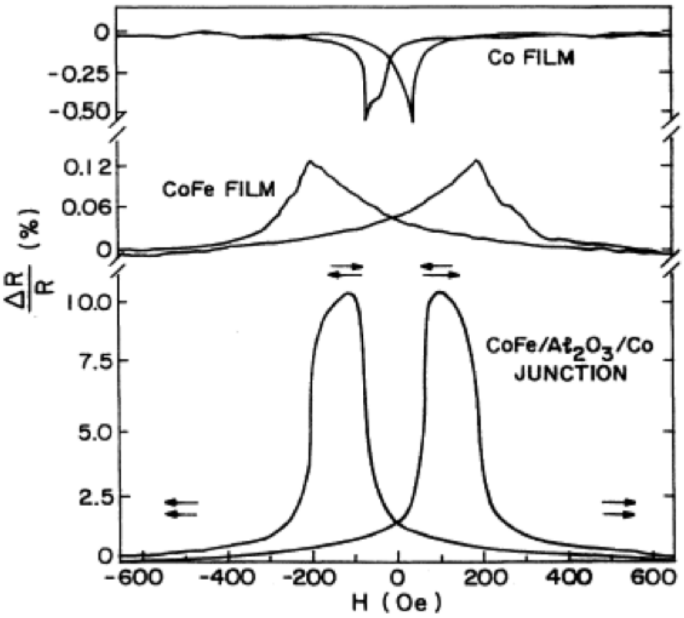

Figure 2.21: Resistance of a CoFe/Al_2O_3/Co structure at room temperature, including AMR measurements on the CoFe and Co films showing the difference in coercive field of the two layers. Taken from Moodera et al.[73]

2.4 Carbon Nanotubes and Magnetism

Due to the structural symmetry of carbon nanotubes the two non-equivalent axes for applied fields are parallel to the axis of the tube: along the translational vector and perpendicular to the tube axis. When considering the interaction of the four-fold degenerate ground state of the quantised energy levels, when a field is applied parallel to the tube we have to take into account the orbital motion of electrons[74, 75]. States with a positive $\boldsymbol{k}_\perp$ rotate around the circumference in the opposite direction to those with negative $\boldsymbol{k}_\perp$ with a velocity $v_{orb} = \frac{1}{\hbar}\frac{\mathrm{d}E}{\mathrm{d}k_\perp}$ defining the motion as clockwise (CW) or anti-clockwise (ACW). Considering the states closest to the Fermi level of the tube we find the K point states to have an opposite orbital velocity to those around the K' points with the K band states having an ACW rotation in the conduction band and a CW rotation in the valence band. As each CW(ACW) orbit for K point states has an equal energy ACW(CW) partner in the K' point states the two sub-bands are degenerate.

The magnetic moment produced by the rotating charge in these orbits $\mu_{orb} = Dev_F/4$[76] is directed along the tube axis, where D is the diameter of the rotation. When the orbital magnetic moment interacts with a parallel applied field the energy of the states is shifted by:

$$\Delta E_{orb} = -\mu_{orb} \cdot B = \pm\frac{Dev_F B_\parallel}{4}$$

This energy splitting lifts the orbital degeneracy of the four-fold ground state as shown in Figure 2.22, where a large splitting of the two orbital states with $B_\parallel$ is seen together with a smaller splitting of the orbital sub-bands due to the Zeeman shift of the electron spins.

For a magnetic field applied perpendicular to the tube axis ($B_\perp$)[77, 78] there is no coupling to the orbital moment and we expect to see a Zeeman splitting of the two-fold spin degenerate levels of $E_Z = g\mu_B B_\perp$, with $g = 2$ expected for the electrons in a nanotube with no orbital angular momentum[78, 79, 80, 81], but with lower values of $1 \geq g \leq 2$ also having been observed[82]. In this case the two spin-split levels will be orbitally degenerate as shown in Figure 2.23(a).

Introducing disorder into the model of the carbon nanotube quantised energy

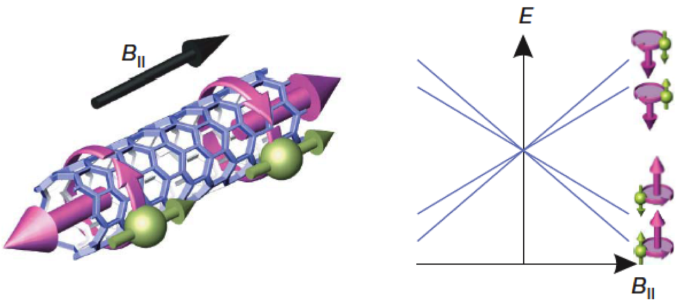

Figure 2.22: Current direction and orbital magnetic moment (purple arrows) of electrons arising from their rotation around the tube, green arrows representing the electrons intrinsic spin and the expected splitting of the carbon nanotubes four fold degenerate ground state due to orbital moment and spin in a parallel magnetic field. Taken from Kuemmeth et al.[74]

states produces mixing of the K and K' energy levels. The disorder induced coupling lifts the orbital degeneracy of the energy levels of the tube and produces a splitting of the orbital energy levels equal to $\Delta_{KK'}$ at zero field. The modification of the four orbital and spin states by a magnetic field applied perpendicular or parallel to the tube is shown in 2.23(b), where the spin degenerate energy levels are Zeeman split for $B_{\perp}$, whereas they are both orbitally and Zeeman spit for $B_{\|}$.

The four-fold degeneracy of the ground state can also be lifted by spin-orbit coupling of the electrons, in which the electron spin couples with the orbital moment of the sub-band to form two Kramer doublets $(K\downarrow, K'\uparrow)$ and $(K\uparrow, K'\downarrow)$. The splitting is equal to the spin-orbit coupling Δ_{SO} and the dictates which pair has a lower energy. In Figure 2.23(c) we see $B_{\|}$ splits the Kramer pair depending on their orbital sub-band, whereas $B_{\perp}$ shows no splitting of the pairs as it does not couple K and K'. This means measurements of g in the perpendicular orientation may vary from zero when $\Delta_{SO} \gg \Delta_{KK'}$ to 2 in the opposite case[56].

Including both a dominant disorder and spin-orbit interaction ($\Delta_{KK'} > \Delta_{SO}$) into the model of the energy levels produces the magnetic field dependence shown in Figure 2.23(d), where at zero field we observe two spin degenerate states split by $\sqrt{\Delta^2_{KK'} + \Delta^2_{SO}}$, which become spin-split in a perpendicular field, but unlike the case which only includes disorder, do not cross at high $B_{\perp}$, due to the suppression

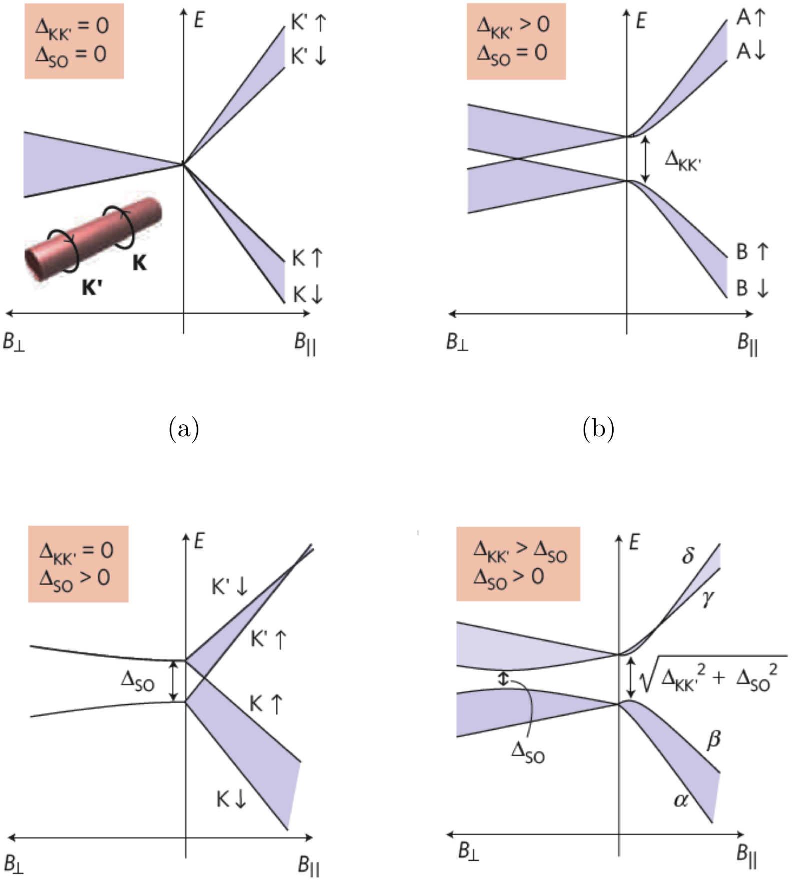

(a) (b)

(c) (d)

Figure 2.23: Effects of spin orbit interaction and disorder in the spin and orbital energy levels of a carbon nanotube in a parallel and perpendicular applied field. Considering the case of no spin-orbit or disorder (a), disorder (b), spin orbit (c) and both spin-orbit and a dominant disorder ($\Delta_{KK'} > \Delta_{SO}$) (d) Taken from Jesperson et al.[56]

of the splitting by the spin-orbit coupling. While in a parallel field the spin-orbit interaction is responsible for the asymmetric splitting of the Kramer doublets (α, β) and (γ, σ)[56].

The relationship between the disorder and spin orbit coupling of the four-fold ground state of carbon nanotubes is relevant when considering the periodicity and shell filling of carbon nanotube QDs[83]. The expected filling for a carbon nanotube with no disorder or spin-orbit coupling is similar to that of an atom in that the occupation order of the energy level should follow Hund's rules. Hund's first rule states that electrons should be arranged to maximise S, the total spin of the system as this minimises the coulomb energy due to the Pauli exclusion principle preventing electrons with parallel spins occupying the same orbital shell. Therefore we expect the first two electrons to be added to the QD to be the same spin and half fill each of the orbitals, the next two electrons with then have opposite spin to the first two and fill the remaining two available states. When applying a perpendicular magnetic field the four states are Zeeman shifted up or down depending on their spin, with the lower two states having spin aligned with the field and the next two aligned opposite it. Figure 2.24(a) shows results from Makarovski et al.[84] where this shell filling sequence is observed in the upper set of four states (I), with the separation of the states, or addition energy, shown in 2.24(b).

The lower four states (II) in Figure 2.24(a) show the effect of disorder on the shell filling. In this case the energy gap $\Delta_{KK'}$ lifts the orbital degeneracy and the states fill with alternating spin values in the lower energy orbital, then the higher energy orbital at $B_{\perp} < 4$ T. At high field the Zeeman shift overcomes the orbital splitting, reverting the shell filling order to that seen in group (I), with the Zeeman shift at the switching point allowing the orbital splitting to be found $\Delta_{KK'} = 0.5$ meV. Shell filling with alternate spin that is overcome by an applied perpendicular field has also been reported in the work of Moriyama et al.[80]. In both these examples the disorder has been shown to be dependent on the number of electrons in the QD, which leads to the breaking of the four-fold symmetry of the coulomb resonances. If the disorder was constant for all electron shells we would expect to see the addition energy to vary over the four electrons added to each orbital, but still observe a four-fold symmetry in the addition energy,

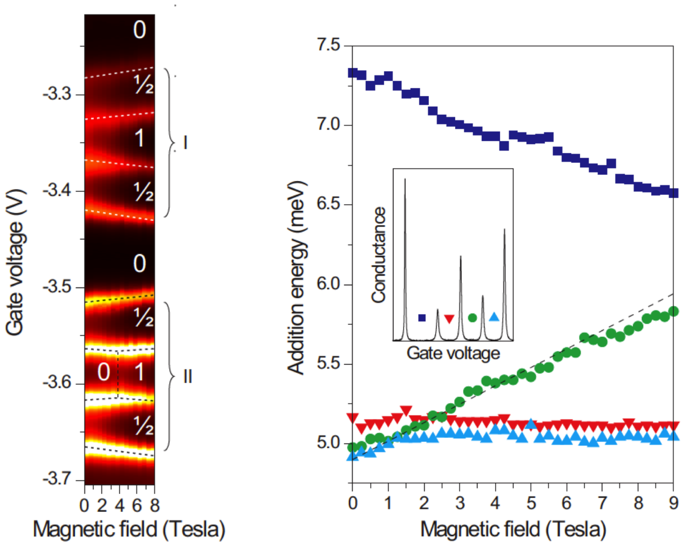

(a) (b)

Figure 2.24: (a) Zero bias conductance of a carbon nanotube QD as a function of V_{g} and $B_{\parallel}$ showing the Zeeman shift of the energy levels, lighter colours indicate higher conductance. (b) The addition energy of four states similar to group (I) in (a). Taken from Makarovski et al.[84]

whereas for changing disorder, this can be broken.
At finite bias (e$\cdot V_{\mathrm{SD}} > \Delta E$) the excited states of the QD can be probed. This allows the observation of the Zeeman splitting of the QD energy levels if they lie between the chemical potentials of source and drain. Including disorder in the energy levels for an alternate spin filling of the electron orbitals means that the levels at the edges of the coulomb diamonds, that correspond to an even number of electrons in the dot (S=0) are split, as shown in Figure 2.25 as the electron added to the dot may be spin up or spin down. The levels at the edges of the diamonds that correspond to an odd number of electrons are not split, as the spin of the previous electron added to the dot fixes the spin of the next available energy level. The un-split energy levels are still Zeeman shifted in this case[85].
In the case of no disorder, the energy level splitting will be observed when electrons are tunnelling into an unoccupied orbit for the first two electrons added to the dot, on the other hand there will only be a Zeeman shift in the energy of the next two electrons added to the dot.

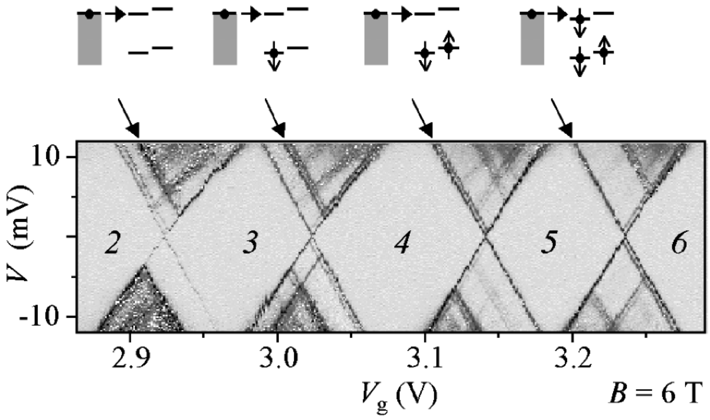

Figure 2.25: Coulomb blockade stability diagram for a carbon nanotube at 100 mK with a perpendicular field of 6 T. The edges of the odd n diamonds are not Zeeman split as is expected for a CNT with alternate spin filling, as shown by the energy level diagrams above. Taken from Cobden et al.[85]

Having discussed the effects of applied magnetic field on the energy levels in the dot itself, now we must consider the effect of applied field on the magnetic pads. For non-magnetic pads in an applied field, the up and down spin sub-bands are shifted by the Zeeman energy but due to their lack of spin-polarisation, the shift does not cause an overall energy shift in the pad. For ferromagnetic pads with spin polarisation we expect the chemical potential to shift by $\Delta\mu = -\frac{1}{2}Pg\mu_B B$[86, 87, 88]. During device measurement the chemical potentials of the electrodes are set at values by the measurement apparatus so $\Delta\mu$ is compensated for by a movement of electrons between the NM measurement leads and the FM electrode, leaving the FM electrode at the same chemical potential as before the Zeeman shift but with a different electrostatic potential. This changed electrostatic potential produces a gate-like effect on the dot, through the capacitive coupling of the dot to the electrodes, shifting the energy by $e\Delta\Phi_{QD} = \Delta\mu_{\mathrm{S(D)}}C_{\mathrm{S(D)}}/C_{\Sigma}$ and is known as the magneto-coulomb (MC) effect[89]. Figure 2.26(a) shows the change in charge of a quantum dot coupled to two ferromagnetic electrodes. The induced charge is linear with field apart from the two discontinuities as the electrodes reverse their magnetisation, the charge on the QD is constant when the pads are aligned anti-parallel due to the assumed symmetric coupling of the electrodes and the dot and use of the same material for both electrodes. For small changes in induced charge on the island relative to the addition energy ($e\Delta\Phi_{QD} \ll E_{\mathrm{add}}$) the change in conductance of the device varies with $\frac{\mathrm{d}G}{\mathrm{d}V_{\mathrm{g}}}$ and the calculated change in conductance for a device due to the MC effect is shown in Figure 2.26(b) assuming $\frac{\mathrm{d}G}{\mathrm{d}V_{\mathrm{g}}} \neq 0$ i.e. the gate voltage is set to a value that corresponds to the slope of a coulomb resonance. In addition to the MC effect the demagnetising field of the electrodes may also play a role in the MR of the device as the carbon nanotube is buried beneath the FM electrode. The magnetic domains around the nanotube may rotate slowly with applied field before the electrode reverses magnetisation, changing the local work function of the FM and hence the charge on the dot before the electrode switches, this effect is included for positive field in Figure 2.26(b) as the dashed line.

While there is some debate about whether some results on carbon nanotube QD spin valves may be attributed to a MC effect, results published by Datta et al.[90] report the observation of this effect in double-walled carbon nanotubes

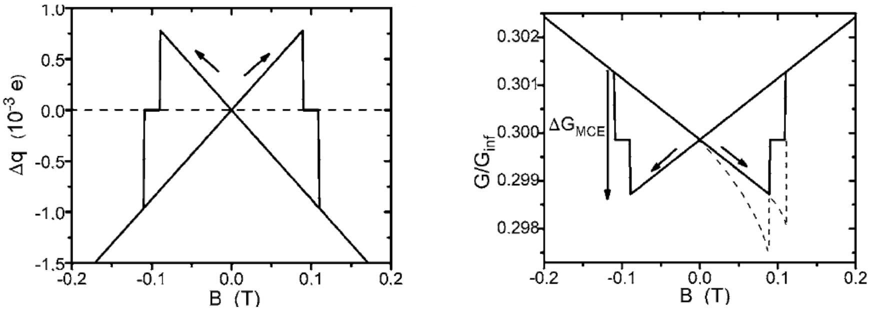

(a) (b)

Figure 2.26: (a) Induced charge on a QD due to the magneto-coulomb effect, δq is linear with field apart from the discontinuities when each of the two ferromagnetic pads reverse their magnetisation. (b) Change in conductance of a device on the slope of a coulomb resonance due to δq, dashed line is the enhancement of the change in conductance due to a demagnetising field acting on the domain at the FM-CNT junction. Taken from van der Molen et al.[86]

that contain iron nanoparticles contacted with non-magnetic electrodes, in which the changing electrostatic potential of the particles with magnetic field produces a gating effect on the tube. The changing position of the coulomb resonances of the device, as the field is swept from negative to positive values, is shown in Figure 2.27, together with two gate sweeps at different magnetic fields showing the change in effective gate voltage ΔV_{g}. MR sweeps performed on the device at three gate voltages corresponding to positive, negative and zero $\frac{\mathrm{d}G}{\mathrm{d}V_{\mathrm{g}}}$ show the expected sign and magnitude of the MR.

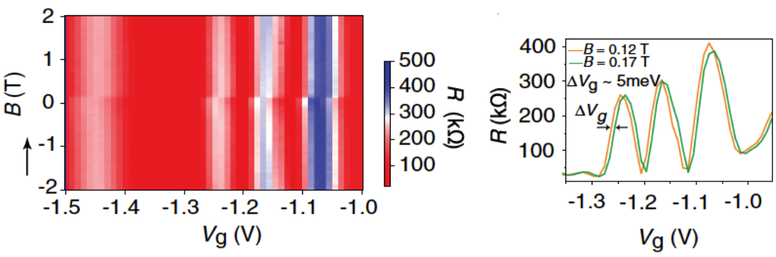

Figure 2.27: Colourscale plot of differential resistance of a double-walled CNT which contains Fe nanoparticles and is contacted to NM electrodes over a range of V_g as the magnetic field is swept from -2 T to 2 T, showing the sharp change in peak position at the coercive field of the Fe nanoparticle. Two gate voltage sweeps are also shown before and after the nanoparticle switches to illustrate the change in peak position. Taken from Datta et al.[90]

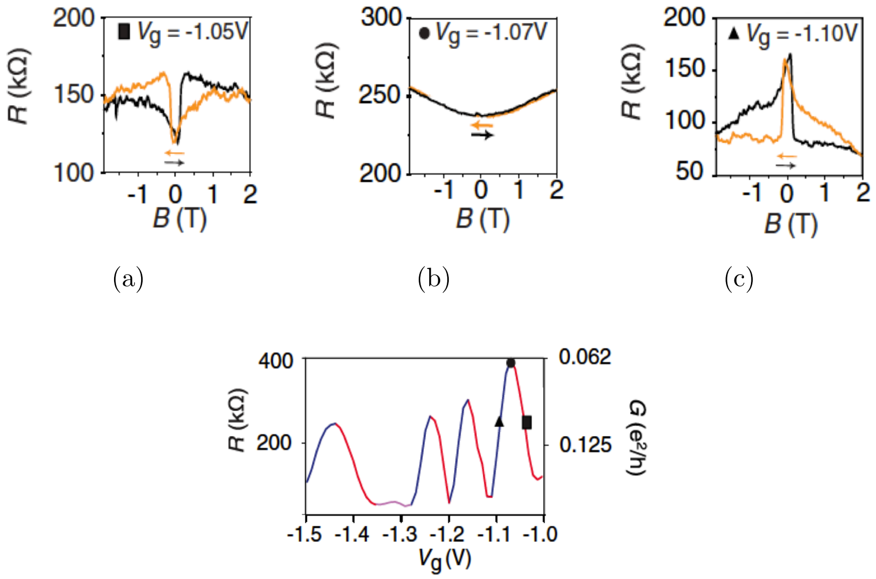

(a)

(b)

(c)

(d)

Figure 2.28: MR data taken at three gate voltages (triangle, circle and square) around a conductance minima of the device from Figure 2.27. Taken from Datta et al.[90]

When considering spin transport through a carbon nanotube Cottet et al.[91, 92] model the system as a quantum wire (QW) separated from two FM pads by tunnel barriers (TB). There is a spin (σ) dependent transmission probability ($T_l^{c\sigma}$) for electron tunnelling in a parallel or anti-parallel alignment of the ferromagnetic electrodes (c=P(AP)) of the quantum wire (l=L,R specifying the left and right contact) as shown in Figure 2.29. On reflection from the QW-FM interface a spin dependent phase shift ($\psi_l^{c\sigma}$) can occur due to the spins interaction with the FM known as the spin-dependence of interfacial phase shifts (SDIPS). This phase difference causes a spin-splitting of the energy levels in the quantum wire:

$$g\mu_B h_c^{\mathrm{SDIPS}} = E_\downarrow^c - E_\uparrow^c = \Sigma_{\mathrm{L,R}} \frac{\psi_l^{c\uparrow} - \psi_l^{c\downarrow}}{\pi N_F^M}$$

where N_F^M is the density of orbital states at the Fermi level in the wire. Figure 2.30 shows the dependence of the MR on the gate voltage applied to a QD for different values of $g\mu_B h_{\mathrm{P}}^{\mathrm{SDIPS}}$, with $g\mu_B h_{\mathrm{AP}}^{\mathrm{SDIPS}} = 0$ due to the cancellation of the phase shift of the electrons when the electrodes are in the AP state. The magnitude of the MR at $g\mu_B h_{\mathrm{P}}^{\mathrm{SDIPS}} = 0$ is approximately equal to the value predicted by Julliere's formula of $\frac{2P_1P_2}{1+P_1P_2}$. For the two resonances considered we observe the peaks moving in opposite directions due to the opposite spin of the electrons filling the levels. It is also important to note that the effect of SDIPS on the

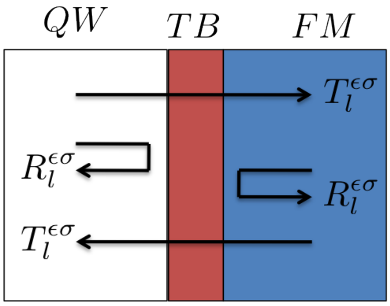

Figure 2.29: Schematic of electron transport through a tunnel barrier between a CNT and a FM electrode for parallel and anti-parallel FM configurations c=P(AP), electron spin $\sigma =\uparrow (\downarrow)$ and left or right contact l=L(R). adapted from Cottet et al.[91]

MR of a device can be large whilst still not easily resolvable in the conductance traces.

The MR for a nanotube with no disorder breaking the orbital degeneracy is

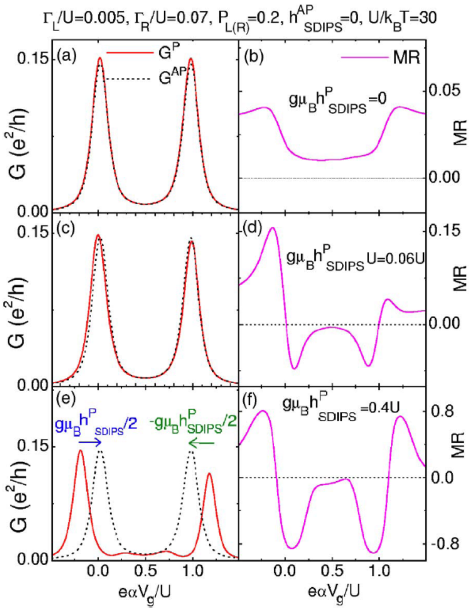

Figure 2.30: (a)(c)(e) conductance in the P(AP) configuration sown as red(black dashed) lines for a one orbital QD $h^{\rm AP}_{\rm SDIPS}=0$ due to the cancellation of phase shifts and varying $h^{\rm P}_{\rm SDIPS}$. (b)(d)(f) MR calculated from $MR=(G^{\rm P}-G^{\rm AP})/(G^{\rm P}+G^{\rm AP})$. Taken from Cottet et al.[91]

shown in Figure 2.31. The two lower values of $g\mu_B h_{\rm P}^{\rm SDIPS}$ in this case are similar to those presented in Figure 2.30 where up spin resonances move to a larger gate voltage and down spins move the opposite way. But for $g\mu_B h_{\rm P}^{\rm SDIPS}=0.3\ U_{\rm C}$ the splitting of the spin levels is larger than the line-width of the coulomb resonance, meaning Coulomb blockade does not entirely suppress the up spins contribution to the third peak. This produces a MR of the same sign for the first three coulomb resonances, which then flips for the final level.

SDIPS may enhance the MR through a carbon nanotube spin valve to beyond that expected using Julliere's model for TMR and produce a MR that oscillates with gate voltage, however it is not the only mechanism that may produce oscillating MR, which is also predicted to occur for carbon nanotube QDs in the

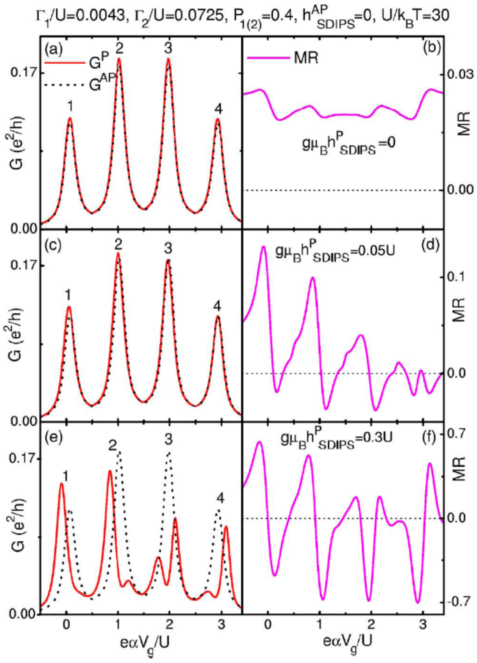

Figure 2.31: (a)(c)(e) conductance in the P(AP) configuration sown as red(black dashed) lines for a two orbital QD $h^{\rm AP}_{\rm SDIPS} = 0$ due to the cancellation of phase shifts and varying $h^{\rm P}_{\rm SDIPS}$. (b)(d)(f) MR calculated from $MR = (G^{\rm P} - G^{\rm AP})/(G^{\rm P} + G^{\rm AP})$. Taken from Cottet et al.[91]

limit of highly asymmetric tunnel barriers at either electrode by Cottet et al.[92]. Modelling the conductance of a nanotube around $E_{\rm res}$, the energy position of a coulomb resonance, in the limit of low transmission probability $T_l \ll 1$ the transmission in the P(AP) state can be found using a Breit-Wigner like formula:

$$T^{\sigma}_{\rm P(AP)} = \frac{T^{\sigma}_{\rm L} T^{\sigma}_{\rm R}}{(\pi N^{W}_{F}[E - E_{\rm res}])^2 + (T^{\sigma}_{\rm L} + T^{\sigma}_{\rm R})^2/4}$$

When the dot is off resonance ($[E - E_{\rm res}]^2 \gg (T^{\sigma}_{\rm L} + T^{\sigma}_{\rm R})^2/4\pi N^{W}_{F}$) the transmission probability of electrons through the device is proportional to $T^{\sigma}_{\rm L} T^{\sigma}_{\rm R}$, giving:

$$MR = \frac{2P_1 P_2}{1 + P_1 P_2}$$

As would be predicted by Julliere's formula, whereas on resonance ($E + E_{\rm res}$) the transmission probability is approximately equal to $4T^\sigma_{\mathrm{L}}/T^\sigma_{\mathrm{R}}$ which leads to:

$$MR = -\frac{2P_1P_2}{1+P_1P_2}$$

Figure 2.32 shows this change in MR at the coulomb resonance with no SDIPS and also the effect of including SDIPS into this model. In this case SDIPS is observed to enhance the magnitude of the MR and introduce an asymmetry to the MR about the coulomb resonance.

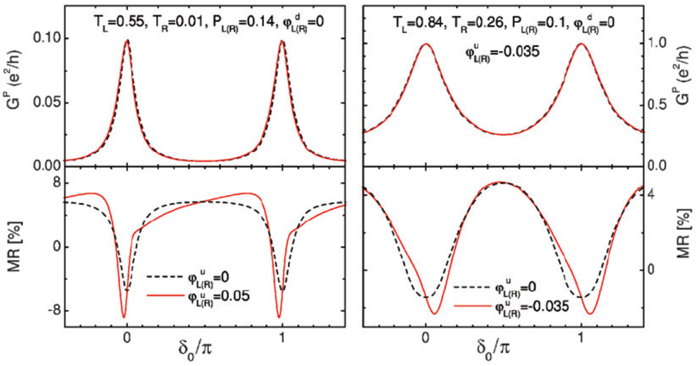

Figure 2.32: Conductance (top panels) and MR (bottom panels) defined as $MR = (G^{\mathrm{P}} - G^{\mathrm{AP}})/(G^{\mathrm{P}} + G^{\mathrm{AP}})$ for $h^{\mathrm{P}}_{\mathrm{SDIPS}} = 0$ (black dashed lines) and finite $h^{\mathrm{P}}_{\mathrm{SDIPS}}$ (red lines) for a one orbital QD with highly asymmetric coupling. Taken from Cottet et al.[91]

2.5 Published Work on Spin-Transport in carbon Nanotube Quantum Dots

Various ferromagnetic materials have been used to contact carbon nanotubes to investigate spin transport including cobalt, iron, nickel, nickel-palladium alloys, permalloy (NiFe), ferromagnetic semiconductors and half-metals.

Of the results published on Co electrodes, Tsukagoshi et al.[30, 93] present results on a small bundle of SWCNTs showing an $\sim +8\%$ MR at low temperature (1.6 K), which changed sign at 20 K and reduced with temperature up to 175 K.

The bundle showed some variation of conductance with gate voltage but MR was performed at only one V_{g} and no anisotropy of the pads was employed to create differing coercive fields and an anti-parallel aligned state. Kim et al.[94] also present MR in Co contacted SWCNTs and show a +2% MR at 200 mK, which although interpreted as due to spin transport through the device seem to more closely resemble a magneto-coulomb effect, possibly including a demagnetising field enhancement. This interpretation also seems more likely due to Co pads having the same dimensions, meaning there is no difference in coercive field. However there is also very little variation of conductance of the device with gate voltage, which would be necessary to observe a MC effect. Tombros et al.[95] present results on a four terminal Co-contacted SWCNT, shape anisotropy is used to create differing coercive fields of the contacts and a 2 terminal MR between the central two contacts of 6% is obtained, although after thermally cycling the device a negative MR is observed in the forward magnetic sweep and a positive MR in the back sweep as shown in Figure 2.33. No gate electrode is included in the device to investigate the V_{g} dependence of the MR, but non-local measurements were performed where the voltage was measured between two adjacent electrodes whilst a current was passed between the other two. These results show a change in the non-local resistance consistent with a spin-accumulation and diffusion in the carbon nanotube.

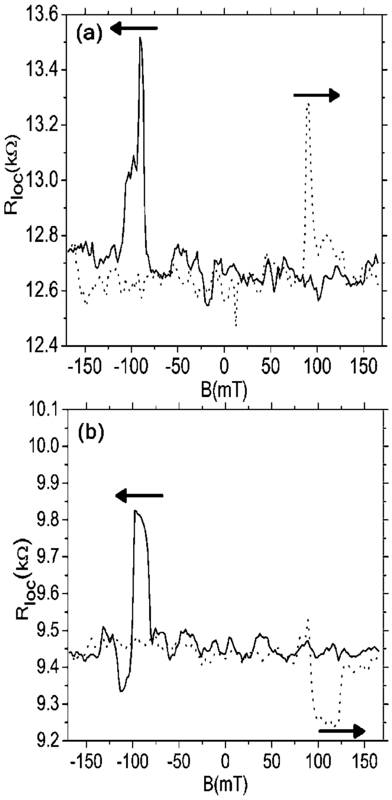

Figure 2.33: Two terminal measurements on a Co contacted CNT taken either side of thermally cycling the device, a source drain current of 10 nA was used at 4.2 K. Taken from Tombros et al.[95]

Measurements carried out using Fe electrodes by Jensen et al.[96] show oscillations in conductance with V_g and both positive and negative MR of up to 100%, depending on the applied gate voltage. The electrodes used were not patterned to create different coercive fields and the magnetoresistance obtained is attributed to spin transport due to an anti-parallel aligned domain structure that the CNT contacts. However the results shown in Figure 2.34 at $V_g = 0$ V bear a striking similarity to those in Figure 2.28(c) which show the MC effect of an Fe nanoparticle encapsulated in a double-walled nanotube.

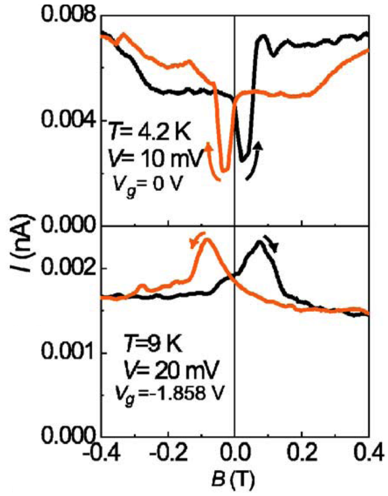

Figure 2.34: MR obtained at different gate voltages for an Fe contacted CNT with $V_{\mathrm{SD}} = 10$ mV at 4.2 K. Taken from Jensen et al.[96]

Nagabhirava et al.[97] present MR measurements over a large range of gate voltages (-3 V$\leq V_{\mathrm{g}} \leq$11 V) which vary between -15% and 10% as shown in Figure 2.35. The electrodes used had no shape anisotropy so any spin-dependent MR is assumed to originate from anti-parallel domain structure in the pads. Unfortunately in this work no clear coulomb blockade resonances can be seen in the gate voltage dependence of the conductance, meaning no deeper insight can be obtained as to the charge and spin state of the CNT and how that relates to the observed MR.

Nickel-palladium (NiPd) has been used to investigate spin and charge transport in carbon nanotubes by Sahoo et al.[98] and Feuillet-Palma et al.[32] The choice of NiPd as a material was based on palladium showing very good reliable contact to SWCNTs[28, 29] and having the highest Stoner parameter of the non-ferromagnetic elements, meaning alloying it with a ferromagnet easily drives the palladium into a ferromagnetic state. Hence, it was hoped that a NiPd alloy might combine the reliable contacting of CNTs of Pd with a finite spin polarisation for conducting spin-transport experiments. As Man et al.[99] report conductance values of close to 2 G_0 with a NiPd alloy, the good contact appears to be true and the electrodes are ferromagnetic, so NiPd does indeed seem to be a good choice of material for spin-transport in CNTs. However these alloys

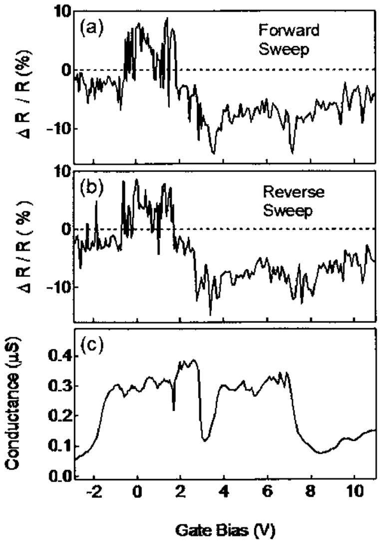

Figure 2.35: MR of a Ni contacted CNT as a function of gate voltage for the forward (a) and back (b) sweep directions and the two terminal conductance of the device (C). Measurements were taken at 4.2 K with a 100 μV AC excitation. Taken from Nagabhirava[97]

also have an easy axis that is in-plane but perpendicular to their long axis when patterned into strips to make contact to tubes, meaning the domains tend to order antiferromagnetically with moments aligned to the short axis at zero field as shown by the magnetic force microscopy image in Figure 2.36, which shows the y-axis components of the magnetic moments of the domains of two NiPd strips as colourscale values. This short axis magnetisation not only makes it difficult to design pads with specific magnetisations at the point the CNT contacts during magnetic reversal but also greatly increases the stray field of the electrodes at the nanotube, with that stray field being parallel to the tube axis and forces the applied field used to switch the pads to also be parallel to the tube axis. As discussed previously a parallel magnetic field couples to the orbital motion of the tube to modify the orbital energy levels, with an orbital energy splitting larger than the Zeeman splitting of spin states due to a perpendicular applied field, so in many cases this is not the preferred orientation for the magnetic electrodes.

SWCNT QDs contacted by Sahoo et al.[31] show clear stable coulomb resonances from which the coupling and intrinsic energy scales of the dot can be extracted.

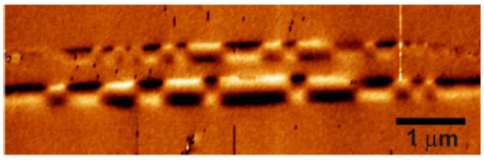

Figure 2.36: Magnetic force microscopy (MFM) image of two NiPd electrodes of differing widths. The colourscale represents magnetisation perpendicular to the long axis of the electrodes, alternating bright/dark, dark/bright sections are have there magnetic moments in opposite directions. Taken from Feuillet-Palma et al.[32]

The dependence of the MR on the gate electrode also correlates well with the position of the coulomb resonances. Applying the scattering model developed in Cottet et al.[91, 92] and using the parameters extracted from the coulomb blockade stability diagram, including asymmetric barriers, and a finite SDIPS as a free fitting parameter to the MR oscillations, results in a good fit to the experimental data as shown in Figure 2.37. Note from the consistent symmetry of the MR for the two coulomb resonances shown, that the model includes a four-fold degenerate ground state and the spin of the electrons added to the dot at each of the resonances is of the same sign. Evidence for the MR being produced by spin-transport through the CNT rather than a magneto-coulomb effect includes the asymmetry of the MR about each coulomb peak caused by SDIPS, the lack of low field hysteretic MR when one of the ferromagnetic electrodes is replaced with a NM and the large MR signal, with the MC MR calculated to be $\sim 0.4\%$ using the dot parameters. The magnitude of the SDIPS used to fit the data ($h^{\mathrm{P}}_{\mathrm{SDIPS}} = 0.05\ U_{\mathrm{C}}$) corresponds to a field of about 2 T, which is too large to attribute to stray field effects and corresponds well to the value calculated using non-interacting theory of ~ 1.3 T.

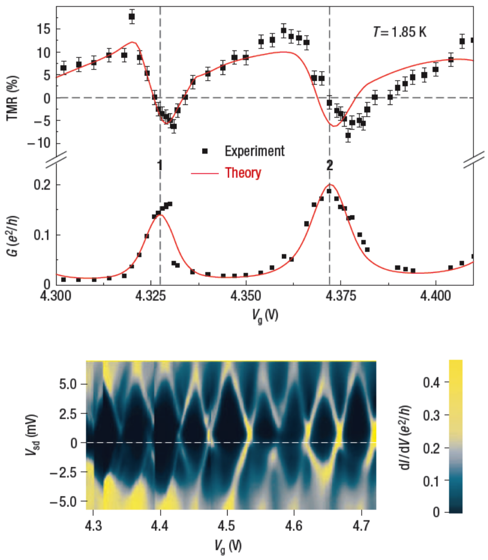

Figure 2.37: MR as a function of gate voltage and corresponding conductance for a NiPd contact SWCNT QD at 1.85 K, experimental results shown as black points and theoretical predictions from the SDIPS model of Cottet et al.[91] using parameters extracted for the QD, shown in red. The MR of both peaks has the same symmetry to the spin state of each resonance is the same and the device must be in a four-fold degenerate state. Also shown is the stability diagram for the QD, which features clear, regularly spaced resonances. Taken from Sahoo et al.[31]

During the course of this work results have also been published on permalloy (Py) contacted CNT QDs, with that of Aurich et al.[100] showing a +3% MR with a well defined anti-parallel alignment of the electrodes as demonstrated by the AMR of the pads as shown in Figure 2.38. The transport through the dot shows well defined if irregularly spaced coulomb resonances with a high conductance ($\sim 0.6\ G_0$) showing good symmetric coupling to the CNT. The MR through the device is stated to be strongly dependent on V_g although these results are not presented and given the irregularities of the coulomb resonances would be difficult to interpret in terms of the spin state of the QD.

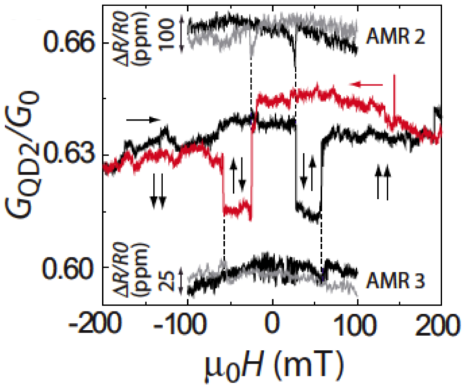

Figure 2.38: MR shown in red and black, of a Py contacted CNT QD at a fixed gate voltage corresponding to the maximum of a coulomb resonance at 230 mK. The traces above and below the MR through the device are the AMR of the Py electrodes, showing sharp switching with coercive fields that match the switching fields of the device MR, showing the device has a well defined anti-parallel state. Taken from Aurich et al.[100]

Recently Morgan et al.[101] have also published work on transport in Py contacted QDs where values of MR from 0%-4.5% were obtained depending on gate voltage. Irregular and noisy oscillations with gate voltage are interpreted as the device operating with multi-electron tunnelling but the maximum conductance at low V_{SD} of 0.0065 G_0 seems to show that the CNT is poorly contacted. The coercive fields of the magnetic electrodes are not known and there does not appear to be a stable anti-parallel state.

In summary there is evidence that a few ferromagnetically contacted CNTs have shown spin transport. Most show evidence that their MR is due to other effects such as MC that dominate, meaning there is still much to do in the field of spin transport in CNTs.

Chapter 3

Methods

3.1 Carbon Nanotube Growth

Carbon nanotubes are grown by chemical vapour deposition (CVD) by our collaborators at Basel University. Before growth 1 cm × 1 cm pieces of highly boron doped silicon that have a 400 nm thermally growth oxide on their surface and a resistivity of 10 $\mu\Omega$cm are cleaned. The oxide electrically insulates the devices patterned on the surface of the chips from the p-doped silicon underneath, allowing the silicon to be used as a backgate.
After cleaning, the chips have a iron-ruthenium (FeRu) nanoparticle solution spin coated onto them. They are then heated in a CVD system to 950°C in an argon atmosphere, at which point the argon is replaced with a methane / hydrogen mix for growth, after which the samples are cooled in an argon / hydrogen mix. In this process the methane provides the carbon feedstock for growth, the hydrogen reacts with any excess carbon, keeping the growth clean and the argon provides an inert atmosphere. This growth process produces mainly individual single wall CNTs with typical lengths of 2-10 μm[102].

3.2 Lithographic Techniques

Lithography is used to define a coordinate system to locate CNTs and then define metallic electrodes to make contact to those CNTs. In this work electron beam lithography (EBL) has been used for the creation of each layer of the devices due to its advantages in feature size and overlay alignment in comparison to optical techniques. EBL uses an electron beam to break bonds in molecules of resist that have been spin-coated onto substrates, these exposed areas are then more easily removed when placed in a development solution due to their shorter chain lengths, allowing the resist to be patterned into designs. Depositing materials onto these patterned substrates produces layers both on top of the unexposed resist and on the substrate in the exposed areas, removing the remaining resist by dissolving the resist in solution (lift-off) then leaves the substrates with material only on the areas exposed by the electron beam, as shown in figure 3.1.

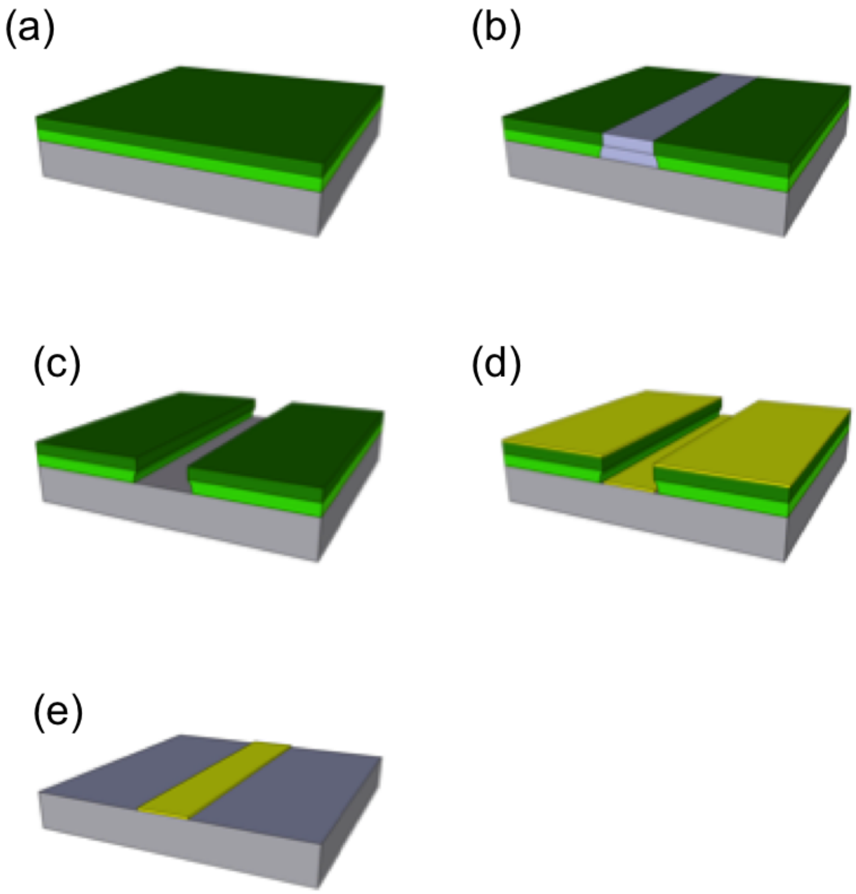

Figure 3.1: Patterning metal electrodes onto a substrate using EBL. (a) A resist is spin-coated onto a substrate comprising of two layers, the lower layer of which is composed of a polymer chain of lower molecular weight than the top layer. (b) The resist is exposed using an electron beam scanned across the substrate in a defined pattern that breaks down the resist. (c) The resist is developed, removing areas that have been exposed to the electron beam. (d) Metal is deposited onto the resist and exposed substrate. (e) Remaining resist is dissolved, leaving deposited metal on the substrate only in areas that had previously been exposed by the electron beam.

In this work a double layer resist is used made up of a 3% by volume 495K molecular weight polymethyl methacrylate (PMMA) solution in anisole under-layer, which is spin-coated onto chips with a spin programme of 2k rpm for 20 seconds, followed by 3k rpm for 40 seconds, then baked for 40 minutes at 170°C. A 2% by volume 950K molecular weight PMMA solution in Anisole top layer is then spin coated at 3k rpm for 20 seconds followed by 5k rpm for 40 seconds, then a final bake of 40 minutes at 170°C. After exposure to an electron beam at 30 kV samples are developed in a 1:3 solution of methyl isobutyl ketone (MIBK) to Isopropanol (IPA).

The lower molecular weight PMMA under-layer is more easily removed by the developer solution after exposure to the electron beam, producing an undercut to the resist profile. This allows the un-exposed resist and material deposited onto it to be removed more easily in lift off as it ensures a discontinuity to the material film between resist and substrate. This is particularly important when depositing material using sputtering, rather than thermal or electron evaporation, as the material is deposited in a diffusive process with a mean-free path on the order of a few cm, meaning the angle of incidence between the deposited particles and the substrate is not 90°, causing material to be deposited on the side walls of the resist film if the walls do not have a sufficient undercut.

3.3 Scanning Electron Microscopy

A LEO 1350 field emission gun scanning electron microscope (SEM) is used to locate CNTs relative to a set of alignment marks patterned on the substrate by EBL. In the scanning electron microscope electrons are pulled from an electron source, generally a sharpened tungsten tip, by a large accelerating voltage, of the order of keV. This electron beam is then shaped and confined by a set of magnetic coil lenses and an aperture as it travels down the SEM column. To produce an image the beam is rastered across the sample by an electrostatic gate whilst a detector collects secondary electrons produced in the sample by the primary electrons of the beam interacting with the sample.

The diameter of carbon nanotubes imaged in the SEM is comparable to the resolution of the instrument, yet they appear to be visible with an apparent diameter much larger than that expected. This is due to dynamic voltage contrast between the carbon nanotube and the insulating substrate[103], as the electron beam scans across a nanotube on an insulating substrate, the nanotube appears to glow brightly with respect to the substrate. This is due to surface charging caused by the electron beam meaning the insulating substrate acquires a negative charge, whereas the nanotube, with its relatively high capacitance and conductivity dissipates the charge incident upon it, meaning it gains a positive charge with respect to the substrate. This positive potential increases the number of secondary electrons released by the substrate around the tube as it pulls them out of the substrate. This effect, and also its converse, where a tube becomes negatively charged due to being in contact with a metal electrode, making the tube appear darker than the surrounding substrate can be seen in Figure 3.2.

A low accelerating voltage (0.8-1.1 keV) is used when searching for tubes on the substrate, this makes the penetration depth of the electron beam smaller, meaning the image acquired is more surface sensitive, maximising the ability to resolve CNTs. This allows faster scans to be performed at lower magnifications, minimising the exposure of the CNTs to the electron beam. The exposure of the CNTs to the electron beam is also reduced by taking care to image the CNTs as little as possible, as the electron beam may damage the CNTs and produces amorphous carbon buildup which forms over the tubes making electrical contact to the tube poor.

After images of tubes in relation to alignment marks on the substrate have been obtained, they are then modified to correct any errors in the x and y scaling of the image and also any slew in the image. These errors are caused by small errors in the calibration of the x and y axis deflection coils and inhomogeneous charging in the substrate. This is done by measuring and then correcting the pitch and angle of the alignment marks contained in the image and ensures the tube can be contacted reliably.

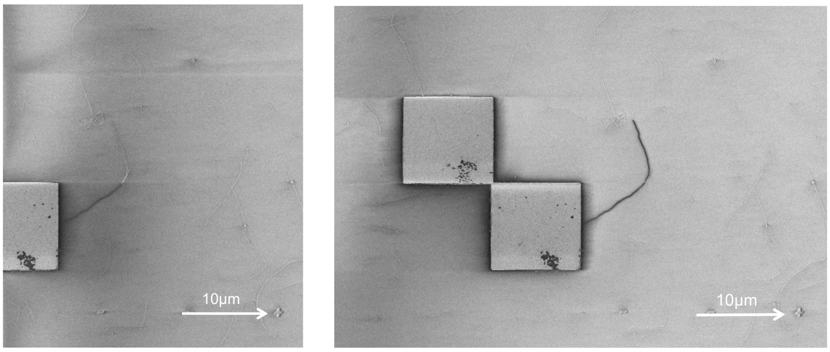

(a) (b)

Figure 3.2: Appearance of CNTs in a SEM relative to their charge state. The electron beam is rastered across the sample to obtain the image from left to right, from the top of the image to the bottom. In (a) the CNT is seen in contact with a metal electrode. In the area above the visible electrode the tube is conducting electrons away from the position of the electron beam, becoming positively charge with respect to the substrate and glowing brightly. While in areas of the tube at the same level as the electrode the electron beam has crossed the electrode before scanning the tube, negatively charging the electrode and subsequently the CNT that is in electrical contact to it, making the tube negatively charged with respect to the substrate and appear dark. (b) Shows that when the scan area is enlarged to include the entire electrode, areas of the CNT that glowed in (a) now appear dark due to the negative charge of the CNT.

3.4 Sputter Deposition

Sputtering is a technique used to deposit thin films of material onto samples by bombarding target materials with ions. The ions have enough momentum that atoms of the target material are released from the surface and diffuse across the chamber onto the sample placed opposite. In this work 2 separate sputter systems were used to deposit metal layers, with both systems using DC magnetron sputtering and employing argon (Ar) as a working gas to bombard the target. In DC magnetron sputtering the Ar is ionised by a large voltage applied between the target and its outer shield. The positively charged Ar ions are then accelerated towards the target that is held at a large negative bias. Additionally the magnetic field of the magnetron guns confines the Ar plasma, allowing a lower working pressure of argon compared to a sputter gun with no magnetic confinement. This process is shown in Figure 3.3.

The sputter system used for deposition of metallic pads onto CNTs is shown schematically in Figure 3.4. By first pumping out the main chamber using a roughing pump to ~0.5 mTorr then opening the main chamber to a cryopump, a vacuum of 10^{-8} Torr is achieved after 12 hours pumping time, as measured by a mass spectrometer installed in the main chamber. This vacuum is then further improved by flowing liquid nitrogen (N_2) through a Meisner trap positioned

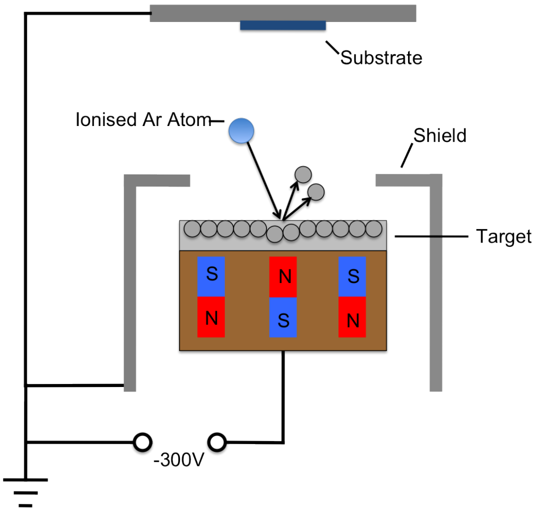

Figure 3.3: Schematic representation of DC magnetron sputtering.

around the sample for 2 hours prior to growth, the trap consists of a length of copper tubing through which the liquid N_2 flows, which has the effect of freezing water vapour left in the chamber. Using this technique a base pressure of 10^{-9} Torr with a partial pressure of water in the system of 10^{-10} Torr is possible. This low base pressure is advantageous as metals deposited are sensitive to impurities present in the chamber during growth. Samples are loaded into the system by mounting them onto the faces of a hexagonal chuck, which is then placed into a load-lock and pumped using a combination of a turbo and a roughing pump before the samples are transferred to the main chamber, allowing multiple batches of samples to be grown without breaking the vacuum of the main chamber.

Inside the sputter system 2 magnetrons designed for use with non-magnetic materials and 2 magnetrons for use with magnetic materials face the hexagonal sample chuck as shown in Figure 3.4. The guns face the sample chuck at an angle of 16° to the vertical and are separated from one another using a shield to prevent cross-contamination of the target materials. The sample chuck is also separated from the guns by a shielding plate which has an aperture over the chuck, only allowing material to be deposited onto the face of the chuck directly under the shield.

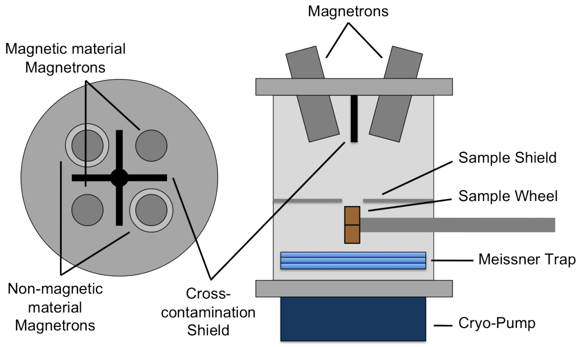

Figure 3.4: Internal layout of Mjölnir, the primary sputter system used in this work.

The other sputterer used was a commercially available Leskers PVD 75 sputter system, which was employed to deposit titanium / gold (Ti/Au) layers patterned into alignment marks or sets of bond pads connected to the inner pads that contact the CNT. It was used for these layers due to its advantages of having a short time to pump down to a reasonable vacuum (1 hour to $2{\times}10^{-7}$ Torr and having an argon ion plasma cleaning gun. This Ar ion gun allowed the inner contacts to be gently milled before deposition of the outer bond pads, ensuring no residue is trapped between the two metallic layers to make good contact between the layers. Due to the small contact area between the inner pads and the outer bond pads ($\sim$0.1 μm^2), any resist residue stuck to the metallic inner pads can produce a tunnel barrier that may not be noticeable during room-temperature measurements, but produce an open-circuit at low-temperatures.

3.5 Magneto-Optic Kerr Effect

The Magneto-Optic Kerr Effect (MOKE) is employed to measure the relative magnetisation of ferromagnetic pads at room temperature during magnetic reversal. It does this by measuring the rotation and ellipticity of the plane of polarisation of a beam of linearly polarised light when it is reflected off a sample by using two polarisers on the incident and reflected light beams[104, 105]. In the case of longitudinal MOKE the incident polariser sets the incident light to an angle of 90° to the plane of incidence this is referred to as s-polarised light. The second polariser, often referred to as the analyser in a MOKE setup is set at just under or over 90° to the first polariser, meaning the photo-diode detector beyond the analyser measures the amplitude of the light at 90° to the incident beam. The amplitude of this detected light is proportional to the magnetisation of the sample.

The rotation of polarisation of the light upon reflection from a ferromagnetic surface can be explained if we consider the s polarised light incident onto the sample as a superposition of left and right circularly polarised beams, these two beams will drive electrons in the sample into motion in the direction of their rotations. If no magnetic field is present in the sample the radii of the two electron orbitals will be equal and the light will be reflected from the sample with the same polarisation as the incident light, for magnetic materials the B field will produce a Lorentz force on these orbiting electrons making the radii for left and right circularly polarised light different, thus the two polarisations of light propagate through the sample at different velocities. On reflection from the sample the two

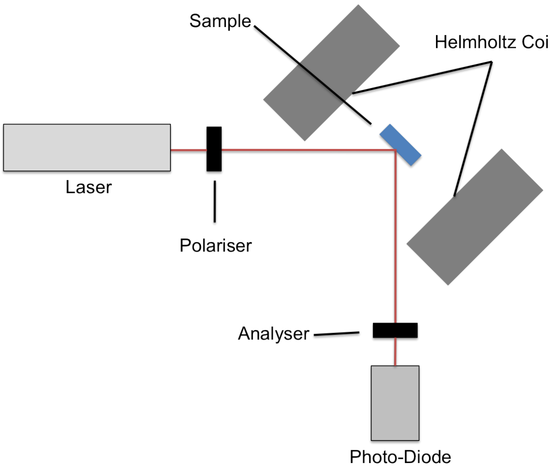

Figure 3.5: Experimental setup for longitudinal MOKE.

polarisations recombine, forming elliptically polarised light with a Kerr rotation proportional to the magnetisation of the sample.

When measuring the magnetisation reversal of pads designed to be used as electrodes in CNT transport experiments the pads must be patterned as repeated arrays in a 1 mm^2 area, as the laser spot incident on the sample is approximately 2 mm in diameter and single pads would not contain enough material to observe the Kerr rotation.

3.6 Low Temperature Techniques

To measure properties of devices such as coulomb blockade the devices must be cooled to a point where the thermal energy of the sample is less than the energy scales of the effects being investigated, for example the energy level spacing of the carbon nanotube, which is on the order of 1 meV corresponds to a temperature of 12 K.

An Oxford Instruments helium-flow cryostat, is used to achieve these temperatures by releasing liquid helium into an evacuated sample space via a needle valve connected to a helium bath that surrounds the sample space. When the liquid helium at 4.2 K enters the evacuated sample space it boils, lowering the temperature of the sample space. By evacuating the sample space the vapour pressure of the helium can be lowered reducing the temperature it boils at, and so the temperature the sample space can be cooled to. This allows a device loaded into the sample space to be cooled to 1.4 K, or alternatively held at any temperature between 1.4 K and 300 K by changing the amount of liquid flowing into the sample space, heating the base of the chamber with a resistive element and by varying the speed at which the chamber is being evacuated. Samples are loaded into the cryostat by placing them into a brass sample head, with electrical contact made to the device using sprung pins. The sample head is mounted onto the end of the sample stick, around which the electrical measurement lines are wound, ensuring the lines are thermally anchored to the stick to prevent heat transfer to the sample from the room temperature lines connected to the top of the stick. Baffles mounted onto the stick reduce heat transfer from the top plate through the gas in the chamber. A superconducting solenoid mounted in the helium bath around the sample position allows a magnetic field of up to 9 T to be applied to the sample for magneto-transport measurements.

For lower temperatures a Cambridge Magnetic Refrigeration (CMR) adiabatic demagnetisation refrigerator[106] allows samples to be cooled to a base temperature of 50 mK, this apparatus takes considerably longer than a helium-flow cryostat to load a sample ready to measure, and for this reason tends to be used for samples that take longer to measure. CNT samples tend to be measured in this cryostat due to the longer time available for measurement without having to unload and reload samples, this is advantageous as thermally cycling samples may change local charge buildup in the substrate and contact to the CNT, changing the device, meaning results between cryostat runs may not be comparable.

To reach 50 mK the CMR fridge uses three stages of cooling, the first stage of which is to load the experimental insert, shown in Figure 3.6, into a liquid helium bath. This is done with a small amount of helium in the experimental insert vacuum can to transfer heat from the apparatus inside the can to the helium bath. The vacuum can is then pumped out to high vacuum allowing the next stage of cooling to start, which is to use a 1 K pot, consisting of a chamber connected to the helium bath via a needle valve, in thermal contact with the 1 K plate and evacuated by a pumping line. Lowering the vapour pressure of the helium in the 1K pot cools the chamber from 4.2 K to <2 K and in turn the 1

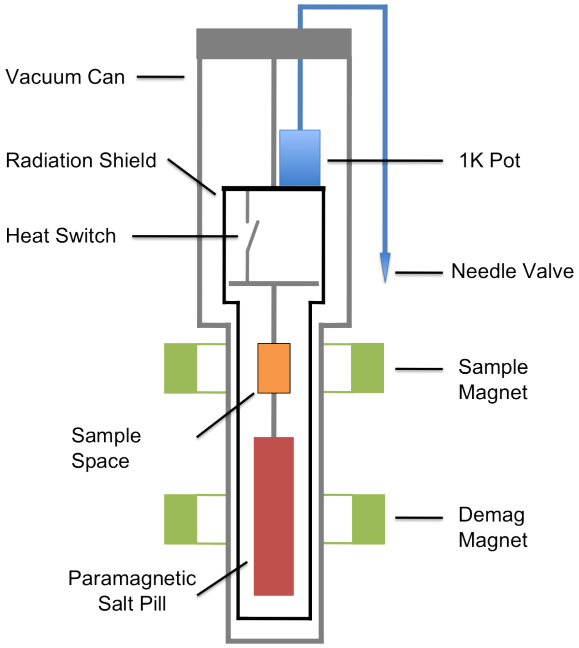

Figure 3.6: Schematic representation of the CMR fridge experimental insert. When in operation the whole system is submerged in a liquid helium bath.

K plate. The third stage of cooling is adiabatic demagnetisation, used to cool the low temperature stage (LTS). The LTS is thermally connected to the 1 K plate by a heat switch that consists of a set of gold-plated copper fingers that can be brought in and out of contact with a cup mounted onto the LTS. When the heat switch is open the thermal contact between the LTS and the rest of the experimental insert is very low as it is suspended from a set of thin kevlar cords. When the paramagnetic salt pill attached to the bottom of the LTS is magnetised and the heat switch is closed, the magnetic moments of the paramagnetic salt are aligned, decreasing the entropy of the LTS and in turn heating it. When the LTS has subsequently cooled down to the temperature of the 1 K plate the heat switch is opened and the temperature of the LTS can be further reduced by reducing the field applied to the paramagnetic salt. The moments of the paramagnetic salt then randomise, increasing their entropy and cooling the LTS to a base temperature of 50 mK. The base temperature is reached when the field on the paramagnetic salt is zero and the moments are fully randomised. Alternatively the system can be held at a given temperature between the temperature of the 1 K plate and 50 mK by reducing the field on the salt pill until the LTS reaches the temperature set, then slowing the rate at which the field is being reduced to a rate that holds the temperature stable. As the temperature drop of the LTS is roughly proportional to the amount the field has been reduced from its maximum value, higher temperatures can be held for longer periods of time than lower temperatures, as a higher field is still applied to the salt pill once the holding temperature has been reached. A superconducting solenoid mounted in the helium bath around the sample position allows a magnetic field of up to 6T to be applied to the sample for magneto-transport measurements, this field is independent of the field applied to the salt pill.

3.7 Low Temperature Measurements

To measure the conductivity of CNT devices at low temperatures using DC voltages a National Instruments Digital Acquisition (DAQ) card is used, as this apparatus is able to supply ±10 V with a resolution of 16 bits, or 0.3 mV, the output voltage it supplies is often stepped down by a voltage divider by $2\times \rightarrow 1000\times$ before it is connected to the device to allow more sensitive measurements to be performed. A Stanford Research Systems SR570 current to voltage pre-amplifier is then used to convert the current flow through the device into a voltage that is read back by one of the sense channels of the DAQ card. The SR570 has a sensitivity of $10^{-3} - 10^{-12}$ A/V and can be powered by internal batteries during measurements, ensuring the only earth of the measurement apparatus is supplied by the DAQ card. For AC measurements a Stanford Research Systems SR830 Lock-in Amplifier (LIA) is used to supply an AC voltage, which is then stepped down by a transformer or voltage divider. The AC current flow through the device is then converted to a voltage by the SR570, which is then measured by the LIA, with R and θ measured as voltage outputs of the LIA by two sense lines of the DAQ.

To measure differential conductance at a constant DC bias the AC voltage supplied by the LIA must be combined with the DC output of the DAQ. This must be done without introducing earth loops between the apparatus and is performed by either combing the two signals using an AD524 Op-Amp with voltage followers on each input or by adding the AC voltage to the DC by using a transformer.

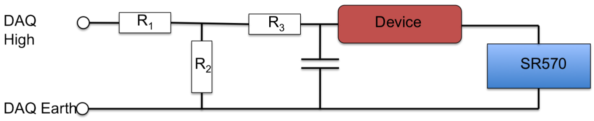

Figure 3.7: Circuit for voltage biased DC measurements.

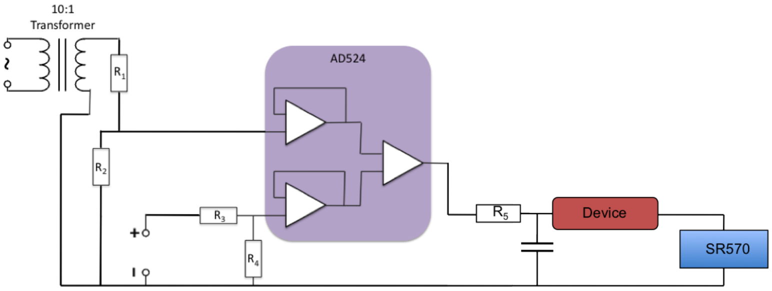

Figure 3.8: Circuit for voltage biased AC measurements, with additional DC bias offset. Alternative setups include running the DC supply through one side of a transformer whilst the other side is AC biased, removing the need for the comparator.

3.8 OOMMF

The Object Orientated MicroMagnetic Framework (OOMMF)[107] is a program written to model the magnetisation of materials by solving the Landau-Lifshitz-Gilbert (LLG) equation[108, 109]:

$$\frac{\delta m}{\delta t} = -\gamma m \times H_{eff} + \alpha_G m \times \frac{\delta m}{\delta t}$$

This describes the damped precession of a magnetic moment about an effective field (H_{eff}), where $\gamma = \mu_0 ge/2m_e$ is the gyromagnetic ratio and α_G is the Gilbert damping parameter. It does this by separating the structure of the magnetic material being simulated into a array of elements of a chosen size that should be of the order of the exchange length in the material for accurate calculation. Each element then has is own magnetisation and effective field due to the elements surrounding it made up of the exchange, Zeeman, magnetostatic and crystalline anisotropy fields. OOMMF then solves the LLG equation for each element and changes the magnetisation of the elements in response to the precession for a small change in time, this process then continues to iterate until the torque ($m \times H_{eff}$) decreases below set tolerance.

Chapter 4

Permalloy Nucleation Pad Electrodes

4.1 Introduction

In this chapter we present results obtained from permalloy (Py) contacted nanotubes by first discussing the pad design and magnetic properties, then presenting results on the formation of a quantum dot at low temperatures. Finally we present magneto-transport measurements performed on devices, relating these results to the pad magnetics. The magnetoresistance of the devices are shown to vary with applied source-drain bias and the interpretation of results at high and low source-drain bias are discussed.

4.2 Pad Design

To investigate spin-dependent transport in carbon nanotube devices it is necessary to align the ferromagnetic contact pads contacted to CNT in parallel and anti-parallel configurations using an applied field. In spin-valve devices different materials can be used for each of the magnetic elements to create hard and soft pads with differing coercive fields that are dependent on their constituent materials. When using the same material for each pad in a lateral geometry shape anisotropy is used to create a hard and soft pad, in which a shape is chosen for each pad that increases or decreases the coercive field to minimise the demagnetisation energy. The shape of the magnetic pads used in this chapter can be seen in Figure 4.1, with the oval soft pad on the left and the pointed hard pad on the right. These pad designs were chosen as they had already been characterised and used in domain wall nucleation work carried out at the University of Leeds, where there differing coercivities had been established[110].

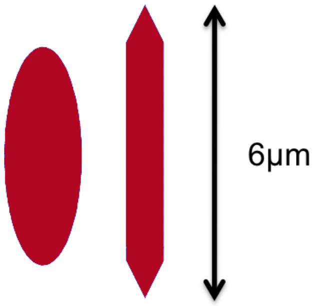

Figure 4.1: Design of Py nucleation pads with shape anisotropy to create differing coercive fields for the left, soft pad and the right, hard pad.

MOKE measurements performed on arrays of the magnetic pads at room temperature, shown in Figure 4.2, have a two stage reversal as the soft pad and hard pad switch their magnetisation. The switching of the soft pad occurs over a larger range of field than the hard pad, showing it remains misaligned with the axis of the applied field for longer. The magnetisation is also seen to not quite reach a constant value before the hard pad reverses, meaning that the soft pad has not fully completed its rotation before rotation of the hard pads magnetisation begins to occur. However the change in magnetisation with field is small at this point, showing most of the magnetisation of the pad is aligned with the field and when these pads are used to contact CNTs at low temperature their coercive fields should be increased, increasing the field range over which an anti-parallel alignment is possible.

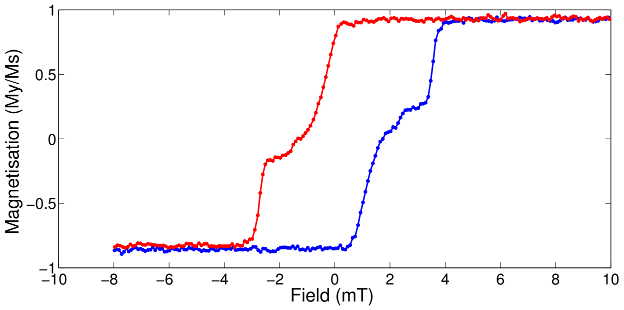

Figure 4.2: MOKE measurements of the magnetisation parallel to the long axis of the pads (M_y) carried out on large arrays pads at room temperature. A two step switching process is observed and attributed to the switching of the soft and hard pad designs. Note that there is no point in between the two magnetic reversals where the magnetisation is held constant - there is no stable anti-parallel alignment of the entire pad at room temperature. The blue line shows the field sweeping in a positive direction and the red line the field sweeping in the negative direction.

To measure the switching of the pads patterned onto CNTs at low temperature the resistance of the pads along their easy axis can be measured during magnetic reversal. A change in resistance, known as the anisotropic magnetoresistance (AMR), due to the change in angle between the pad magnetisation and the direction of current is observed, with a minimum when the magnetisation is at 90° to the current and an angular dependence of $\cos^2\theta$ where θ is the angle between the magnetisation and the current in bulk polycrystalline samples. This dependence is derived from the high symmetry of the resistivity tensor in bulk materials and may differ from magnetic nanostuctures due to diffusive scattering at the surface[64]. Figure 4.3 shows the AMR in both a hard and soft pad at 1.66 K, with the resistance values scaled to show the hard pad above the soft pad in the figure. The resistance of the hard pads is seen to start to decrease before the soft pad, however the minima in resistance are at roughly the same value, not showing a good separation in the switching fields of the pads as required for anti-parallel alignment of the pads. However these results were obtained from magnetic pads on the same chip, but not connected to the CNT device, so it is possible the pads contacted to the CNT performed better, or that the domain structure of the pads allowed an anti-parallel alignment as they switched, given that the CNT is small, and will possibly only contact a single magnetic domain.

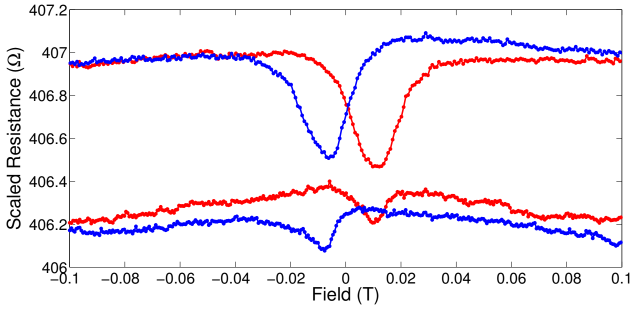

Figure 4.3: AMR measurements performed on the pads at 1.66 K. The hard pad magnetic loop is placed above that of the soft pad. The conductance minima, corresponding to the points at which the magnetisation of the pad that is perpendicular to the current direction are seen to be very similar, showing there is not good separation of the coercive fields of the pads at low temperature.

4.3 Non-Magnetic Transport

Figure 4.4 shows a diagram of Device 1, a 400 nm long CNT spanning between two magnetic pads described previously. Two non-magnetic leads make contact to each magnetic pad, however contact 1 was found to be broken upon testing the device, leaving only one contact onto the soft magnetic pad.

Transport measurements were taken using the electrical measurement setup described previously with the device in the adiabatic demagnetisation refrigerator (ADR) using the 2nd stage of cooling to hold the temperature at approximately 1.8 K. At this temperature the IV characteristics of the device at a gate bias of 0 V show steps corresponding to the energy spacing of the nanotube together with a blocked central region due to the coulomb repulsion of charge on the dot as shown in Figure 4.5.

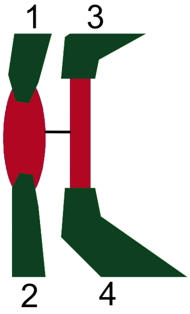

Figure 4.4: Contacts made to the magnetic pads using NM leads. The carbon nanotube spans the gap in between the two Py pads. Unfortunately contact 1 was found to be broken, leaving only 3 connections to the device.

The device also shows coulomb resonance as the V_g is swept at constant source-drain bias as seen in Figure 4.6, corresponding to energy levels being swept between the source and drain energy levels. The coulomb resonance has a spacing of 14.5 ± 0.3 mV corresponding to a back-gate capacitance of the dot of 11.1 ± 0.2 aF. There is no four point periodicity in the V_g peak spacing as one would expect for a pristine nanotube.

By varying both source-drain bias and gate voltage whilst measuring the current flow through the device the differential conductance can be plotted. This is

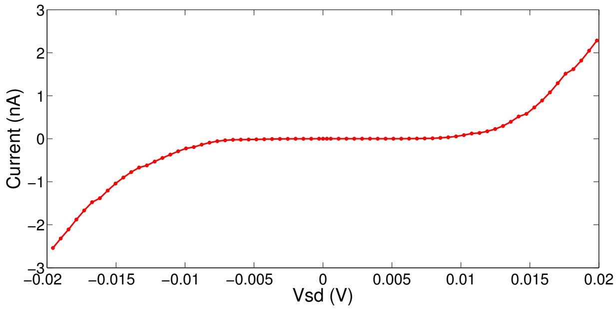

Figure 4.5: Current-voltage (IV) characteristics of the device at low temperature (1.66 K). Steps in the conductance of the device with applied V_{SD} are observed showing charge quantisation in the transport of the device.

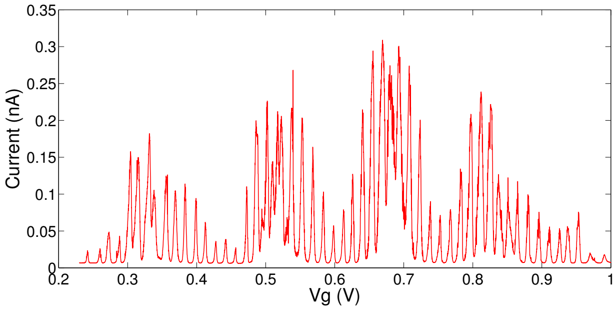

Figure 4.6: Dependance of the conductance on V_{g} at a fixed source-drain bias of $V_{\mathrm{SD}} = 2$ mV at 1.66 K. Regularly spaced coulomb resonances are observed with a 14.5 ± 0.3 mV periodicity.

shown in Figure 4.7 and also in Figure 4.8, with a decreased colour-scale range to make the low source-drain bias more visible. Both these figures show a low conductance region at low source-drain bias that does not follow the standard theory for transport in a CNT quantum dot.

To explain this low conductance region we must look at the transport between the non-magnetic leads and the magnetic pads. IV measurements through the hard pad using contacts 3 and 4 showed a non-linear tunnelling relationship upon loading the device. Before transport measurements were performed on the CNT this pad was current annealed, removing the barrier. This pad then had a linear IV and a resistance of $\sim 470\ \Omega$. The soft pad only having one working contact

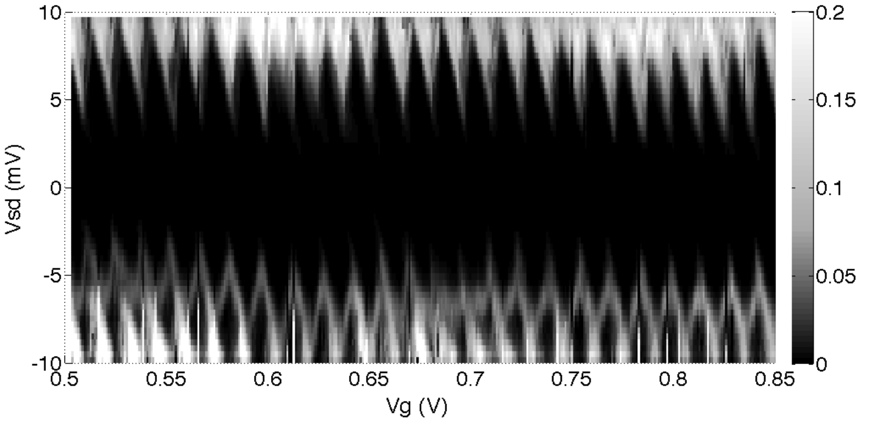

Figure 4.7: Coulomb blockade stability diagram of the device at 1.66 K, the edges of the coulomb blockade diamonds are observed, but no excited states of the QD are visible. Note the large central region where transport is blocked which is attributed to a tunnel barrier in series with the device. Colourbar in 10^{-3} G_0

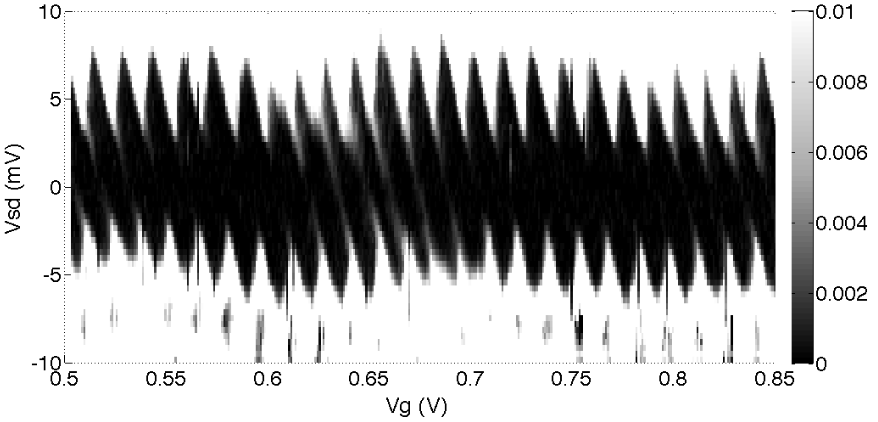

Figure 4.8: Coulomb blockade stability diagram of the device at 1.66 K, plotted with a smaller conductance range to show transport in the central region. We observe that the coulomb peaks are offset in V_{g} as well as separated by the blocked central region. Colourbar in 10^{-3} G_0

meant it could not be current annealed, leaving a tunnel barrier in series with the CNT quantum dot on the drain side of the device in the configuration it was measured in. This tunnel barrier decouples the Fermi level of the soft pad from the drain, which is held at ground by the DAC card. This can be seen in the low source-drain bias region of Figure 4.8 where the coulomb blockade resonances move to higher gate voltages at larger negative source-drain bias. When applying a negative source-drain bias the Fermi level of the source electrode is raised and the Fermi level of the soft pad is between the level of the the source and ground, causing electrons to tunnel through the barrier, as shown in Figure 4.9. Applying a larger negative potential raises the source level and in turn the soft pad level to a lesser extent, this raising of the soft pad level means the quantum dot energy must be raised to achieve the maximum conductance through the dot, which can be achieved by applying a larger positive potential to the gate.

To extract the charging energy U_{C} of the dot and the gate coupling factor α the

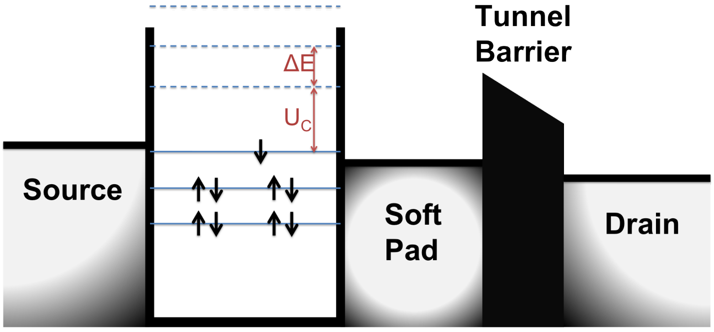

Figure 4.9: Schematic representation of the device showing a tunnel barrier between the soft pad and the non-magnetic lead that connects it to the measurement apparatus. This tunnel barrier produces an offset in chemical potential between the soft pad and drain when the device is source drain biased.

central region of low conductance is removed from the plot and the positive and negative source drain bias offset by $\Delta V_{\mathrm{g,TB}}$ the change in gate potential needed to compensate for the raised soft pad energy level to keep the CNT energy level equidistant between the source and soft pad levels. This is valid as we may assume the blocked regions of the coulomb blockade diamonds are not affected by the voltage bias on the tunnel barrier once the blocked central region has been removed as the voltage bias over the tunnel barrier, and so the Fermi level of the soft pad, should be roughly constant.

Figure 4.10 shows a section of the differential conductance plot after removing

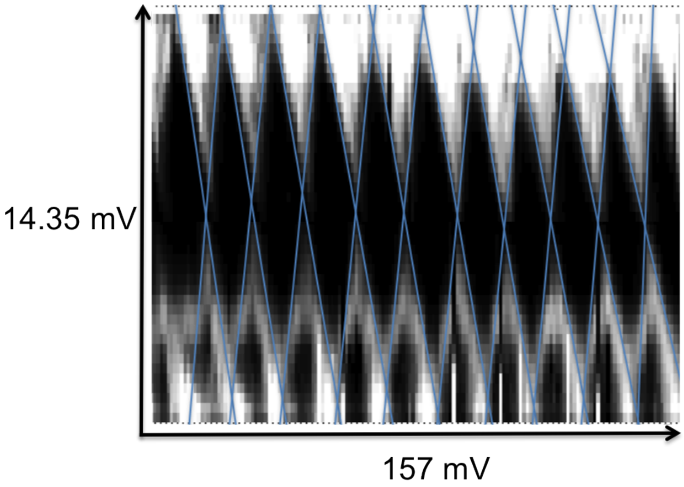

Figure 4.10: Differential conductance through the device as a function of V_g and V_{SD}. The blocked central region of the device identified in Figure 4.7 has been removed and the remaining results offset by 13.35 mV in V_g. Blue lines show the edges of the coulomb blockade diamonds allowing parameters of the QD to be extracted.

the blocked central region. The measurements of the coulomb blockade diamonds correspond to a charging energy of 6.3 ± 0.1 meV and $E_{\text{add}}/e\alpha = 14.5 \pm 0.3$ mV, giving a gate coupling factor $\alpha = 0.43 \pm 0.01$. The section removed was 5.65 mV in V_{SD} and the two remaining sections were offset by 13.35 mV the ratio of which is 0.42. This value is within the range of α, confirming that within the blocked central region almost all the applied voltage is dropped across the tunnel barrier, raising the Fermi level of the soft pad by e$\cdot V_{SD}$. The gradients of the lines indicating the edges of the coulomb blockade diamonds shown in Figure 4.10 are used to extract the capacitative coupling of the dot to the source and drain electrodes, giving $C_S = 8.9 \pm 0.2$ aF $C_D = 5.8 \pm 0.2$ aF. By combining with the capacitative coupling of the gate found previously we find the total capacitance of the dot to be $C_\Sigma = 25.8 \pm 0.8$ aF. The charging energy of the QD indicates that it is probably a single-walled carbon nanotube[58].

4.4 Magnetic Transport

An external field can be applied along the easy axis of the device in the ADR whilst measuring the transport properties of the device using DC techniques as previously described. This allows the properties of the device to be found upon magnetic reversal of the magnetic pads. The conductance of the device was measured at a constant gate voltage set at a coulomb blockade resonance, for a range of source-drain biases, these measurements were repeated between 20 and 30 times and then averaged to increase the signal to noise ratio and remove random conductance fluctuations from the measurements which can occur in CNT devices over long time periods.

Magnetoresistance measurements were seen to have two regimes at high and low bias, with high bias measurements performed at $V_{\mathrm{SD}} = 20 \rightarrow 40$ mV, when the device I-V characteristics were approximately linear and those below $V_{\mathrm{SD}} = 20$ mV in the non-linear coulomb blockade regime.

Figure 4.11 shows the high bias regime, in which the IV through the device is approximately linear. In this bias range many excited states are available for conduction through the CNT and it is effectively acting as a resistor, with no gate voltage dependence of conduction through the device for small changes in gate voltage. Although no gate voltage sweep at this bias was performed to confirm this. However if MR structure of lower source-drain bias is attributed to changes in the charge on the QD due to the electrostatic energy of the pads causing a magneto-coulomb shift in energy of the QD and that structure is not seen at higher V_{SD} it implies that changes in the charge state of the QD do not change the conduction through it at this level of bias. The change in current between the high and low conductance states during magnetic reversal increases approximately linearly with bias voltage between 20 mV and 30 mV as would be expected for giant magnetoresistance (GMR), although the change in current for 40 mV is lower than would be expected. Fitting the high and low conductance states of the MR between 20 mV and 30 mV with a linear plot gives a low resistance of 1.4 ± 0.2 MΩ, a high resistance of 1.6 ± 0.3 MΩ and a GMR of $9 \pm 2\%$. Obviously the error in the two resistance values is very large and the error ranges of the two values overlap, this is due to the lack of V_{SD} values considered

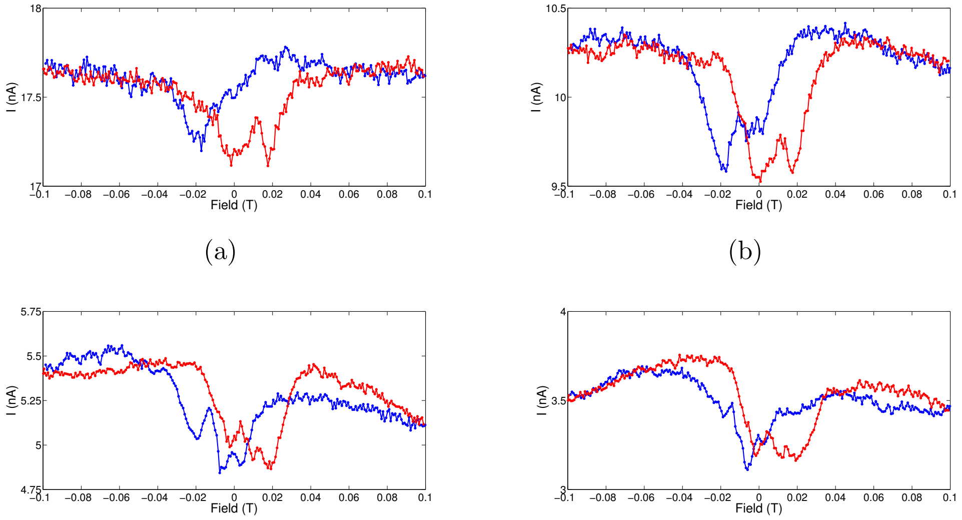

(a)

(b)

(c)

(d)

Figure 4.11: Current flow through the device at 1.66 K in the high bias regime, at fixed source-drain biases of (a) $V_{\mathrm{SD}} = 40$ mV, (b) $V_{\mathrm{SD}} = 30$ mV, (c) $V_{\mathrm{SD}} = 25$ mV and (d) $V_{\mathrm{SD}} = 20$ mV as the applied magnetic field is swept forward from negative to positive values (red lines) and back from positive to negative values (blue lines)

and because of the way the measurement was taken. As the MR was measured for each source-drain value over the period of hours the consistency between the points is a lot lower than would be expected for a single IV measurement and different amplification values were used for different V_{SD} points depending on the conductance of the device, with the amplifier offset varying depending on its amplification level. This means that although the conductance of the device is consistent for the MR measured at each source-drain bias, there may be offsets in the IV dependence when comparing the current flow though the device at different V_{SD}. These difficulties only allow us to conclude that it is possible that the increasing ΔI of the MR at larger V_{SD} could be due to GMR. Comparing the MR of the device with the AMR of the pads in Figure 4.12 it is obvious that an anti-parallel alignment of the overall magnetisations of the pads is not achieved, however the CNT may be in contact with a small area of each pad, meaning the signal seen is the misalignment of a single domain in each of the magnetic pads. The shape of the MR through the device is consistent with this as it shows a broad double dip in conduction compared to the sharper dips seen in the AMR of the device, as the conductivity of a GMR device is proportional to $\sin^2(\theta/2)$, where θ is angle between the two magnetic domains the CNT contacts. To obtain the shape of the MR observed one domain may rotate early in the magnetic reversal and then remain misaligned to the CNTs other contacted domain until the pads have almost finished their reversal, apart from the small peak in the centre of the broad dip, corresponding to a reduction in θ.

Figure 4.13 shows the lower bias regime. These results were taken after the high bias results using the same measurement setup and gate voltage. In this bias range the IV of the device is non-linear and steps in the IV due to energy levels of the quantum dot becoming available for transport are observed (Figure 4.5). Compared to the high bias range additional structure is seen in the MR, together with an offset in conduction between the positive and negative saturations that increases relative to the level of the current with decreasing V_{SD}. We also observe a larger magnetic field range over which the MR is observed. The larger range over which the MR is observed is consistent the changing energy of the magnetic pads affecting the charge state of the QD, as if we assume the MR seen at higher bias is due to the angle θ between the magnetisations and that θ does not vary

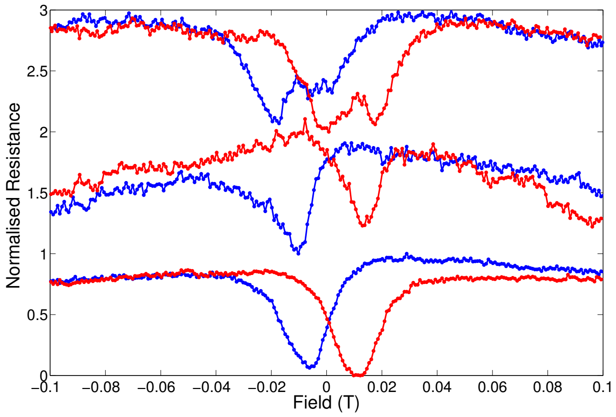

Figure 4.12: Comparing the soft pad (lower trace), hard pad (middle trace) and device MR (upper trace). Resistance for the three data sets is normalised and offset. MR seen through the device would have to be caused by a domain in the pads rotating very early in the magnetic reversal of the pads.

with V_{SD} the magnetic field dependence of the MR due to spin-scattering at the interfaces should also not change with V_{SD}. However the demagnetising energy of a domain contacted to a CNT may change before a significant rotation of its magnetisation has occurred, producing an induced charge on the dot, changing its conductance.

The change in the charge induced on the quantum dot due to the Zeeman shift of the energy of the pads (Δq) can be calculated using the capacitive coupling of source and drain electrodes[86]:

$$\Delta q = \frac{(\mathrm{C}_S + \mathrm{C}_D)}{2e} g P \mu_B B$$

With the change in Δq_{Rev} upon magnetic reversal of the electrodes being the value of most interest to this experiment, to find an estimate of the maximum possible change in conductance due to the MC effect in this system we will assume that the coercive fields of the pads are approximately the same ($H_C = 0.02$ T from AMR) and that the magnetisation of the pads M_y/M_S along the long axis of the pads changes from +1 to -1 upon reversal. These assumptions lead to $\Delta q_{\mathrm{Rev}} = 0.085$ meV or 0.0135 e. To then find the corresponding change in conduction of the device the change in conductance with gate voltage ($\mathrm{d}G/\mathrm{d}V_{\mathrm{g}}$) must be known. Unfortunately V_{g} conductance data for this device only exists for source drain

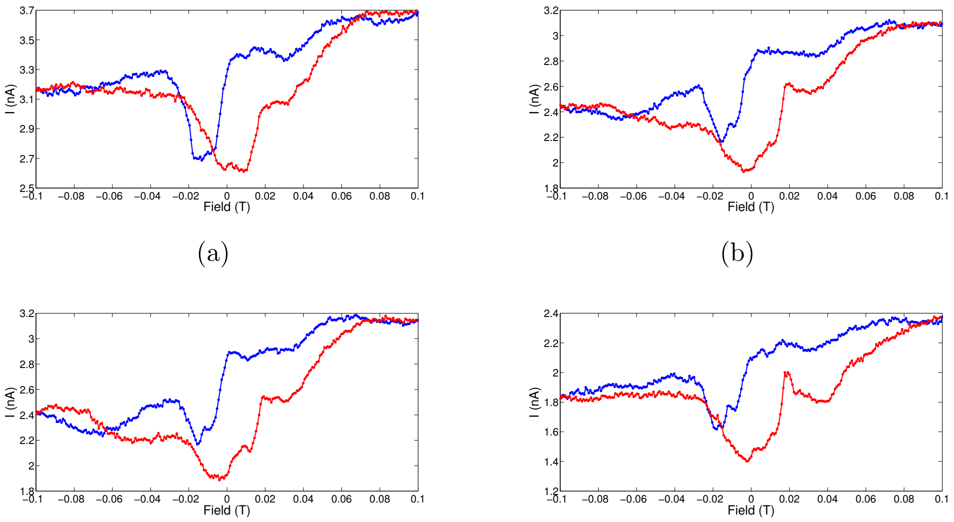

(a) (b)

(c) (d)

Figure 4.13: Current flow through the device at 1.66 K in the low bias regime, at fixed source-drain biases of (a) $V_{\mathrm{SD}} = 17.5$ mV, (b) $V_{\mathrm{SD}} = 16$ mV, (c) $V_{\mathrm{SD}} = 15$ mV and (d) $V_{\mathrm{SD}} = 14$ mV as the applied magnetic field is swept forward (red lines) and back (blue lines)

biases of up to $V_{\mathrm{SD}} = 10$ mV and the MR measurements are between 14 mV and 17.5 mV so the values must be extrapolated from the lower biases. Upon plotting $(\mathrm{d}I/\mathrm{d}q)/I$ we find the relationship linear and choose a value equal to the upper bound of the data of $\mathrm{d}I/\mathrm{d}q \sim 2$ nA/e at a current of 0.4 nA which equates to $\mathrm{d}I/\mathrm{d}q = 18.5$ nA/e at $V_{\mathrm{SD}} = 17.5$ mV, making the maximum change in current due to MC effect ~ 0.25 nA for this source-drain bias. As this, the maximum possible change due to the MC effect, is still less than the observed ΔI and does not explain the offset in saturation current, there must be an additional effect contributing to the MR. As with the increased range the MR is observed over, these features could be explained by a domain local to the nanotube that due to the demagnetising field in the electrode increasing the induced charge on the QD over what is expected from the MC effect and possibly persisting up to 0.1 T, producing a saturation offset depending on its direction of magnetisation relative to the rest of the electrode.

Between the last set of MR data presented and the following MR results the device transport properties changed, showing coulomb peaks in different positions and increased low V_{SD} conductance. This change is attributed to an annealing of the tunnel barrier between the ferromagnetic pad and drain discussed previously. Although high currents were not passed between the ferromagnetic electrode and normal metal lead as with the hard pad the substantial amount of time the device had been measured for lessened the barrier. When measured the device parameters were the same, $U_{\mathrm{C}} = 6.3$ meV and $E_{\mathrm{add}} = 14.8$ mV but the central region in which conduction was blocked was reduced to 2.82 mV from the previous value of 5.65 mV.

MR measurements at low source drain bias (V_{SD}=2-4 mV) are shown in Figure 4.14, we observe the saturation offset seen in previous measurements and also the features of the structure of the MR are similar to those previously observed and attributed to domain movement in the Py pads. As the tunnel barrier in series with the device is known to not allow current to flow until the voltage drop across it is 1.41 mV the voltage drop across the CNT at $V_{\mathrm{SD}} = 2$ mV, shown in Figure 4.14(c), is equal to V_{QD}=600 μV, at which level we may assume the IV dependence of the device is approximately linear, this allows the calculation of the MR as $MR = (G_{\mathrm{P}} - G_{\mathrm{AP}})/G_{\mathrm{AP}}$. The MR is then $\sim$ 93% when taken between the positive saturation and minimum conductance dips and $\sim$ 245% when taken between negative saturation and the minimum conductance dips.

The maximum value of $\mathrm{d}I/\mathrm{d}q$ from the coulomb peaks of the device at $V_{\mathrm{SD}} = 2$ mV is found to be 0.148 nA/e, which allows the maximum change in current due to the MC effect to be found to be $\Delta I = 0.02$ nA, which is close to half the current change between the positive saturation and minima and far smaller than the change between the negative saturation and minima. Although as we have actual conductance with field data at this bias level the induced charge on the dot needed to produce the changes in conduction observed can be better estimated to be 0.12 e for the negative saturation to the minima, an order of magnitude larger than the calculated maximum possible change in charge due to the switching of the pads.

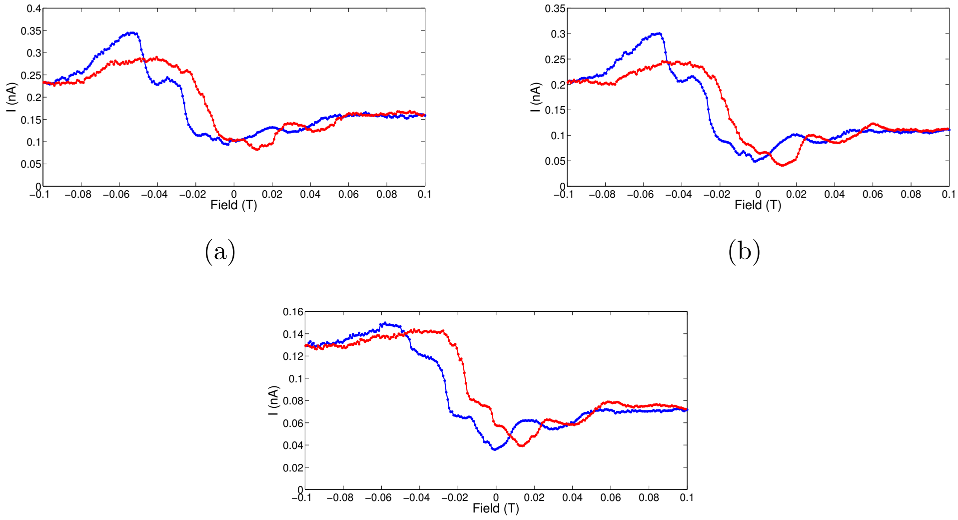

(a)

(b)

(c)

Figure 4.14: Current flow through the device at 1.66 K in the low bias regime, after partial annealing of the tunnel barrier between the soft pad and drain. Measurements taken at fixed source-drain biases of (a) $V_{\mathrm{SD}} = 4$ mV, (b) $V_{\mathrm{SD}} = 3$ mV and (c) $V_{\mathrm{SD}} = 2$ mV as the applied magnetic field is swept forward (red lines) and back (blue lines)

Results from the device presented in this chapter have shown that stable contact can be made to carbon nanotubes with sputtered permalloy, forming quantum dots with regularly spaced coulomb resonances, although the conductance of the device was quite low (0.054 G_0 at 600 μV). The magnetic properties of the Py pads however were lacking, with no well-defined anti-parallel state and possibly domain dynamics causing large changes in conductance in the carbon nanotube contacted. In the following chapter this is solved by using a pad design that is single domain in the tube contact area and has a reasonable separation of coercive fields between the hard and the soft pad.

When magnetoresistance has been ascribed to changes in electrostatic potential of the Py pads, the magnitude of the energy change needed to produce a MR of the size observed is an order of magnitude larger than that predicted as the maximum possible energy change due to Zeeman shift in the pads , showing that other factors are affecting the transport through the tube. One possibility for the large change in conduction could be a changing tunnel barrier height between the magnetic electrodes and the CNT, however, no sign of the modification of the barrier heights is seen in the gate voltage dependence of the conduction and there is no intrinsic difference between a change in electrostatic energy of a barrier due to charge build up in the magnetic pads or the substrate so if this was the case we would expect to observe it. So if we cannot assign a change in barrier height to a changing electric field maybe it is due to the changing magnetic field. As we are in the coulomb blockade regime individual energy levels may be assigned spin states from calculation of the shell-filling, though there is no preferred orientation of the spin outside of its interaction with an applied field i.e. we expect orbitals to be filled in majority / minority order rather than in some pre-defined sequence. However domain misalignment that differs between the two saturations may change the stray field on the dot in the two states, producing a magnetisation dependence of the QD energy levels.

In summary the MR observed in the high bias regime is ascribed to GMR in that it is due to spin dependent scattering at the CNT / electrode interfaces. The magnitude of this high bias MR is $9 \pm 2\%$, which is of a similar order to most published results, with only Jensen et al.[96] observing significantly higher values at 100%. At lower bias when coulomb blockade controls transport through the dot we observe MR over a larger field range with offsets in saturation conductance which we believe is due to changes in the charge state of the dot, as these changes in charge are larger than the calculated possible change due to the MC effect there must be another process involved, potentially caused by the domain state of the magnetic pads.

Chapter 5

Permalloy Nanowire Electrodes

5.1 Introduction

Following the results presented in the previous chapter magnetic pads were designed with a simpler magnetic reversal, allowing measurements to be taken at better defined magnetic states, with anti-parallel alignment of the pads over a known field range. This chapter will present magnetic measurements and simulation of the pad design followed by results obtained from Devices 2 and 3, consisting of carbon nanotubes spanning between the two magnetic pads which act as quantum dots at low temperature.

5.2 Pad Design

Following results from Py nucleation pad contacted CNTs presented in the previous chapter it was concluded that pads were needed that had differing coercive fields and areas that remained in single domain states during magnetic reversal to contact the carbon nanotube. Rectangular pads with high aspect ratios, as used in various works, were tested, with 200 nm × 5 μm and 500 nm × 2 μm chosen as 200 nm represented the smallest feature size that could be patterned with enough consistency by EBL using equipment available. However these pads magnetic properties were still not optimal, with the hard pad coercive field being 0.01 T and the soft pad rotating between 0 T and 0.005 T from MOKE measurements. When used to contact carbon nanotubes these pads had a low success rate compared to larger nucleation pads and devices that showed QD behaviour at low temperatures did not show consistent magnetic properties.

The next pad design was then based on work by Kirk[111, 112] which shows that the coercive field of a permalloy electrode can be significantly increased by sharpening the ends of the pads to exclude closure domains from the tips of the electrodes. They show a stable single domain state in 200 nm wide Py elements that have two sharpened ends, however this width is equal to that of the thinnest electrode of the rectangular pads used previously, so this was increased to 300 nm to try to improve contacting to CNTs. This was considered a reasonable width to choose as Preusche et al.[113] show lengths of Py that remain in a single domain state at zero field at widths of 500 nm. To produce two electrodes of differing coercive fields a nucleation pad was included on one end of one of the electrodes, significantly lowering its coercive field. Figure 5.1 presents MOKE measurements of the magnetisation parallel to the long axis of the pads (My) taken at room temperature of large arrays of the hard (blue line) and soft (red line) pads. The rotation of the nucleation pad of the soft electrode followed by the movement of the domain down the electrode is visible in the soft pad data as a two step switch. The important property of these electrodes is that the hard pad magnetisation is still saturated when the soft pad has completed its reversal, meaning there should be a well defined anti-parallel alignment over a reasonable field range.

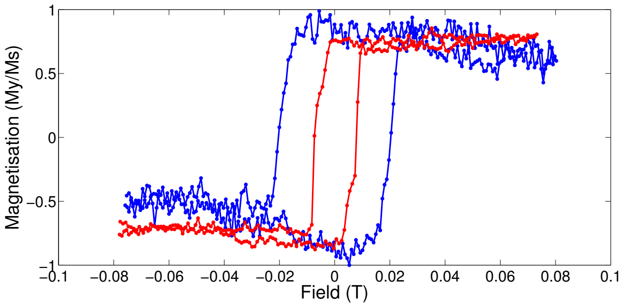

Figure 5.1: Magnetisation along the long axis (M_y/M_S) of arrays of the hard (blue line) and soft (red line) pads as measured by MOKE

The pad magnetisation and domain state are also simulated using OOMMF. Figure 5.2 shows the magnetisation along the long axis of the pads during reversal at a temperature of 0 K, which shows similarities to the magnetisation as measured by MOKE at room temperature, including the nucleation of a domain in the rounded tip of the soft pad, followed by the movement of the domain down the electrode, as can be seen by the two gradients of the soft pad switch. We also observe a large anti-parallel state between 0.15 T and 0.04 T, during which the pads should remain in single domain states, as shown by the constant magnetisation.

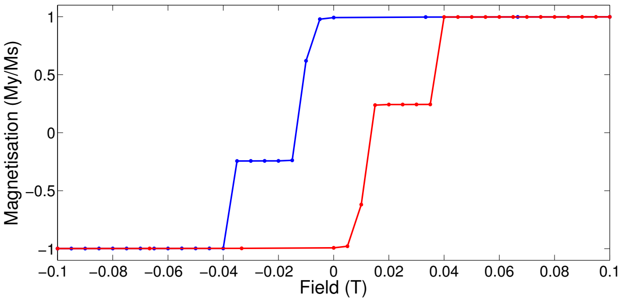

Figure 5.2: Pad magnetisation M_y/M_S calculated as calculated by OOMMF at 0 K

Figures 5.3:5.6 show M_y/M_S the magnetisation parallel to the long axis of the pads during reversal. As can be seen in Figure 5.3 there is no domain structure at 0 T and during reversal a vortex domain nucleates in the rounded tip of the soft pad at 0.01 T, followed by a reversal of the pad as the domain moves down the length of the pad by 0.015 T. The two magnetisation of the pads are then stable until the reversal of the hard pad at 0.04 T, at which point both pads are in a single domain state, aligned parallel with the applied field.

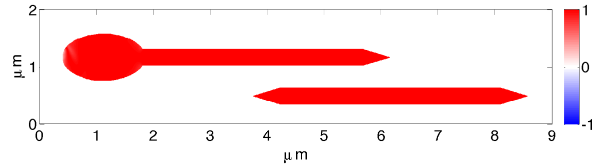

Figure 5.3: Domain Structure as calculated by OOMMF at B=0 T. Colourscale in M_y/M_S

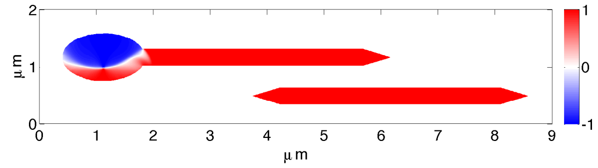

Figure 5.4: Domain Structure as calculated by OOMMF at By=0.01 T at which point a domain forms in the nucleation pad of the soft electrode. Colourscale in M_y/M_S

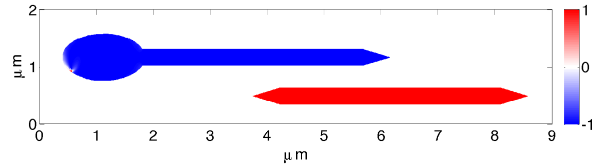

Figure 5.5: Domain Structure as calculated by OOMMF at By=0.015 T at which point the soft pad reverses magnetisation. Colourscale in M_y/M_S

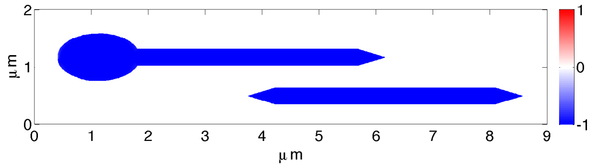

Figure 5.6: Domain Structure as calculated by OOMMF at By=0.04 T at which point the hard pad has reversed its magnetisation. Colourscale in M_y/M_S

5.3 Device 2

Measurements were performed on Device 2 at low temperature in an Oxford helium-flow cryostat described previously. Each of the magnetic pads were contacted by a non-magnetic lead to allow transport measurements through the device, this single contact does not allow transport measurements through the magnetic pads to be performed, however previous results not included in this work had shown that the inclusion of an argon ion plasma cleaning step between the deposition of the magnetic pads and the deposition of the non-magnetic leads ensures Ohmic contact between the metallic layers with no formation of tunnel barriers seen in the previous results, making current annealing and checking of the resistance through the magnetic pads unnecessary. A single carbon nanotube spans the gap between the electrodes allowing current flow between the pads as shown in Figure 5.7, although the CNT in the image is broken as the image was taken after measurement of the device.

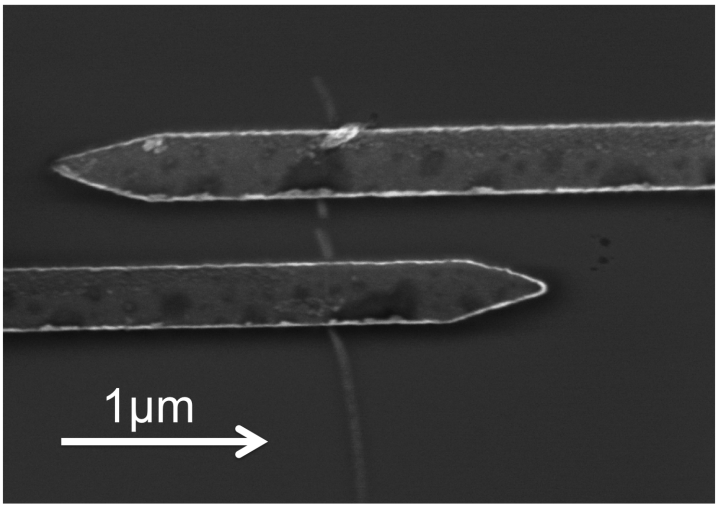

Figure 5.7: SEM of the device after measurement. The carbon nanotube is seen to be broken, which occurred after the measurement of the device.

Figure 5.8 shows an IV through Device 2 at 1.7 K, with a gate voltage of 32 mV, corresponding to a coulomb resonance as seen in Figure 5.9. The steps in the IV curve and the peaks in coulomb peaks in the gate sweep at constant source-drain bias show the device is acting as a quantum dot. No large blocked central region is observed in the IV taken at a coulomb peak, showing there is no tunnel barrier in series with the device.

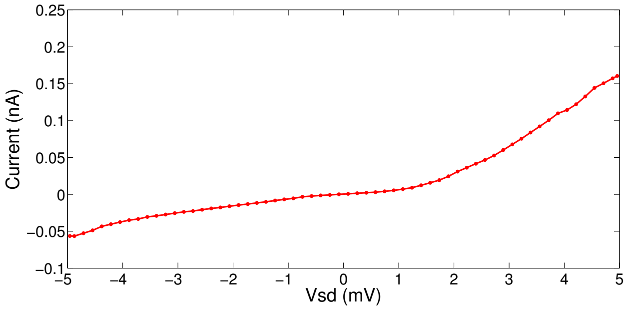

Figure 5.8: IV characteristics of Device 2 taken at V_g=32 mV, corresponding to a coulomb peak, at 1.7 K

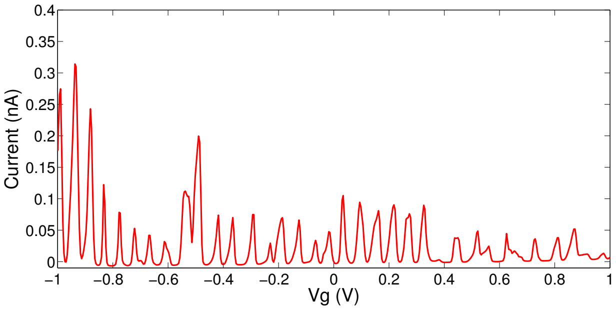

Figure 5.9: Gate voltage dependence of conductance at V_{SD}=4 mV and 1.7 K

Figure 5.10 shows the magnetoresistance of the device at V_g=32 mV with a source-drain bias of V_{SD}=4 mV, corresponding to the conductance peak seen in Figure 5.9. The figure is constructed by averaging 39 consecutive sweeps with no results excluded. Changes in conduction of the device can be seen at the switching fields of the hard and soft pad (∼30 mT and ∼10 mT respectively), however there is also a change in conduction between positive and negative saturation and the anti-parallel state of the device seems be either a higher or lower conductance than the saturation depending on the direction of the sweep. Both of these features are unexpected, there should be no difference in conduction between positive and negative saturation of the magnetic pads and while both positive and negative magnetoresistance have been observed in carbon nanotubes[95] they should not be observed on the same magnetic loop at a constant gate voltage and source drain bias.

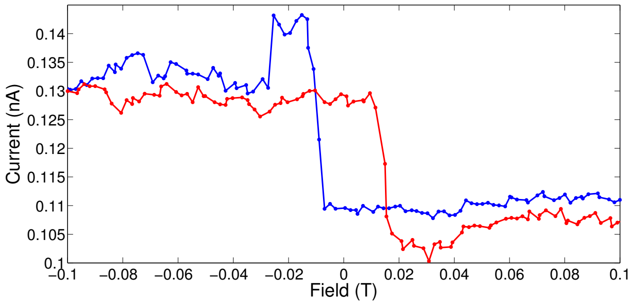

Figure 5.10: Average magnetoresistance of multiple loops taken at V_{SD}=4 mV and V_{g}=32 mV, corresponding to a coulomb resonance. T=1.7 K

Examining the individual loops obtained during the measurement shows that the offset between positive and negative saturation can change with loops showing conduction at positive saturation that is either higher or lower than the value at negative saturation. By grouping the loops into 3 sets by whether their conduction is higher at positive saturation, lower at positive saturation or roughly equal for the two saturations we construct Figure 5.11, which shows the averages of these 3 sets of loops and Figure 5.12, which shows the distribution of the 3 states. A change in conduction in the anti-parallel state is observed for all but the back sweep of the low positive saturation loop and the distribution of the states appears to be random. As positive and negative MR is observed in carbon nanotube QDs at different gate voltages[98] there is the possibility of the positions of the coulomb peaks moving during the measurement, causing the change in sign of the magnetoresistance and also possibly the change in conduction at positive and negative saturation.

To report the magnitudes of the change in conductance from the data we will define the MR on the forward sweep (-$B \rightarrow +B$) as $MR = (I_{\mathrm{P},-B} - I_{\mathrm{AP},+B})/I_{\mathrm{AP},+B}$

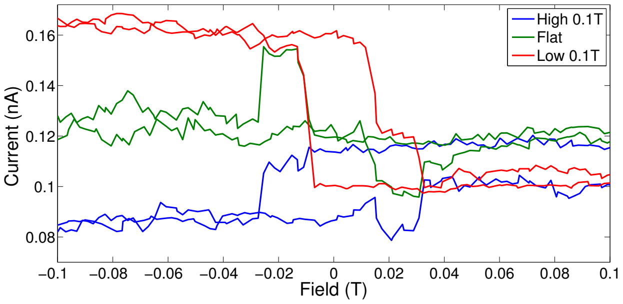

Figure 5.11: Average magnetoresistance of the three groups of MR loops, defined by their relative offsets in conduction saturation. Taken at V_{SD}=4 mV and V_{g}=32 mV, corresponding to a coulomb resonance. T=1.7 K

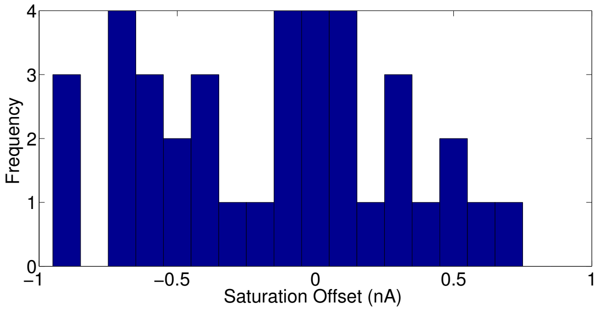

Figure 5.12: Distribution of the saturation conduction offset for each MR loop

and the MR on the back sweep ($+B \rightarrow -B$) as $MR = (I_{\mathrm{P},+B} - I_{\mathrm{AP},-B})/I_{\mathrm{AP},-B}$. This MR does not relate to Julliere's formula because of the non-linearity of the conductance at finite bias, but will allow comparison between results. The average non-selected loop MR of the forward and back sweeps between the P and AP state is $MR = 6 \pm 2\%$. Defining the MR between the saturations as $MR_{\mathrm{sat}} = (I_{\mathrm{P},+B} - I_{\mathrm{P},-B})/I_{\mathrm{P},-B}$, gives us a value of $MR_{\mathrm{sat}} \sim 18\%$. The split loops MR are larger due to not having the signal averaged out between loops with MR of opposite sign and we find the maximum magnitude of the MR for both the anti-parallel states and the saturation offset is $\sim 40\%$.

Reversing the source-drain bias on the device to test the effect of current direction on the magnetoresistance a peak is selected from the gate voltage sweep shown in Figure 5.13 at 32 mV$_{\mathrm{g}}$, at which value the peak at positive bias is also found. The magnetoresistance with these parameters is shown in Figure 5.14 as the average of 49 loops with no selection. As with the previous results these repeated loops are then sorted into 3 sets the averages of which are shown in Figure 5.15 and the distribution in Figure 5.16. The same change in saturation conduction as seen at positive source-drain bias is observed, with the anti-parallel alignment of the magnetic pads observed as a change in conduction also. The 3 sets of loops show a distribution that is mostly high conduction at positive saturation, but includes loops sorted into the other two sets.

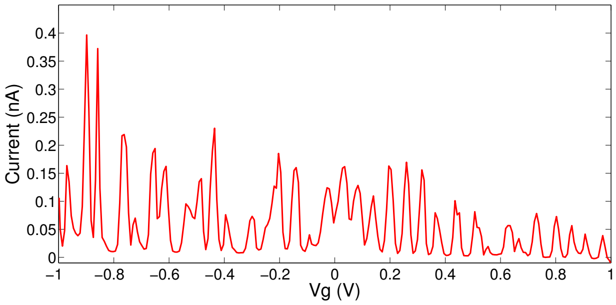

Figure 5.13: Gate voltage dependence of conductance at V_{SD}=-4 mV and 1.37 K

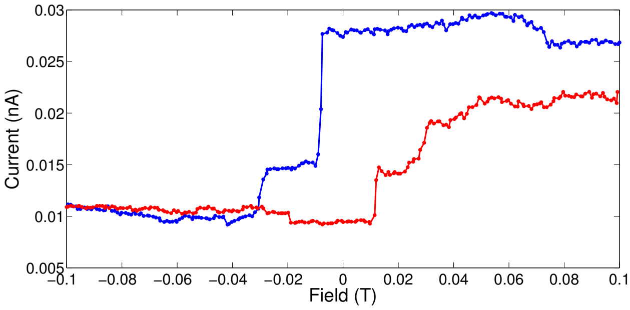

Figure 5.14: Average magnetoresistance of multiple loops taken at V_{SD}=-4 mV and V_{g}=32 mV, corresponding to a coulomb resonance. T=1.37 K

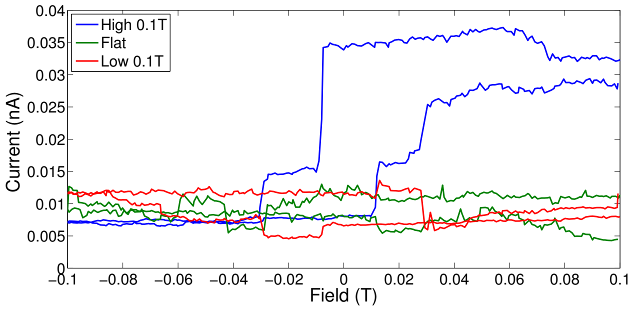

Figure 5.15: Average magnetoresistance of the three groups of MR loops, defined by their relative offsets in conduction saturation. Taken at V_{SD}=-4 mV and V_{g}=32 mV, corresponding to a coulomb resonance. T=1.37 K

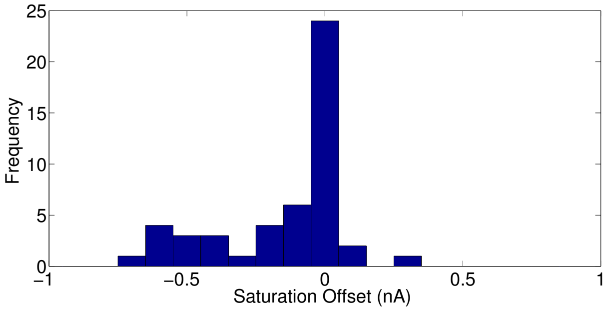

Figure 5.16: Distribution of the saturation conduction offset for each MR loop

Analysing the MR of the unselected averaged loops and the split sets we find both are dominated by the high positive saturation loops which have $MR_{\mathrm{sat}} \sim$ 300% and changes in the anti-parallel state of approximately 100%. The other split sets have far smaller MR values and a higher level of random current fluctuations, although this could be due to the small number of loops that make up these two sets of data. If the 3 sets of MR data with differing signs of MR are produced by fluctuations of the charge on the dot due to changes in the local charge state of the device, then this bias towards high conduction at positive saturation could be explained by a more stable charge state, or possibly a gate voltage that is offset from the coulomb resonance point, meaning that with small charge fluctuations, it is more likely that the QD charge state stays on one side of the coulomb resonance.

A positive or negative source-drain bias of 4mV allows conduction through excited states of the carbon nanotube quantum dot, as can be seen in Figure 5.8 where there are multiple steps in the IV between 0 and 4 mV when the gate voltage is set to a coulomb peak. To remove excited states from the conduction through the carbon nanotube and test a single energy level, AC measurements were performed using the techniques described previously. Figure 5.17 shows the coulomb resonances of Device 2 using a 0.3 mV$_{\text{p-p}}$ AC excitation, a peak conduction of $\sim 8 \times 10^{-4}$ G_0 ($G_0 = 2e^2/h \approx 7.748.10^{-5}\Omega^{-1}$) suggests a weak and asymmetric coupling to the permalloy pads.

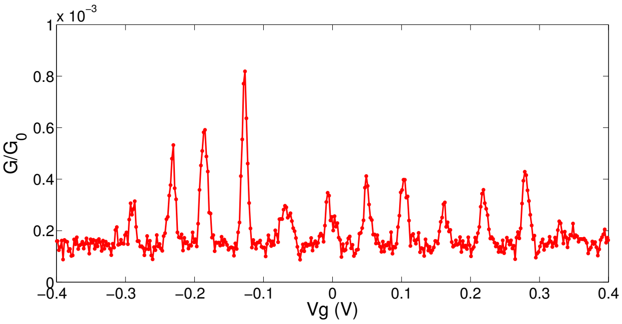

Figure 5.17: Gate voltage dependence of conductance at V_{SD}=0.3 mV$_{\text{AC}}$ and 1.64 K

Figures 5.18:5.23 show the average loops and and split sets of the magnetoresistance measurements performed at 0.3 mV$_{\text{p-p}}$ AC excitation at three different coulomb peaks. This data shows that the saturation offset varying does not depend on current direction, also comparing the flat loops of Figures 5.19 and 5.23 we see that the conduction change in the anti-parallel state may also change sign for the reversal direction.

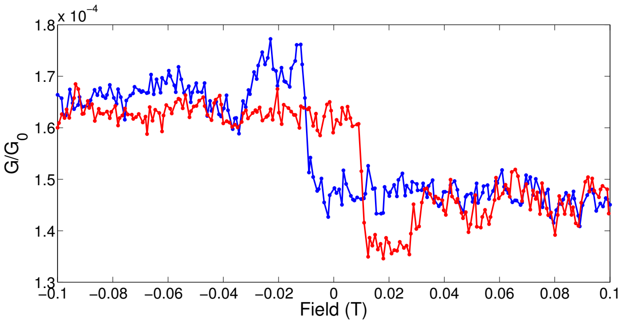

Figure 5.18: Average magnetoresistance of multiple loops taken at V_{SD}=0.3 mV$_{\mathrm{AC}}$ and V_{g}=49 mV, corresponding to a coulomb resonance. T=1.64 K

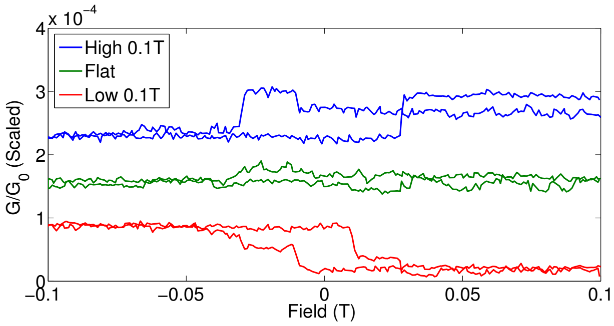

Figure 5.19: Average magnetoresistance of the three groups of MR loops, defined by their relative offsets in conduction saturation. The three curves have been offset for clarity, with 10^{-4} G_0 added to the loop which has high conduction at positive saturation and 10^{-4} G_0 subtracted from the loop at low conduction at positive saturation. Taken at V_{SD}=0.3 mV$_{\mathrm{AC}}$ and V_{g}=49 mV, corresponding to a coulomb resonance. T=1.64 K

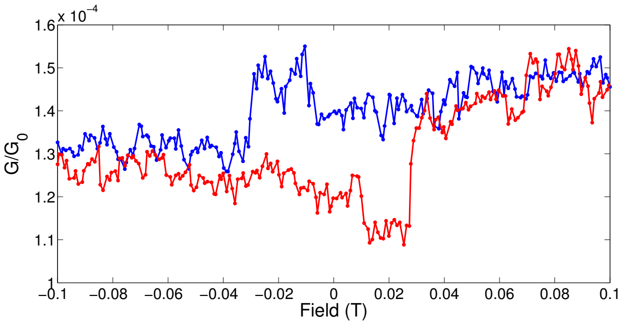

Figure 5.20: Average magnetoresistance of multiple loops taken at V_{SD}=0.3 mV$_{\mathrm{AC}}$ and V_{g}=104 mV, corresponding to a coulomb resonance. T=1.64 K

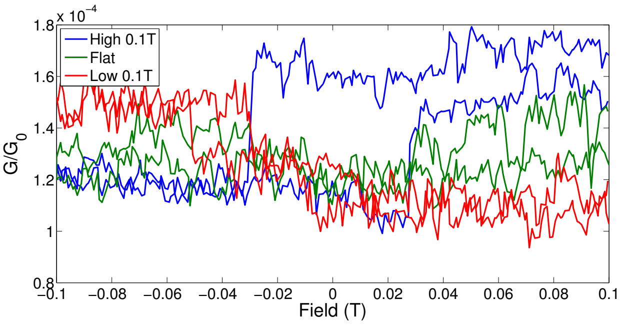

Figure 5.21: Average magnetoresistance of the three groups of MR loops, defined by their relative offsets in conduction saturation. Taken at V_{SD}=0.3 mV$_{\mathrm{AC}}$ and V_{g}=104 mV, corresponding to a coulomb resonance. T=1. 64K

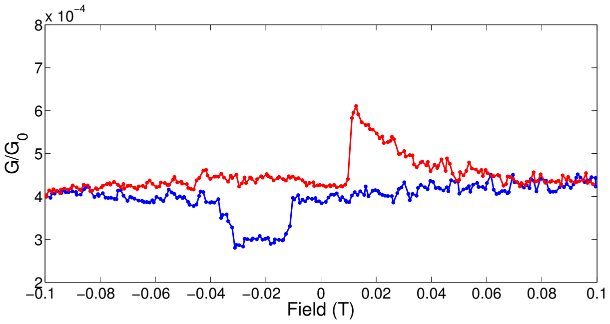

Figure 5.22: Average magnetoresistance of multiple loops taken at V_{SD}=0.3 mV$_{\mathrm{AC}}$ and V_{g}=-189 mV, corresponding to a coulomb resonance. T= 1.62K

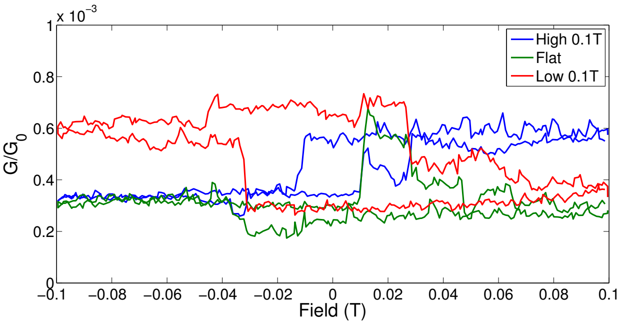

Figure 5.23: Average magnetoresistance of the three groups of MR loops, defined by their relative offsets in conduction saturation. Taken at V_{SD}=0.3 mV$_{\mathrm{AC}}$ and V_{g}=-189 mV, corresponding to a coulomb resonance. T=1.62 K

The maximum changes in conductance of $\sim 60\%$ for the split sets of data and $\sim 10\%$ for the unsorted average values are comparable to the changes seen at V_{SD}=4 mV shown in Figures 5.10 and 5.11, showing that the current ratios at finite bias may be a reasonable approximation of the change in conductance of the device. Comparing both these sets of data to those acquired at V_{SD}=-4 mV seem to show that if we attribute these changes to a shift in the coulomb peak i.e. a change in induced charge on the dot due to some MC effect or SDIPS, we can conclude that $\mathrm{d}G/\mathrm{d}V_{\mathrm{g}}$ for the negative biased results was considerably higher than for the positive and AC biased cases. Leading to the conclusion that as the data was acquired at conductance peaks, there was a change in charge state on the dot between measurement of the conductance peaks and MR measurements, leading to a higher $\mathrm{d}G/\mathrm{d}V_{\mathrm{g}}$

Interestingly the magnetic loops that do not show an offset in saturation conduction show MR of opposite sign between the back and the forward sweep in the anti-parallel state. Work published by Tombros et al.[95] shows a change in sign of the MR between the two anti-parallel states for a Co contacted CNT, where results are also presented showing spin accumulation from 4-terminal non-local measurements, seeming to confirm that the change in resistance is due to a spin transport effect. Magnetic loops that show no saturation offset in this work may also be attributed to spin transport, as from the other two sets of loops we observe that the change in conduction between saturations is larger than the change between the parallel and anti-parallel state. This means that if the changes in conduction are due to induced charge on the QD, the observed change in the anti-parallel state may be due to spin-dependent transport rather than coulomb peak movement.

Making no assumptions about the transport through the device, we can conclude that the magnetisation orientation of the Py pads changes the conductance through the device, because changes in conduction always occur at the coercive fields of the device. The saturation offset observed for most measurements shows that some property of the transport is sensitive to the magnetic orientation of the pads, despite the fact that there is no difference in energy of the magnetic pads between a positive and negative applied field of the same magnitude. With the possible exception of a domain trapped near the nanotube in one orientation

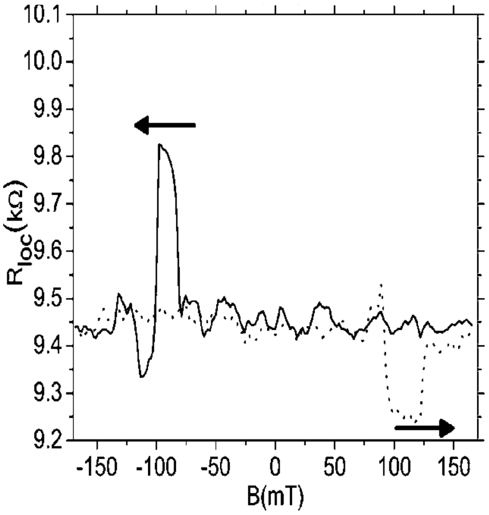

Figure 5.24: Two terminal resistance of a carbon nanotube showing both positive and negative MR in the same magnetic loop at 4.2 K. Taken from Tombros et al.[95]

but not the other. From OOMMF simulations and their similarity to observed switching behaviour this does not seem likely. It seems as though there is some internal quantisation axis in the CNT
To gain further insight into the mechanism of these conductance changes the position and magnitude of the coulomb resonance during magnetic reversal, and hence the gate voltage dependence of the MR must be found, results presented on Device 3 in the next section were taken with this aim in mind.

5.4 Device 3

Device 3 follows the same design as Device 2, where a single carbon nanotube spans between two permalloy pads. The differential conductance dI/dV at 300 mK as a function of backgate voltage V_{g} and source drain bias V_{SD} is plotted in Figure 5.25, showing the coulomb blockade diamonds of the quantum dot. The full width half maximum (FWHM) of the coulomb resonance around zero bias is 0.44 ± 0.03 meV, which is larger than the thermal energy $k_B T$=0.026 meV, suggesting the resonance is broadened by the coupling to the leads (Γ broadening) and the low conductance around zero bias of $\sim 0.1 \times 10^{-3}$ G_0 shows the coupling to be asymmetric.

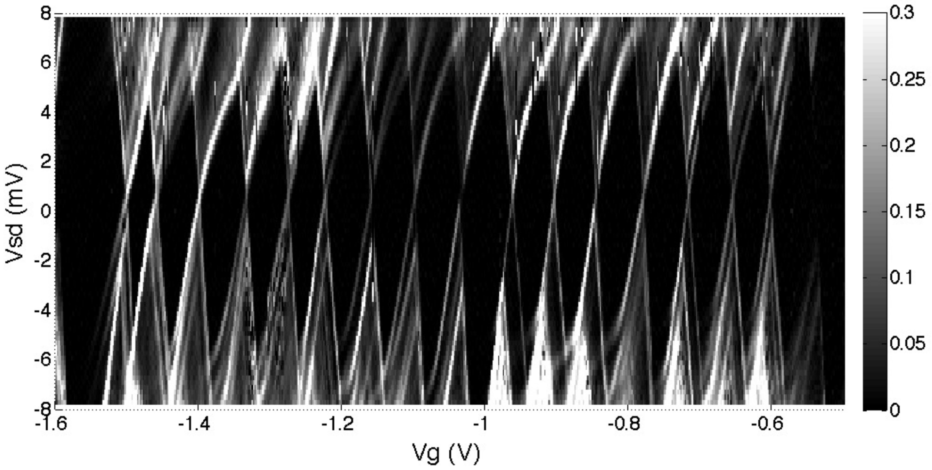

Figure 5.25: dI/dV of the device taken at 300mK showing coulomb diamonds, colourscale in 10^{-3} G_0

By measuring the coulomb blockade diamonds the charging energy, U_{C}, was found to be 6.0 ± 0.2 meV and the energy spacing of the CNT, ΔE, was found to be 1.44 ± 0.06 meV, with the coupling of the CNT to the gate $\alpha = \frac{C_{\mathrm{gate}}}{C} = 0.113 \pm 0.004$. The ratio of $\Delta E/U_{\mathrm{C}}$=0.24 indicates that this is a single-walled carbon nanotube.[58]. As $k_B T \ll \hbar\Gamma < \Delta E$ the line shape of the coulomb resonances at zero bias should have the Breight-Wigner form[57]:

$$G_{\mathrm{BW}} = \frac{2e^2}{h}\frac{\Gamma^{\mathrm{H}}\Gamma^{\mathrm{S}}}{\Gamma^{\mathrm{H}}+\Gamma^{\mathrm{S}}}\frac{\Gamma}{(\frac{\varepsilon}{\hbar})^2+(\frac{\Gamma}{2})^2}$$

where Γ^{H} and Γ^{S} are the coupling to the hard and soft pad respectively, $\Gamma^{\mathrm{H}}+\Gamma^{\mathrm{S}} = \Gamma$ the overall coupling to the leads and ε is the separation between the energy level of the quantum dot and the Fermi levels of the pads. Taking the maximum value of the conductance at $\varepsilon = 0$ and the FWHM of the peak to be Γ results in $\hbar\Gamma^{\mathrm{H/S}}$=0.43±0.06 meV / 0.009±0.001 meV.
Results shown previously have indicated that shifts in the energy levels of the quantum dot may occur on magnetic reversal of the ferromagnetic pads, to test this the line shape of the 3 coulomb resonances at a range of gate bias between -1 V and -1.2 V were measured during magnetic reversal of the pads at V_{SD}=4 mV bias. At this bias we expect a broadening of the coulomb blockade peak and so choose to fit an inverse $\cosh^2$ function to each of the resonances as an estimate of the line shape of the curve as would be in the case $\Delta E < k_BT < U_{\mathrm{C}}$. An example of the coulomb peaks with fits is shown in Figure 5.26 with experimental data shown in blue and fitted curves in red.

The peak position for the resonances extracted from the fit can then be plotted versus applied magnetic field during reversal. Figure 5.27 shows the peak position during magnetic reversal of the peak at V_{g} ∼-1.04 V which we will label peak 1, with the peaks at larger negative gate voltages peak 2 and peak 3. This data is the average of 30 loops, all of which show a similar offset in saturation with the positive saturation being at a more negative gate voltage. This is true of all the 3 peaks with the offsets in gate voltages, calculated as the difference in average peak position at $B >$0.05 T and $B < -0.05$ T, resulting in peak 1 offset = 7.4±0.3 mV, peak 2 offset = 6.1±0.2 mV and peak 3 offset = 4.4±0.3 mV. The change in the peak position occurs at the switching field of the hard pad (∼0.03 T) which makes the position of the peak depend on the magnetisation direction of the hard pad, invariant with applied field, apart from some small change observed at a positive applied field. This is unexpected as energy level movement has previously been proposed and observed in quantum dots contacted to ferromagnetic electrodes[86, 87, 88] where Zeeman shift or anisotropic energy

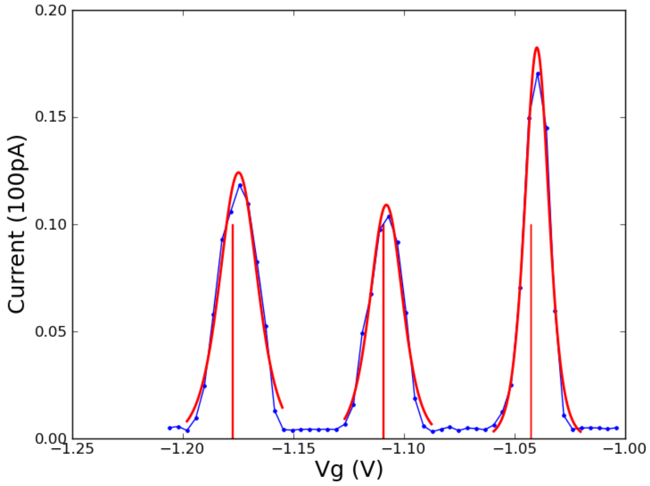

Figure 5.26: Example of 3 coulomb resonances at V_{SD}=4 mV, shown in blue, with inverse $\cosh^2$ fits shown in red

changes have altered the electrostatic potential of the magnetic electrodes, moving the levels of the dot through a gating effect. In this work the movement occurs between two states in which there is no change in the chemical or electrostatic potential of the magnetic electrodes i.e. at saturation not 90°.

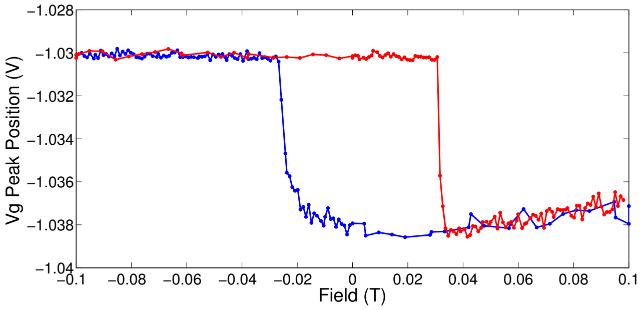

Figure 5.27: Movement of peak 1 from fits of the coulomb blockade resonance, all 3 peaks have show similar dependence with field.

Figure 5.28 shows the maximum value of peak 1 from the fitting during magnetic reversal, all the peaks maxima are very similar to this.

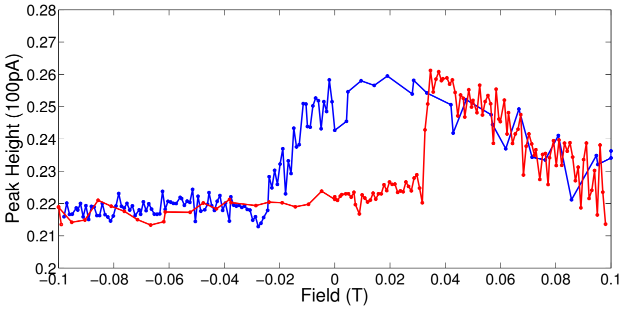

Figure 5.28: Maximum value of peak 1 from fitting to the coulomb blockade resonance. All three peaks show similar dependence with field.

To compare the conduction at parallel and anti-parallel alignment of the magnetic electrodes the magnetic loops can be split into 4 states:

- Parallel 1: parallel alignment of the pads at positive saturation
- Anti-Parallel 1: anti-parallel alignment of the pads sweeping from positive to negative field
- Parallel 2: parallel alignment of the pads at negative saturation
- Anti-Parallel 2: anti-parallel alignment of the pads sweeping from negative to positive field

The four defined magnetic states are illustrated on the magnetisation reversal loop of the electrodes in Figure 5.29. In this way the MR can be calculated between Parallel 1 and Anti-Parallel 1, together with Parallel 2 and Anti-Parallel 2, ignoring the change in peak position that occurs when the hard pad switches magnetisation. The change in conduction between the two saturation states can also be compared using Parallel 1 and Parallel 2.

Figure 5.30 shows the MR calculated as $(I_{\mathrm{P}} - I_{\mathrm{AP}})/I_{\mathrm{AP}}$ for the back sweep of the magnetic loop 0.1 T → -0.1 T, and Figure 5.31 the corresponding forward sweep. The sign of the MR is stable on the back sweep but can reverse on separate loops for the forward sweep, these two states are separated and plotted in Figure 5.31. To compare the saturation MR we use $MR_{\mathrm{sat}} = (I_{+\mathrm{B}} - I_{\text{-B}})/I_{\text{-B}}$, as shown in Figure 5.32.

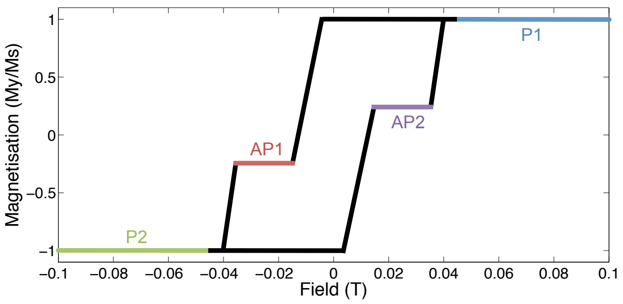

Figure 5.29: The four magnetic states of the device used to calculate the magnetoresistance of the device.

Figures 5.33:5.35 show comparisons of the line shapes of the coulomb peaks in the 4 magnetic states.

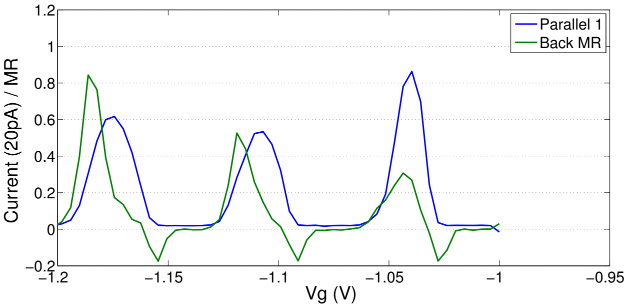

Figure 5.30: 3 peak back sweep MR, shown in green and conduction in the Parallel 1 state, shown in blue.

The movement of the coulomb resonances seen at saturation in these measurements seems to confirm that changes in saturation conductance of earlier devices are due to changing charge on the QD, although the source of these changes in charge is not obvious. The maximum change in charge due to the MC effect for both pads at 0.04 T is equal to 0.02 e, which is small compared to the average shift in the coulomb resonances between saturations of 0.11 e, which together with the fact that the charge induced on the QD should be symmetric about B=0 T makes it unlikely to be the cause of the observed shift.

Spin dependent interfacial phase shifts (SDIPS) can change the position of coulomb

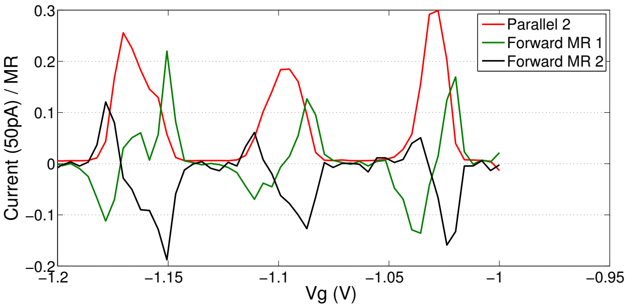

Figure 5.31: 3 peak forward sweep MR. The MR was found to have unstable and reverse sign, so similar loops were extracted from the data and averaged to make MR 1 (green line) and MR 2 (black line). The red line is the conduction in the Parallel 2 state.

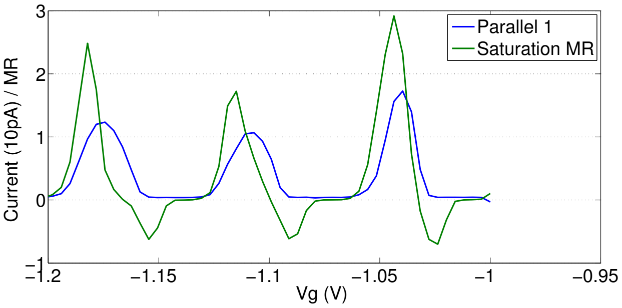

Figure 5.32: 3 peak saturation MR, shown in green and conduction in the Parallel 1 state, shown in blue.

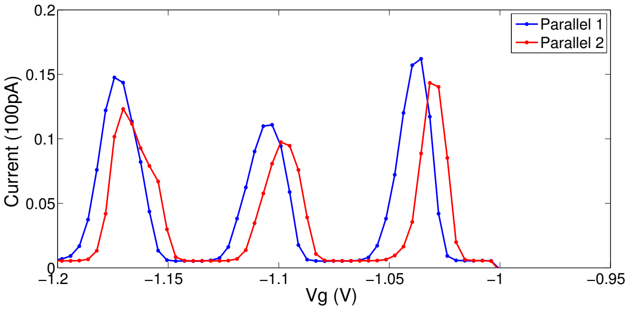

Figure 5.33: Coulomb resonances in the Parallel 1 (blue line) and Parallel 2 (red line) states.

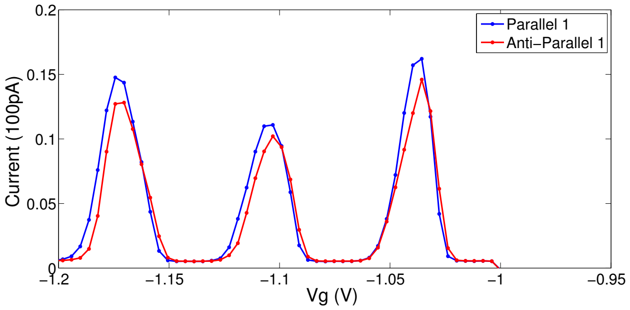

Figure 5.34: Coulomb resonances in the Parallel 1 (blue line) Anti-Parallel 1 (red line) states.

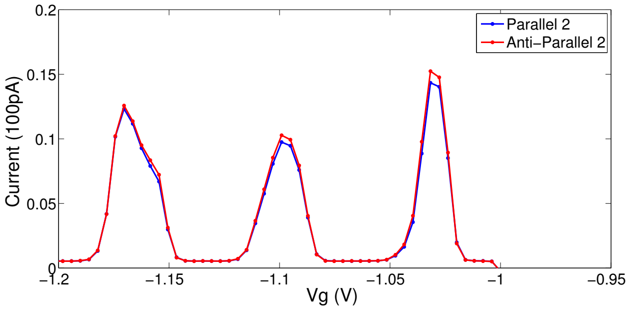

Figure 5.35: Coulomb resonances in the Parallel 2 (blue line) Anti-Parallel 2 (red line) states.

peaks between parallel and anti-parallel alignment and could be used to explain the change in energy levels at saturation if the spin of the electron for each resonance is fixed and does not change upon reversing the field direction and pad magnetisation for some reason. This is due to the phase shift of a electron on reflection from a magnetic interface depending on the magnetisation of the FM and the spin of the electron. From high field measurements of the position of the coulomb resonances shown in Figure 5.36 we see no high field dependence for peak1, shown in Figure 5.36(a), and an alternating shift in position between peak 2 (Figure 5.36(b)) and peak 3 (Figure 5.36(c)). The alternating shift shows that the high field movement is dependent on the Zeeman shift of the electron spin, rather than an induced charge on the QD due to the MC effect, which would shift each energy level in the same direction and also identifies the electron added at peak 2 is aligned with the applied field, while peak 3 is aligned opposing the applied field. So there is no fixed electron spin for each resonance and SDIPS cannot explain the offset between the two saturations. The gradient of a linear fit of the high field data beyond the hard pad switch of peak 2 and peak 3 corresponds to a g-factor of $g = 0.92 \pm 0.08$, from $g = \alpha\mu_B \mathrm{d}V_g^{\mathrm{PEAK}}/\mathrm{d}B$. While not the expected value of 2 for electrons in a CNT[78, 79, 81] has been observed for CNTs in other work[82] and may be an indication of a spin-orbit coupling in the CNT[56]. This small change in position with applied field also makes the observed change in the energy levels of the QD between saturations unlikely to be caused by a stray field effect, as the movement between the saturation energy levels would correspond to a field of approximately 12 T. The stray field in the area of the nanotube parallel and perpendicular to the long axis of the pads is calculated as < 2.2 mT from OOMMF simulation.

When comparing the measurements of the positions of coulomb resonances in the low field (Figure 5.27) and high field (Figure 5.36) the offset was seen to change from higher at negative saturation to lower at negative saturation, this change occurred only once over the time the device was measured and was not seen to return to the previous state upon repeated measurement of the low field coulomb peak movement.

One other feature seen in these measurements is the shoulder that appears on peak 3 when the magnetisation of the hard pad is in one orientation, but is not observed in the other orientation. As these measurements were taken at finite bias this is probably due to the conduction through an excited state of the dot rather than the Zeeman splitting of a spin-degenerate energy level due to the separation of the energy levels being larger than could be accounted for through the Zeeman energy and that the field at the dot should be of the same magnitude in each case. This allowed conduction through an energy level in one orientation but not the other could be an indication of the spin dependence of the excited state.

Taking the difference in saturation conductance to be caused by some property of the hard magnetic pad switching, the MR between the AP and P states can then be compared to models of the spin-dependent transport through CNT QDs. We observe a gate dependent MR that varies from positive to negative about the

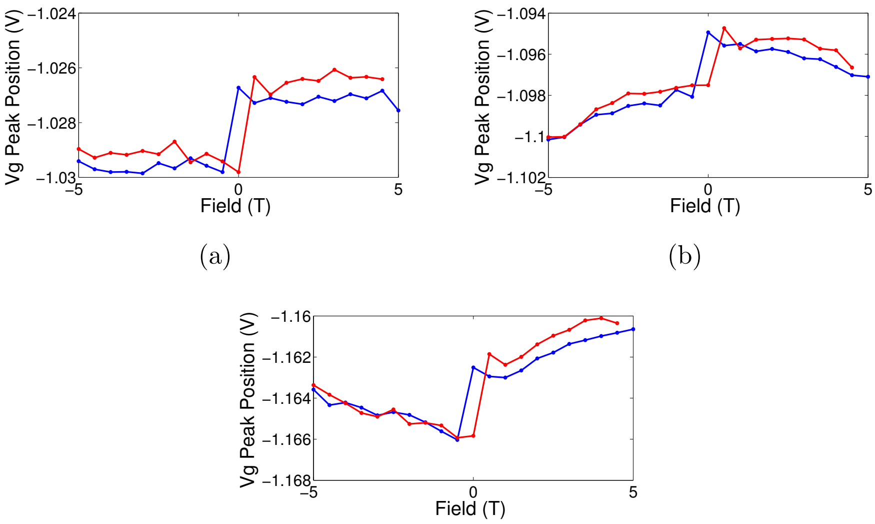

(a)

(b)

(c)

Figure 5.36: High field dependence of coulomb blockade maximum position for peak 1 (a), peak 2 (b) and peak 3 (c).

coulomb resonance peak, with an asymmetry to the magnitude of the MR. This fits well with theory of SDIPS as described by Cottet et al.[91] as the oscillating MR is caused by a spin dependent energy level shift between the P and AP states. However the MR we observe has the same symmetry for all three resonances, which does not fit with the observed orientation of electron spin from the high field measurements, although this disparity could be negated if we consider that the shell filling of the QD may be dependent on the magnetisation of the electrodes and the applied field, as observed in some devices[78, 84], in which case there may be a different shell filling order in the low field measurements to that which is observed at high field.

Comparing magnetoresistance measurements on NiPd CNT QDs presented by Sahoo et al.[98] we see some similarities, such as the gate dependence of the MR oscillating over the period of the coulomb resonances and the magnitude of the MR observed in the forward sweep in Figure 5.31, with the larger MR values as seen in the back sweep due to a larger SDIPS enhancing the effect. Some differences between results presented in this work and those in the work of Sahoo et al. include the lack of MR in the blocked regions between resonances, although

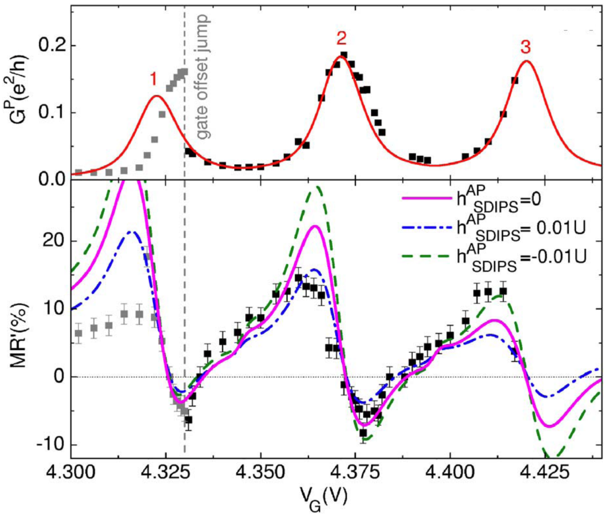

Figure 5.37: Gate dependent MR and gate dependent conductance of a CNT QD contacted with NiPd electrodes. In the top panel experimental results are shown in black, with calculated conductance in red. In the bottom panel fits to the experimental MR in black, with varying SDIPS in purple, blue and green. From Cottet et al.[91], data from Sahoo et al.[98]

this is easily explained by the conductance in between the coulomb resonances in this work being too low to measure on the amplification scale used to acquire the data. The current levels measured between the coulomb resonances in this work are due to amplifier offset, and when comparing the current values measured in the blockaded regions there is no discernible difference between $V_{\text{SD}} = 0$ mV and $V_{\text{SD}} = 4$ mV. We also observe a change in sign of the MR between magnetic loops of the forward sweep, with the only way this could be described by SDIPS theory would be if there was an change in the sign of the electron spin added to the QD at each resonance.

The line shape of the 4 coulomb resonances between -1.18 V and -1.45 V were also measured during magnetic reversal of the pads at V_{SD}=4 mV bias. Figure 5.38 shows an example of the peak position during reversal, with the other 3 peaks looking very similar to this. This data set consists of 9 magnetic loops compared to the previous set of 3 peaks which consisted of 30 repeats, for this reason the data presented here is an average of 4 loops out of the 9, with 5 loops discarded that included random switching events to make the data presented clearer. Again by splitting the loop up into 4 states the V_{g} peak movement between the states and MR can be found. The ΔV_{g} between the states is shown in the table below, the MR is calculated as previously and shown in Figures 5.39:5.41 and the comparison of the line shape of the coulomb peaks in each state in Figure 5.42:5.44.

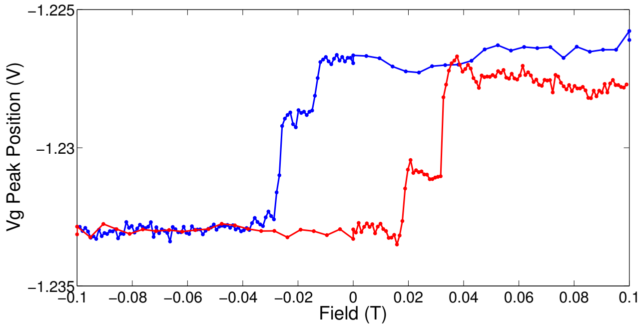

Figure 5.38: Coulomb resonance peak movement of the set of 4 peaks.

Peak	ΔV_{g} Saturation (mV)	$\Delta V_{\mathrm{g,P1/AP1}}$ (mV)	$\Delta V_{\mathrm{g,P2/AP2}}$ (mV)
1	6.5 ± 0.5	2.5 ± 0.3	3.0 ± 0.8
2	6.9 ± 0.8	1.9 ± 0.4	1.8 ± 0.5
3	6.4 ± 0.9	1.8 ± 0.4	1.8 ± 0.5
4	7.5 ± 0.9	1.8 ± 0.4	2.1 ± 0.6

Differences between the data acquired on these four points when compared to that on the three points between gate voltage values of -1 V and -1.2 V include a larger ΔV_{g} between the parallel and anti-parallel states that is resolvable in the fitted coulomb peak data shown in Figure 5.38 and subsequent larger MR values seen on the forward and back sweeps. Due to similar ΔV_{g} between saturations, the MR_{sat} is similar between the two sets of peaks The MR instability in the sign

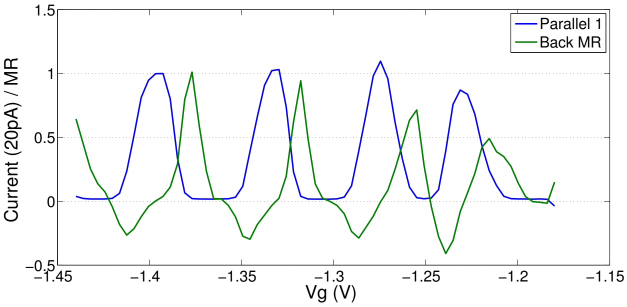

Figure 5.39: 4 peak back sweep MR, shown in green and conduction in the Parallel 1 state, shown in blue.

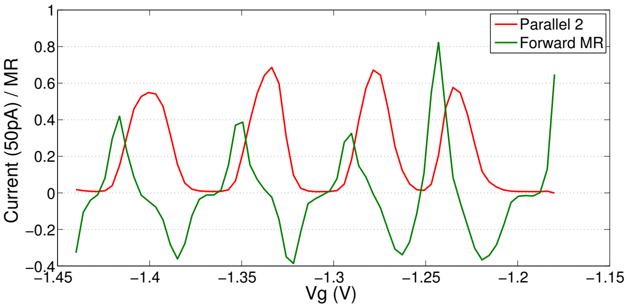

Figure 5.40: 4 peak forward sweep MR, shown in green and conduction in the Parallel 2 state, shown in red.

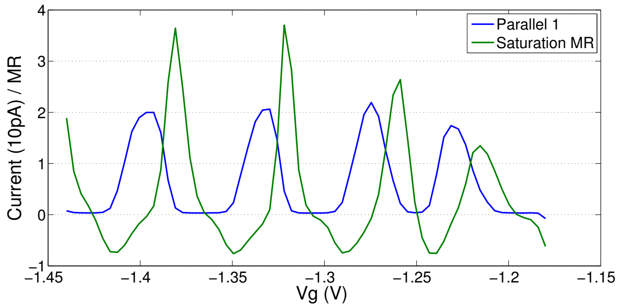

Figure 5.41: 4 peak saturation MR, shown in green and conduction in the Parallel 1 state, shown in blue.

of the MR between separate MR loops is also not observed, with the sign of the MR stable and of opposite values for the forward and back sweep. Measurements of the high field dependence of the position of the energy levels also differ, with

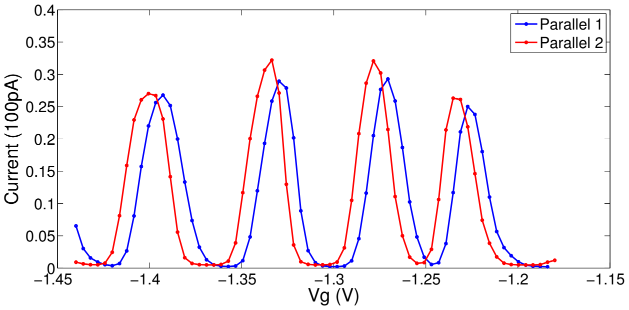

Figure 5.42: Coulomb resonances in the Parallel 1 (blue line) and Parallel 2 (red line) states.

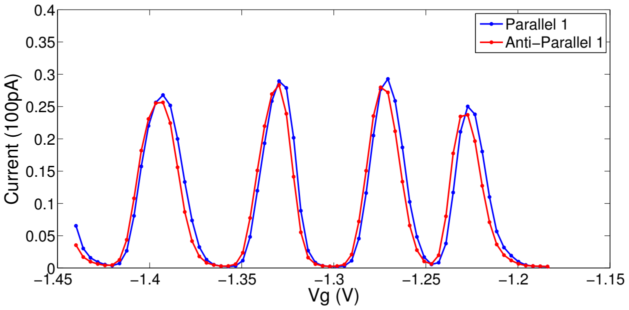

Figure 5.43: Coulomb resonances in the Parallel 1 (blue line) and Anti-Parallel 1 (red line) states.

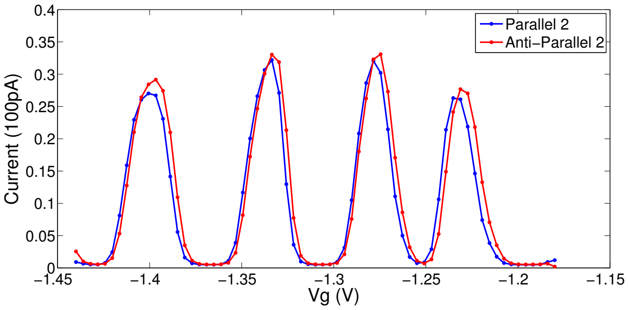

Figure 5.44: Coulomb resonances in the Parallel 2 (blue line) and Anti-Parallel 2 (red line) states.

all the energy levels showing the same increasing (less negative) position of the coulomb resonances. This could be due to MC effect, which lowers the energy of the magnetic pads at high field, causing electrons to flow into the pads from the measurement lines, increasing the negative charge of the pads. This negative charge gates the device in the same way a negative potential applied to the gate electrode would and removes charge from the dot, causing the coulomb resonances to appear at higher gate voltages, although the movement of the peaks has the same gradient as that of the 3 peaks of ~ 0.5 mV/T, corresponding to an electron energy shift with $g \sim 1$. The calculated MC effect caused by the Zeeman shift of the pads is actually far larger than this at 30 mV/T.This means that the observed energy level shift is unlikely to be caused by the MC effect, especially when considering the three peaks shown previously showed alternating shifts in energy at the same gradient.

Figure 5.45 shows the magnetoresistance of the device averaged over a range of gate voltages equal to the 4 coulomb resonances to try to find the magnetoresistance of the device excluding any peak motion. Interestingly we see no saturation offset in the MR and a changing sign of the MR between the forward and back loops similar to that seen in the zero offset data of Device 2, shown in Figure 5.11, although in this data the change in conduction on the back sweep is at ~ 0 T rather than the expected coercive field of the soft pad. The magnitude of the MR seen in the anti-parallel state is $5 \pm 1\%$. If we assume that the effect that is moving the coulomb peak positions is not also affecting the conductance of the device then this change in conduction is due to the spin-dependent transport of the device.

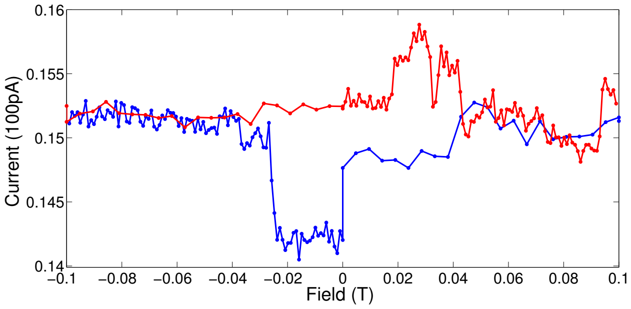

Figure 5.45: Average MR over all 4 peaks, V_{SD}=4 mV.

Measurements of the 4 peaks were also performed at $\mathrm{V_{SD}}$=1.5 mV, these results showed a similar change in peak position with field as at V_{SD}=4 mV, as shown in Figure 5.46 with a peak offset of $\sim$ 6 mV, showing the peak movement is not dependent on source-drain bias. Similar MR is also observed as shown in Figure 5.47, with the forward sweep MR similar but of opposite sign and the saturation MR similar to that observed at V_{SD}=4 mV.

The MR from the 4 consecutive peaks at either bias do not fit with SDIPS theory in that the MR about each of the four peaks has the same symmetry meaning the spin of the electron added to the dot in each resonance would have to be the same which is not possible for shell filling in a CNT due to the Pauli exclusion principle, two consecutive peaks that move in the same direction are expected for a four-fold degenerate ground state and there may at most be 3 consecutive peaks that move in the same direction between the P and AP states if the magnitude of h_{SDIPS} is of the order of the peak spacing, causing spin mixing. Also the MR

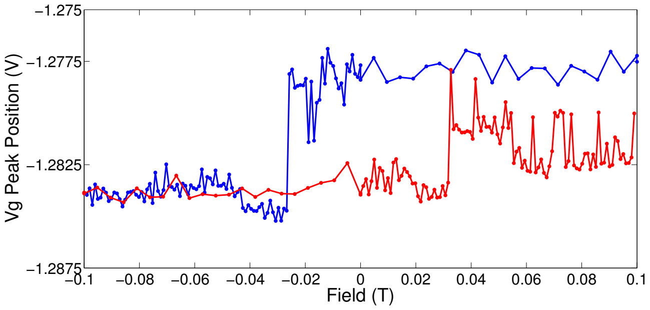

Figure 5.46: V_g peak movement of the set of 4 peaks at V_{SD}=1.5 mV.

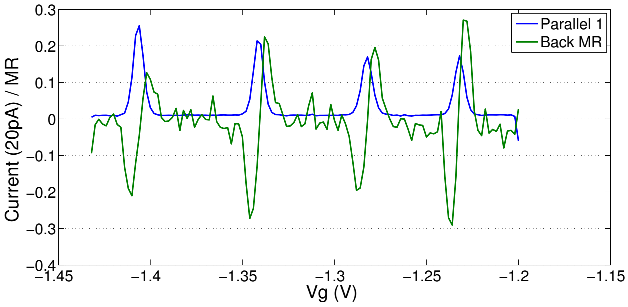

Figure 5.47: 4 peak back sweep MR at V_{SD}=1.5 mV.

observed for the $V_{\mathrm{SD}} = 1.5$ mV case shown in Figure 5.47 does not show the same asymmetry expected for SDIPS as the measurements at higher bias do and the shape of the MR closely matches $\mathrm{d}G/\mathrm{d}V_{\mathrm{g}}$ as would be expected for a MC effect. However, as there is no MC effect observed at high field large enough to account for the large changes in peak position the data cannot be said to fit this model either.

So if neither model for coulomb blockade peak movements with applied field fit the properties of this device, then we must consider other options. As the main differences between this device and other published results are the fact that the Py contacts are sputter deposited and that it has extremely asymmetric coupling to its electrodes, it could be proposed that the coupling of the poor contact is changing during magnetic reversal of the pads. However the magnetostriction of permalloy is very low[36], making it unlikely that physical movement of the electrode is occurring to change the coupling. A change in the asymmetry of the coupling may change the relative slopes of the sides of the coulomb peak, shifting the maximum value slightly as discussed by Jalil et al.[88] but it will not move the absolute positions of the peaks as observed between the two saturations. For that to occur the capacitative coupling between the electrodes and the CNT would have to change and as this is defined by the position and size of the electrode relative to the nanotube, this does not seem likely. However, a change in the coupling to the CNT that moves the position electrons tunnel into the CNT and hence the length of the quantum dot may produce the results observed. As the addition energy is inversely proportional to the length of the CNT (L)[114], a large change in V_{g} peak position may be due to a small change in E_{add}, if the energy level of peak in question is far from a K point, as the change will be multiplied by the number of peaks between it and the K point. For this to be the case a difference in E_{add} between the two saturations ($\Delta E_{\mathrm{add}}^{\mathrm{SAT}}$) that increases linearly with peak number would be expected. Figure 5.48 shows $\Delta E_{\mathrm{add}}^{\mathrm{SAT}}$ for the 7 peaks investigated in this chapter and while the average change in $E_{\mathrm{add}}/e\alpha$ between the two saturation states of ~ 0.7 mV would be able to account of the coulomb peak saturation offset with the peaks investigated lying a reasonable distance away from a K point there does not appear to be a linear correlation to the points, which would be expected to be observed, meaning that either this explanation is not the case, or that the change in $\Delta E_{\text{add}}^{\text{SAT}}$ is small and the data acquired is too poor to observe it.

Liu et al.[115] observe a similar offset in conductance between saturation states

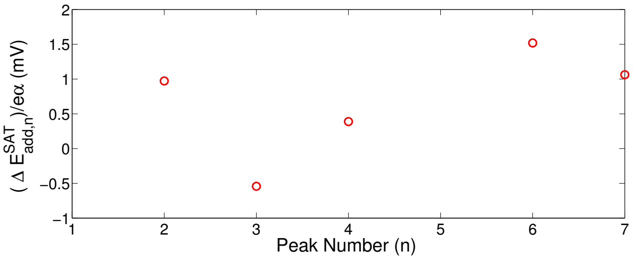

Figure 5.48: Changes in E_{add} between the two saturation states of the magnetic electrodes for consecutive peaks measured. $E_{\text{add}}/e\alpha$ is calculated as the separation between the n+1 and n peaks, numbered from n=1 at the peak located at $V_{\text{g}} \sim -1.4$ V. Statistical errors too small to be shown.

in Co contacted CNT QDs, as shown in Figure 5.49. The explanation given for the saturation offset is a spin-orbit interaction splitting the energy of spin up and spin down states of the QD, which remains constant at positive and negative saturation. These two spin split levels are both within the source-drain bias window, but have different tunnelling probabilities due to their difference in energy. This case is similar to that seen in Device 3, which also shows signs of spin-orbit interaction in its reduced g-factor.

The problem with this explanation is that while a spin-splitting of the QD energy levels is reasonable, the invariance of the spin-split energies with either applied field or pad magnetisation is not, as it implies there is some preferential spin orientation intrinsic to the CNT.

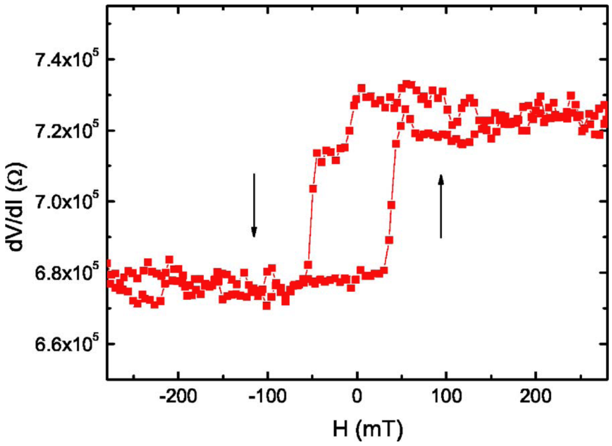

Figure 5.49: Hysteretic saturation MR observed in a Co contacted CNT QD at 0.5 K, coercive fields of the electrodes are estimated to be ∼50 mT. Taken from Liu et al.[115]

To conclude, in this chapter we have observed that changes in conduction of carbon nanotubes in the coulomb blockade regime between saturation in the parallel and anti-parallel states may be attributed to changes in the energies of quantised states in the QDs. However the movement of these energy levels does not fit with current theory of magneto-coulomb effects due to:

- the magnitude of the low field peak shifts being many times that predicted;
- no significant high field movement of the peaks;
- the effect not being symmetric about B=0 T.

SDIPS has also been considered as a possible cause for the changes in energy of the coulomb resonances, but has also been discounted due to:

- the symmetry of the magnetoresistance observed over four consecutive coulomb resonances;
- the proportionality of the observed MR with dG/dV_g observed at low source-drain bias.

The magnetoresistance averaged over the gate voltage range of the four peaks shows a small MR with a changing sign on the forward and back sweeps similar to that shown in the magnetic loops of Device 2 that show no saturation offset. We have identified part of the field dependence of the conductance to be spin-dependant transport. Although changing sign of the MR between forward and back sweeps is not expected in the spin dependent transport it has been previously observed by Tombros et al.[95] in a device that also demonstrates spin accumulation.

We are therefore left with the unusual conclusion that there is an internal quantisation axis in the tube that means the $G_{(B=\uparrow\uparrow)} \neq G_{(B=\downarrow\downarrow)}$.

Chapter 6

Conclusions and Future Work

6.1 Conclusions

Results of this work have shown that stable contact can be made between permalloy and carbon nanotubes, although the zero bias conduction of the devices was two to three orders of magnitude lower than the theoretical quantum conductance of a CNT. When comparing these conductance values to those of other published results on Py contacts to nanotubes, they are of similar magnitudes to the results of Morgan et al.[101] but significantly lower than those obtained by Aurich et al.[100] of 0.6 G_0. However neither of the published results show regularly spaced coulomb blockade features as seen in devices shown in this work, indicating the formation of stable CNT QDs. Despite the low conductance of each device the FWHM of the coulomb resonances of Device 3 indicate good coupling of one of the contacts of $h\Gamma = 0.43 \pm 0.06$ meV indicating that good contact between Py and CNTs has been achieved using the methods we employed. Published results on CNTs show maximum conductance values of 0.1 G_0 with couplings of $\hbar\Gamma^{\mathrm{L(R)}} = 0.3625, (0.0215)$ meV[92].

Devices 1 and 2 showed indications that the charge state of the QDs was changing with the magnetic orientation of the electrodes and measurements performed on Device 3 allowed the changing charge state to be observed. Whilst the magneto-coulomb effect and spin-dependant interfacial phase shifts both predict movement of the coulomb blockade resonances, neither theory fits the observed behaviour of the devices. With the MC effect being discounted as the cause of the shifts due to the magnitude of the movements seen at low field being 10 times that predicted by MC effects and through the lack of significant peak movement at high field. A large SDIPS could account for the magnitude of the peak movements observed, however its dependence on the spin of the electron involved in the transport means that the direction of the shift should not be constant over four consecutive coulomb resonances because of the spin-dependant shell filling of CNTs. This combined with the lack of asymmetry about the coulomb peaks of the MR observed at low bias in Device 3 seems to rule this out as an explanation of all the characteristics of the devices observed.

Another possible interpretation of the peak movements considered include domains trapped in the FM pads near to the contact point of the nanotube, however this is not predicted by simulation of the pad magnetisation using OOMMF nor seen in the measured magnetisation of arrays of the pads using MOKE. As there is no movement of the peaks in the high field data, these domains would also have to persist up to 6 T and be affecting the transport in the tube due to their magnetisation or stray field parallel to the tube axis, rather than any change in their electrostatic potential due to the demagnetising field. For the misaligned domain magnetisation to produce the changes in transport observed, the domains must be orientated perpendicularly to the long axis of the pads, with a parallel and anti-parallel alignment between the two domains at positive and negative saturation. The observed shift in the peak positions could then be due to SDIPS and changes in conductance between the coercive fields of the pads attributed to a smaller rotation of the magnetisation of the domain in the soft pad. The stray field parallel to the tube axis affecting the energy levels of the quantum dot can be discounted due to the movement of multiple consecutive peaks in the same direction, as whether we consider disorder and spin-orbit coupling or not, there cannot be four consecutive energy levels in a CNT QD that show the same energy shift with applied field unless they all have the same spin.

Finally we have considered whether the change in coupling between the FM pads and the tube may be changing upon magnetic reversal, as we observe that the coupling of the pads is highly asymmetric in Device 3, with the coupling of one pad being particularly poor, causing the low conductance observed in the device. The problems with this interpretation are that the magnetostriction in Py is almost zero[36], making physical movements of the FM pad unlikely, combined with the observation of peak movement upon reversal of both pads seen in the group of 4 consecutive peaks measured meaning that the coupling of the pad that is well contacted to the CNT is also changing upon magnetic reversal. Also, while changing the coupling strength of the pads to the CNT may result in a change in the peak maximum position due to a change in the asymmetry of the peak, movements as large as those observed could only be due to changes in the capacitative coupling of the pads to the tube.

The magnetoresistance of the devices presented in this work that is independent of the changes in the induced charge on the dot has been measured by applying a source-drain bias approximately 6 times larger than the charging energy of the QD formed by Device 1, at which point the conductance of the device is assumed to be approximately constant with gate voltage, due to being out of the coulomb blockade regime. In this situation we still observe magnetoresistance which we attribute to the spin scattering at the interfaces of the device producing a GMR of $9 \pm 2\%$.

Magnetoresistance is also observed in Device 2 in magnetic loops that do not show large changes in saturation conduction, possibly indicating that the changes in conduction due to the anti-parallel alignment of the pads and the magnetisation orientation of the hard pad can be considered separately, in which case the changes in conduction could be due to spin dependant transport the magnitude of which is $\sim 10\%$. By averaging the conduction of Device 3 over the gate voltage range the four consecutive peaks are observed over we can shown the MR of the device that is independent of the movement of the peaks. This MR shows similar features to that observed in Device 2 in loops that show no saturation offset and a magnitude of $5 \pm 1\%$. These similar magnetoresistances that are seemingly independent of the movement of the coulomb blockade peaks may be due to the spin-dependant transport through the carbon nanotube.

The saturation offset in Devices 2 and 3 is due to a movement of the coulomb blockade peaks of the device that cannot be attributed to the MC effect or SDIPS and is very large ($\sim 250\%$). Due to this we must conclude that it is due to some internal quantisation axis of the CNT.

6.2 Future Work

The dependence of the magnetoresistance on the charge state of QDs formed from CNTs and changes in charge state due to FM pad magnetisation presented in this work is not yet fully understood. To gain more understanding of the processes involved experiments could be performed to confirm the domain structure of FM pads patterned onto CNTs using a technique such as magnetic force microscopy or spin-polarised electron emission microscopy. With additional experiments carried out using FM pads that have a narrower width to exclude any domain structure if domains are observed. Alternatively to investigate whether changes in conductance of devices are due to changes of the coupling of CNTs to the electrodes more devices can be measured in order to realise a CNT QD with good symmetric coupling to both electrodes, as we have shown that good coupling can be achieved using the techniques employed in this work. Additional barriers such as alumina could also be included between FM and CNT, to hold the height of the barrier between CNT and FM to a fixed value.

Possible future experiments that can be performed using sputtering as a deposition technique include measuring the angular dependence of the magnetoresistance between two ferromagnetic electrodes while applying a field of constant magnitude. This could be achieved by patterning one Py nanowire electrode combined with a circular synthetic anti-ferromagnet[116] (SAF) stack made from alternating permalloy and ruthenium layers, the magnetisation of which can be set to any angle using only a small applied field. This could then be used to find the spin precession in CNTs.

The low-temperatures needed for CNT spin transport means they are not suited for large scale spintronics applications, however their long phase coherence lengths make them a very suitable material for the study of solid-state quantum information. Recently progress has been made on realising a solid state entanglement measurement[117, 118], as proposed by Loss[119, 120], Oliver[121] and Bena[122], where the cooper pairs from a superconducting electrode split into two lengths of carbon nanotube, however it is currently unknown if the pairs remain entangled, for which the solid state equivalent of a Bell state measurement needs to be performed, for which the spin projection of split Cooper pairs needs to be measured with respect to two FM electrodes whose relative magnetic orientations need to be controllable[123]. This could be another possible development of sputtered contact to CNTs as a Py SAF structure would allow this measurement to be performed with minimal applied and stray fields to cause decoherence of the electrons in the CNTs.

References

[1] S. Iijima, “Helical microtubules of graphitic carbon,” *Nature*, vol. 354, pp. 56–58, 1991. 1

[2] D. Qian, E. C. Dickey, R. Andrews, and T. Rantell, “Load transfer and deformation mechanisms in carbon nanotube-polystyrene composites,” *Applied Physics Letters*, vol. 76, no. 20, pp. 2868–2870, 2000. 1

[3] P. M. Ajayan, L. S. Schadler, C. Giannaris, and A. Rubio, “Single-walled carbon nanotube - polymer composites: Strength and weakness,” *Advanced Materials*, vol. 12, no. 10, pp. 750–753, 2000. 1

[4] L. M. Ericson, H. Fan, H. Peng, V. A. Davis, W. Zhou, J. Sulpizio, Y. Wang, R. Booker, J. Vavro, C. Guthy, A. N. G. Parra-Vasquez, M. J. Kim, S. Ramesh, R. K. Saini, C. Kittrell, G. Lavin, H. Schmidt, W. W. Adams, W. E. Billups, M. Pasquali, W.-F. Hwang, R. H. Hauge, J. E. Fischer, and R. E. Smalley, “Macroscopic, neat, single-walled carbon nanotube fibers,” *Science*, vol. 305, no. 5689, pp. 1447–1450, 2004. 1

[5] A. B. Dalton, S. Collins, E. Munoz, J. M. Razal, V. H. Ebron, J. P. Ferraris, J. N. Coleman, B. G. Kim, and R. H. Baughman, “Super-tough carbon-nanotube fibres,” *Nature*, vol. 423, pp. 703–703, 06 2003. 1

[6] B. G. Demczyk, Y. M. Wang, J. Cumings, M. Hetman, W. Han, A. Zettl, and R. O. Ritchie, “Direct mechanical measurement of the tensile strength and elastic modulus of multiwalled carbon nanotubes,” *Materials Science and Engineering: A*, vol. 334, pp. 173–178, 9 2002. 1

[7] M. M. J. Treacy, T. W. Ebbesen, and J. M. Gibson, “Exceptionally high Young’s modulus observed for individual carbon nanotubes,” *Nature*, vol. 381, pp. 678–680, 06 1996. 1

[8] P. Kim, L. Shi, A. Majumdar, and P. L. McEuen, “Thermal transport measurements of individual multiwalled nanotubes,” *Phys. Rev. Lett.*, vol. 87, p. 215502, Oct 2001. 1

[9] S. J. Tans, A. R. M. Verschueren, and C. Dekker, “Room-temperature transistor based on a single carbon nanotube,” *Nature*, vol. 393, p. 49, 1998. 1

[10] R. Martel, T. Schmidt, H. R. Shea, T. Hertel, and P. Avouris, “Single- and multi-wall carbon nanotube field-effect transistors,” *Applied Physics Letters*, vol. 73, no. 17, 1998. 1

[11] S. Heinze, J. Tersoff, R. Martel, V. Derycke, J. Appenzeller, and P. Avouris, “Carbon nanotubes as Schottky barrier transistors,” *Phys. Rev. Lett.*, vol. 89, p. 106801, Aug 2002. 1, 2

[12] P. Avouris, Z. Chen, and V. Perebeinos, “Carbon-based electronics,” *Nature Nanotechnology*, vol. 2, p. 605, 2007. 1

[13] A. Bachtold, P. Hadley, T. Nakanishi, and C. Dekker, “Logic circuits with carbon nanotube transistors,” *Science*, vol. 294, no. 5545, pp. 1317–1320, 2001. 1

[14] C. White and T. Todorov, “Carbon nanotubes as long ballistic conductors,” *Nature*, vol. 395, p. 240, 1998. 1

[15] J. Kong, E. Yenilmez, T. Tombler, W. Kim, H. Dai, R. Laughlin, L. Liu, C. Jayanthi, and S. Wu, “Quantum interference and ballistic transmission in nanotube electron waveguides,” *Phys. Rev. Lett.*, vol. 87, no. 10, 2001. 1

[16] W. Liang, M. Bockrath, D. Bozovic, J. Hafner, M. Tinkham, and H. Park, “Fabry-Perot interference in a nanotube electron waveguide,” *Nature*, vol. 411, p. 665, 2001. 1

[17] H. I. Jørgensen, K. Grove-Rasmussen, T. Novotný, K. Flensberg, and P. E. Lindelof, “Electron transport in single-wall carbon nanotube weak links in the Fabry-Perot regime,” *Phys. Rev. Lett.*, vol. 96, p. 207003, May 2006. 1

[18] J. Cao, Q. Wang, D. Wang, and H. Dai, “Suspended carbon nanotube quantum wires with two gates,” *Small*, vol. 1, no. 1, pp. 138–141, 2005. 1

[19] M. Bockrath, D. Cobden, P. L. McEuen, N. G. Chopra, A. Zettl, A. Thess, and R. E. Smalley, “Single-electron transport in ropes of carbon nanotubes,” *Science*, vol. 275, pp. 1922–1925, 1997. 1, 12, 18, 20

[20] D. E. Logan and M. R. Galpin, “Tunneling transport and spectroscopy in carbon nanotube quantum dots,” *The Journal of Chemical Physics*, vol. 130, no. 22, p. 224503, 2009. 1

[21] S. Sapmaz, P. Jarillo-Herrero, L. P. Kouwenhoven, and H. S. J. van der Zant, “Quantum dots in carbon nanotubes,” *Semiconductor Science and Technology*, vol. 21, no. 11, p. S52, 2006. 1

[22] J. Nygard, D. H. Cobden, and P. E. Lindelof, “Kondo physics in carbon nanotubes,” *Nature*, vol. 408, p. 342, 2000. 1

[23] M. R. Buitelaar, T. Nussbaumer, and C. Schönenberger, “Quantum dot in the Kondo regime coupled to superconductors,” *Phys. Rev. Lett.*, vol. 89, p. 256801, Dec 2002. 1

[24] J. Paaske, A. Rosch, P. Wolfle, N. Mason, C. M. Marcus, and J. Nygard, “Non-equilibrium singlet-triplet Kondo effect in carbon nanotubes,” *Nature*, vol. 2, p. 460, 2006. 1

[25] J. Appenzeller, J. Knoch, V. Derycke, R. Martel, S. Wind, and P. Avouris, “Field-modulated carrier transport in carbon nanotube transistors,” *Phys. Rev. Lett.*, vol. 89, p. 126801, Aug 2002. 2

[26] Y. He, J. Zhang, Y. Wang, and Z. Yu, “Coating geometries of metals on single-walled carbon nanotubes,” *Applied Physics Letters*, vol. 96, no. 6, p. 063108, 2010. 2

[27] S. Lee, S.-J. Kahng, and Y. Kuk, “Nano-level wettings of platinum and palladium on single-walled carbon nanotubes,” *Chemical Physics Letters*, vol. 500, pp. 82 – 85, 2010. 2

[28] A. Javey, J. Guo, Q. Wang, M. Lundstrom, and H. Dai, “Ballistic carbon nanotube field effect transistors,” *Nature*, vol. 424, p. 654, 2003. 2, 46

[29] D. Mann, A. Javey, J. Kong, Q. Wang, and H. Dai, “Ballistic transport in metallic nanotubes with reliable Pd ohmic contacts,” *American Chemical Society*, vol. 3, no. 11, pp. 1541–1544, 2003. 2, 46

[30] K. Tsukagoshi, B. Alphenaar, and H. Ago, “Coherent transport of electron spin in a ferromagnetically contacted carbon nanotube,” *Nature*, vol. 401, p. 572, 1999. 2, 43

[31] S. Sahoo, T. Kontos, J. Furer, C. Hoffmann, M. Graber, A. Cottet, and C. Schönenberger, “Electrical field control of spin transport,” *Nature Physics*, vol. 1, pp. 99–102, 2005. 2, 47, 49

[32] C. Feuillet-Palma, T. Delattre, P. Morfin, J.-M. Berroir, G. Fève, D. C. Glattli, B. Plaçais, A. Cottet, and T. Kontos, “Conserved spin and orbital phase along carbon nanotubes connected with multiple ferromagnetic contacts,” *Phys. Rev. B*, vol. 81, no. 115414, 2010. 2, 46, 48

[33] F. J. Jedema, M. S. Nijboer, A. T. Filip, and B. J. van Wees, “Spin injection and spin accumulation in all-metal mesoscopic spin valves,” *Phys. Rev. B*, vol. 67, p. 085319, Feb 2003. 3

[34] Y. Ji, A. Hoffmann, J. S. Jiang, and S. D. Bader, “Spin injection, diffusion, and detection in lateral spin-valves,” *Applied Physics Letters*, vol. 85, pp. 6218–6220, DEC 20 2004. 3

[35] S. Lepadatu, J. S. Claydon, C. J. Kinane, T. R. Charlton, S. Langridge, A. Potenza, S. S. Dhesi, P. S. Keatley, R. J. Hicken, B. J. Hickey, and C. H. Marrows, “Domain-wall pinning, nonadiabatic spin-transfer torque, and spin-current polarization in permalloy wires doped with vanadium,” *Phys. Rev. B*, vol. 81, p. 020413, Jan 2010. 3

[36] L. W. McKeehan and P. P. Cioffi, “Magnetostriction in permalloy,” *Phys. Rev.*, vol. 28, pp. 146–157, Jul 1926. 3, 115, 121

[37] G. Nahrwold, J. M. Scholtyssek, S. Motl-Ziegler, O. Albrecht, U. Merkt, and G. Meier, “Structural, magnetic, and transport properties of permalloy for spintronic experiments,” *Journal of Applied Physics*, vol. 108, no. 1, p. 013907, 2010. 3

[38] A. K. Geim and K. S. Novoselov, “The rise of graphene,” *Nature Materialser*, vol. 6, pp. 183–191, 03 2007. 5

[39] R. Saito, M. Fujita, G. Dresselhaus, and M. S. Dresselhaus, “Electronic structure of graphene tubules based on C_{60},” *Phys. Rev. B*, vol. 46, pp. 1804–1811, Jul 1992. 5, 7

[40] R. Saito, M. Fujita, G. Dresselhaus, and M. S. Dresselhaus, “Electronic structure of chiral graphene tubules,” *Applied Physics Letters*, vol. 60, no. 18, 1992. 5

[41] S. Reich, C. Thomson, and J. Maultzsch, *Carbon Nanotubes*. Wiley, 2004. 5, 11

[42] R. Saito, G. Dresselhaus, and M. Dresselhaus, *Physical Properties of Carbon Nanotubes*. World Scientific, 1998. 6

[43] S. Reich, J. Maultzsch, C. Thomsen, and P. Ordejón, “Tight-binding description of graphene,” *Phys. Rev. B*, vol. 66, p. 035412, Jul 2002. 7, 12

[44] A. H. Castro Neto, F. Guinea, N. M. R. Peres, K. S. Novoselov, and A. K. Geim, “The electronic properties of graphene,” *Reviews of Modern Physics*, vol. 81, pp. 109–162, Jan-Mar 2009. 9

[45] C. Schönenberger, “Bandstructure of graphene and carbon nanotubes: An exercise in condensed matter physics.” Lecture Notes, April 2000. 9

[46] E. Hill, A. Geim, K. Novoselov, F. Schedin, and P. Blake, “Graphene spin valve devices,” *IEEE Transactions on Magnetics*, vol. 42, no. 10, pp. 2694 –2696, 2006. 9

[47] N. Tombros, C. Jozsa, M. Popinciuc, H. T. Jonkman, and B. J. van Wees, “Electronic spin transport and spin precession in single graphene layers at room temperature,” *Nature*, vol. 448, pp. 571–574, 08 2007. 9

[48] K. Ensslin, “Experiments with graphene: fabrication, characterization and electronic properties,” in *presented at Transport in Mesoscopic Systems, Capri, Italy*, 2008. 9

[49] P. L. McEuen, M. Bockrath, D. H. Cobden, Y.-G. Yoon, and S. G. Louie, “Disorder, pseudospins, and backscattering in carbon nanotubes,” *Phys. Rev. Lett.*, vol. 83, pp. 5098–5101, Dec 1999. 11, 13

[50] S. Tans, M. Devoret, H. Dai, A. Thess, R. Smalley, L. Geerligs, and C. Dekker, “Individual single-wall carbon nanotubes as quantum wires,” *Nature*, vol. 386, 1997. 12, 20

[51] S. Frank, P. Poncharal, Z. L. Wang, and W. A. de Heer, “Carbon nanotube quantum resistors,” *Science*, vol. 280, p. 1744, 1998. 12

[52] A. Kasumov, R. Deblock, M. Koclak, B. Reulet, H. Bouchiat, I. Khodos, Y. Borbatov, V. Volkov, C. Journet, and M. Burghard, “Supercurrents through single-walled carbon nanotubes,” *Science*, vol. 284, 1999. 12

[53] F. A. Zwanenburg, A. A. van Loon, G. A. Steele, C. E. W. M. van Rijmenam, T. Balder, Y. Fang, C. M. Lieber, and L. P. Kouwenhoven, “Ultrasmall silicon quantum dots,” *Journal of Applied Physics*, vol. 105, no. 12, p. 124314, 2009. 13

[54] L. P. Kouwenhoven, “Electron transport in quantum dots.” To be published in the proceedings of the Advanced Study Institute on Mesoscopic Electron Transport. 13

[55] R. Hanson, L. P. Kouwenhoven, J. R. Petta, S. Tarucha, and L. M. K. Vandersypen, “Spins in few-electron quantum dots,” *Rev. Mod. Phys.*, vol. 79, pp. 1217–1265, Oct 2007. 14, 19

[56] T. S. Jespersen, K. Grove-Rasmussen, J. Paaske, K. Muraki, T. Fujisawa, J. Nygard, and K. Flensberg, "Gate-dependent spin-orbit coupling in multielectron carbon nanotubes," *Nature Physics*, vol. 7, pp. 348–353, 04 2011. 15, 32, 33, 34, 107

[57] C. W. J. Beenakker, "Theory of coulomb-blockade oscillations in the conductance of a quantum dot," *Phys. Rev. B*, vol. 44, pp. 1646–1656, Jul 1991. 15, 16, 101

[58] M. R. Buitelaar, A. Bachtold, T. Nussbaumer, M. Iqbal, and C. Schönenberger, "Multiwall carbon nanotubes as quantum dots," *Phys. Rev. Lett.*, vol. 88, no. 15, 2002. 19, 20, 74, 100

[59] S. Ilani, L. A. K. Donev, M. Kindermann, and P. L. McEuen, "Measurement of the quantum capacitance of interacting electrons in carbon nanotubes," *Nature*, 2006. 20

[60] A. Barthélémy, A. Fert, J.-P. Contour, M. Bowen, V. Cros, J. M. De Teresa, A. Hamzic, J. C. Faini, J. M. George, J. Grollier, F. Montaigne, F. Pailloux, F. Petroff, and C. Vouille, "Magnetoresistance and spin electronics," *Journal of Magnetism and Magnetic Materials*, vol. 242–245, Part 1, pp. 68–76, 4 2002. 21

[61] S. Blundell, *Magnetism in Condensed Matter.* Oxford University Press, 2001. 21

[62] N. F. Mott, "The electrical conductivity of transition metals," *Proceedings of the Royal Society of London. Series A, Mathematical and Physical Sciences*, vol. 153, no. 880, pp. pp. 699–717, 1936. 22

[63] A. Fert and I. A. Campbell, "Electrical resistivity of ferromagnetic nickel and iron based alloys," *Journal of Physics F: Metal Physics*, vol. 6, no. 5, p. 849, 1976. 23

[64] M. Getzlaff, *Fundamentals of Magnetism.* Springer, 2008. 23, 24, 69

[65] P. C. van Son, H. van Kempen, and P. Wyder, “Boundary resistance of the ferromagnetic-nonferromagnetic metal interface,” *Phys. Rev. Lett.*, vol. 58, pp. 2271–2273, May 1987. 24, 25, 26

[66] A. Schuhl and D. Lacour, “Spin dependent transport: GMR and TMR,” *Comptes Rendus Physique*, vol. 6, no. 9, pp. 945–955, 2005. 26

[67] I. Žutić, J. Fabian, and S. Das Sarma, “Spintronics: Fundamentals and applications,” *Rev. Mod. Phys.*, vol. 76, pp. 323–410, Apr 2004. 26, 30

[68] M. N. Baibich, J. M. Broto, A. Fert, F. N. Van Dau, F. Petroff, P. Etienne, G. Creuzet, A. Friederich, and J. Chazelas, “Giant magnetoresistance of (001)Fe/(001)Cr magnetic superlattices,” *Phys. Rev. Lett.*, vol. 61, pp. 2472–2475, Nov 1988. 26, 28

[69] G. Binasch, P. Grünberg, F. Saurenbach, and W. Zinn, “Enhanced magnetoresistance in layered magnetic structures with antiferromagnetic interlayer exchange,” *Phys. Rev. B*, vol. 39, pp. 4828–4830, Mar 1989. 26

[70] I. Giaever, “Electron tunneling between two superconductors,” *Phys. Rev. Lett.*, vol. 5, pp. 464–466, Nov 1960. 28

[71] M. Julliere, “Tunneling between ferromagnetic films,” *Physics Letters A*, vol. 54, pp. 225–226, 9 1975. 28

[72] S. Maekawa and U. Gafvert, “Electron tunneling between ferromagnetic films,” *IEEE Transactions on Magnetics*, vol. 18, pp. 707 – 708, mar 1982. 29

[73] J. S. Moodera, L. R. Kinder, T. M. Wong, and R. Meservey, “Large magnetoresistance at room temperature in ferromagnetic thin film tunnel junctions,” *Phys. Rev. Lett.*, vol. 74, pp. 3273–3276, Apr 1995. 29, 30

[74] F. Kuemmeth, S. Ilani, D. C. Ralph, and P. L. McEuen, “Coupling of spin and orbital motion of electrons in carbon nanotubes,” *Nature*, vol. 452, 2008. 31, 32

[75] D. V. Bulaev, B. Trauzettel, and D. Loss, “Spin-orbit interaction and anomalous spin relaxation in carbon nanotube quantum dots,” *Phys. Rev. B*, vol. 77, p. 235301, Jun 2008. 31

[76] E. D. Minot, Y. Yaish, V. Sazonova, and P. L. McEuen, “Determination of electron orbital magnetic moments in carbon nanotubes,” *Nature*, vol. 428, pp. 536–539, 04 2004. 31

[77] A. Secchi and M. Rontani, “Coulomb versus spin-orbit interaction in few-electron carbon-nanotube quantum dots,” *Phys. Rev. B*, vol. 80, p. 041404, Jul 2009. 31

[78] S. Tans, M. Devoret, R. Groeneveld, and C. Dekker, “Electron-electron correlations in carbon nanotubes,” *Nature*, vol. 394, pp. 761–764, 1998. 31, 107, 108

[79] O. Chauvet, L. Forro, W. Bacsa, D. Ugarte, B. Doudin, and W. A. de Heer, “Magnetic anisotropies of aligned carbon nanotubes,” *Phys. Rev. B*, vol. 52, pp. R6963–R6966, Sep 1995. 31, 107

[80] S. Moriyama, T. Fuse, T. Yamaguchi, and K. Ishibashi, “Spin effects in single-electron transport through carbon nanotube quantum dots,” *Phys. Rev. B*, vol. 76, p. 045102, Jul 2007. 31, 34

[81] C. H. L. Quay, J. Cumings, S. J. Gamble, R. Picciotto, H. Kataura, and D. Goldhaber-Gordon, “Magnetic field dependence of the spin-$\frac{1}{2}$ and spin-1 kondo effects in a quantum dot,” *Phys. Rev. B*, vol. 76, p. 245311, Dec 2007. 31, 107

[82] P. Jarillo-Herrero, S. Sapmaz, C. Dekker, L. P. Kouwenhoven, and H. S. J. van der Zant, “Electron-hole symmetry in a semiconducting carbon nanotube quantum dot,” *Nature*, vol. 429, pp. 389–392, 05 2004. 31, 107

[83] H. Ingerslev Jorgensen, K. Grove-Rasmussen, K. Y. Wang, A. M. Blackburn, K. Flensberg, P. E. Lindelof, and D. A. Williams, “Singlet-triplet physics and shell filling in carbon nanotube double quantum dots,” *Nature Physics*, vol. 4, pp. 536–539, 07 2008. 34

[84] A. Makarovski, L. An, J. Liu, and G. Finkelstein, "Persistent orbital degeneracy in carbon nanotubes," *Phys. Rev. B*, vol. 74, p. 155431, Oct 2006. 34, 35, 108

[85] D. H. Cobden and J. Nygård, "Shell filling in closed single-wall carbon nanotube quantum dots," *Phys. Rev. Lett.*, vol. 89, p. 046803, Jul 2002. 36

[86] S. J. van der Molen, N. Tombros, and B. J. van Wees, "Magneto-coulomb effect in spin-valve devices," *Phys. Rev. B*, vol. 73, 2006. 37, 38, 78, 101

[87] A. Bernand-Mantel, P. Seneor, K. Bouzehouane, S. Fusil, C. Deranlot, F. Petroff, and A. Fert, "Anisotropic magneto-coulomb effects and magnetic single-electron-transistor action in a single nanoparticle," *Nature Physics*, vol. 5, 2009. 37, 101

[88] M. B. A. Jalil, S. G. Tan, and M. J. Ma, "Enhanced magneto-coulomb effect in asymmetric ferromagnetic single electron transistors," *Journal of Applied Physics*, vol. 105, no. 7, p. 07C905, 2009. 37, 101, 115

[89] K. Ono, H. Shimada, and Y. Ootuka, "Enhanced magnetic valve effect and magneto-coulomb oscillations in ferromagnetic single electron transistor," *Journal of the Physical Society of Japan*, vol. 66, no. 5, pp. 1261–1264, 1997. 37

[90] S. Datta, L. Marty, J. P. Cleuziou, C. Tilmaciu, B. Soula, E. Flahaut, and W. Wernsdorfer, "Magneto-coulomb effect in carbon nanotube quantum dots filled with magnetic nanoparticles," *Phys. Rev. Lett.*, vol. 107, p. 186804, Oct 2011. 37, 39

[91] A. Cottet and M.-S. Choi, "Magnetoresistance of a quantum dot with spin-active interfaces," *Phys. Rev. B*, vol. 74, p. 235316, Dec 2006. 40, 41, 42, 43, 48, 49, 108, 109

[92] A. Cottet, T. Kontos, S. Sahoo, H. T. Man, M.-S. Choi, W. Belzig, C. Bruder, A. F. Morpurgo, and C. Schönenberger, "Nanospintronics with carbon nanotubes," *Semiconductor Science and Technology*, vol. 21, pp. S78–S95, 2006. 40, 42, 48, 119

[93] K. Tsukagoshi and B. Alphenaar, “Spin-polarized transport in carbon nanotubes,” *Superlattices and Microstructures*, vol. 27, p. 565, 2000. 43

[94] J.-R. Kim, H. M. So, J.-J. Kim, and J. Kim, “Spin-dependent transport properties in a single-walled carbon nanotube with mesoscopic co contacts,” *Phys. Rev. B*, vol. 66, p. 233401, Dec 2002. 44

[95] N. Tombros, S. J. van der Molen, and B. J. van Wees, “Separating spin and charge transport in single-wall carbon nanotubes,” *Phys. Rev. B*, vol. 73, no. 233403, 2006. 44, 45, 91, 98, 99, 118

[96] A. Jenson, J. R. H. abd J. Nygard, and P. E. Lindelof, “Magnetoresistance in ferromagnetically contacted single-wall carbon nanotubes,” *Phys. Rev. B*, vol. 72, p. 035419, 2005. 45, 46, 82

[97] B. Nagabhirava, T. Bansal, G. U. Sumanasekera, and B. W. Alphenaar, “Gated spin transport through an individual single wall carbon nanotube,” *Applied Physics Letters*, vol. 88, p. 023503, 2006. 46, 47

[98] S. Sahoo, T. Kontos, J. Furer, C. Hoffmann, M. Graber, A. Cottet, and C. Schönenberger, “Electric field control of spin transport,” *Nature Physics*, vol. 1, pp. 99–102, 11 2005. 46, 91, 108, 109

[99] H. T. Man, I. J. W. Wever, and A. F. Morpurgo, “Spin-dependent quantum interference in single-wall carbon nanotubes with ferromagnetic contacts,” *Phys. Rev. B*, vol. 73, p. 241401, 2006. 46

[100] H. Aurich, A. Baumgartner, F. Freitag, A. Eichler, J. Trbovic, and C. Schönenberger, “Permalloy-based carbon nanotube spin-valve,” *Applied Physics Letters*, vol. 97, no. 15, p. 153116, 2010. 49, 50, 119

[101] C. Morgan, C. M. Schneider, and C. Meyer, “Permalloy and $Co_{50}Pd_{50}$ as ferromagnetic contacts for magnetoresistance measurements in carbon nanotube-based transport structures,” *Journal of Applied Physics*, vol. 111, no. 7, p. 07B309, 2012. 50, 119

[102] J. Furer, *Growth of Single-Wall Carbon Nanotubes by Chemical Vapor Deposition for Electrical Devices*. PhD thesis, Basel University, 2006. 51

[103] T. Brintlinger, Y.-F. Chen, T. Durkop, E. Cobas, M. S. Fuhrer, J. D. Barry, and J. Melngailis, "Rapid imaging of nanotubes on insulating substrates," *Applied Physics Letters*, vol. 81, no. 13, pp. 2454–2456, 2002. 55

[104] P. N. Argyres, "Theory of the faraday and kerr effects in ferromagnetics," *Phys. Rev.*, vol. 97, pp. 334–345, Jan 1955. 59

[105] Z. Q. Qiu and S. D. Bader, "Surface magneto-optic kerr effect," *Review of Scientific Instruments*, vol. 71, no. 3, pp. 1243–1255, 2000. 59

[106] V. K. Pecharsky and K. A. G. Jr, "Magnetocaloric effect and magnetic refrigeration," *Journal of Magnetism and Magnetic Materials*, vol. 200, pp. 44 – 56, 1999. 61

[107] "The Object Oriented MicroMagnetic Framework (OOMMF) project at ITL/NIST." *ITL/NIST* (online), 2011. `http://math.nist.gov/oommf/`. 65

[108] L. D. Landau and E. M. Lifshitz, "On the theory of the dispersion of magnetic permeability in ferromagnetic bodies," *Phys. Z. Sowjetunion*, vol. 8, no. 153, 1935. 65

[109] T. L. Gilbert, "Lagrangian Formulation Of The Gyromagnetic Equation Of The Magnetization Field," *Physical Review*, vol. 100, no. 4, p. 1243, 1955. 65

[110] M. C. Hickey, D.-T. Ngo, S. Lepadatu, D. Atkinson, D. McGrouther, S. McVitie, and C. H. Marrows, "Spin-transfer torque efficiency measured using a permalloy nanobridge," *Applied Physics Letters*, vol. 97, no. 20, p. 202505, 2010. 67

[111] K. J. Kirk, J. N. Chapman, and C. D. W. Wilkinson, "Switching fields and magnetostatic interactions of thin film magnetic nanoelements," *Applied Physics Letters*, vol. 71, no. 4, pp. 539–541, 1997. 85

[112] T. Schrefl, J. Fidler, K. Kirk, and J. Chapman, “Domain structures and switching mechanisms in patterned magnetic elements,” *Journal of Magnetism and Magnetic Materials*, vol. 175, pp. 193–204, 1997. 85

[113] D. Preusche, S. Schmidmeier, E. Pallecchi, C. Dietrich, A. K. Hüttel, J. Zweck, and C. Strunk, “Characterization of ferromagnetic contacts to carbon nanotubes,” *Journal of Applied Physics*, vol. 106, no. 084314, 2009. 85

[114] T. W. Odom, J.-L. Huang, and C. M. Lieber, “STM studies of single-walled carbon nanotubes,” *Journal of Physics: Condensed Matter*, vol. 14, pp. R145–R167, 2002. 115

[115] L. W. Liu, J. H. Fang, L. Lu, H. F. Yang, A. Z. Jin, and C. Z. Gu, “Spin-dependent transport through a single-walled carbon nanotube coupled to a ferromagnetic and a nonmagnetic metal electrode,” *Phys. Rev. B*, vol. 74, p. 245429, Dec 2006. 116, 117

[116] J. L. Leal and M. H. Kryder, “Spin valves exchange biased by Co/Ru/Co synthetic antiferromagnets,” *Journal of Applied Physics*, vol. 83, no. 7, pp. 3720–3723, 1998. 122

[117] L. G. Herrmann, F. Portier, P. Roche, A. L. Yeyati, T. Kontos, and C. Strunk, “Carbon nanotubes as cooper-pair beam splitters,” *Phys. Rev. Lett.*, vol. 104, p. 026801, Jan 2010. 122

[118] L. Hofstetter, S. Csonka, J. Nygard, and C. Schönenberger, “Cooper pair splitter realized in a two-quantum-dot y-junction,” *Nature*, vol. 461, pp. 960–963, 10 2009. 122

[119] D. Loss and D. P. DiVincenzo, “Quantum computation with quantum dots,” *Phys. Rev. A*, vol. 57, no. 1, 1998. 122

[120] P. Recher and D. Loss, “Superconductor coupled to two luttinger liquids as an entangler for electron spins,” *Phys. Rev. B*, vol. 65, no. 165327, 2002. 122

[121] W. D. Oliver, F. Yamaguchi, and Y. Yamamoto, "Electron entanglement via a quantum dot," *Phys. Rev. Lett.*, vol. 88, no. 3, 2002. 122

[122] C. Bena, S. Vishveshwara, L. Balents, and M. Fisher, "Quantum entanglement in carbon nanotubes," *Phys. Rev. Lett.*, vol. 89, no. 3, 2002. 122

[123] S. Kawabata, "Test of bell's inequality using the spin filter effect in ferromagnetic semiconductor microstructures," *Journal of the Physical Society of Japan*, vol. 70, no. 5, pp. 1210–1213, 2001. 123